Title

Vanadium Oxide Electrochemical Capacitors: An Investigation into Aqueous Capacitive Degradation, Alternate Electrolyte-Solvent Systems, Whole Cell Performance and Graphene Oxide Composite Electrodes

Author

Engstrom, Allison Michelle

Publication Date

2013

Peer reviewed|Thesis/dissertation

Vanadium Oxide Electrochemical Capacitors: An Investigation into Aqueous Capacitive Degradation, Alternate Electrolyte-Solvent Systems, Whole Cell Performance and Graphene Oxide Composite Electrodes

By

Allison Michelle Engstrom

A dissertation submitted in partial satisfaction of the

requirements for the degree of

Doctor of Philosophy

in

Engineering – Materials Science and Engineering

in the

Graduate Division

of the

University of California, Berkeley

Committee in charge:

Professor Fiona M. Doyle, Chair
Professor James W. Evans
Professor Elton J. Cairns

Fall 2013

Abstract

Vanadium Oxide Electrochemical Capacitors:
An Investigation into Aqueous Capacitive Degradation, Alternate Electrolyte-Solvent Systems, Whole Cell Performance and Graphene Oxide Composite Electrodes

By

Allison Michelle Engstrom

Doctor of Philosophy in Engineering – Materials Science and Engineering

University of California, Berkeley

Professor Fiona M. Doyle, Chair

Vanadium oxide has emerged as a potential electrochemical capacitor material due to its attractive pseudocapacitive performance; however, it is known to suffer from capacitive degradation upon sustained cycling. In this work, the electrochemical cycling behavior of anodically electrodeposited vanadium oxide films with various surface treatments in aqueous solutions is investigated at different pH. Quantitative compositional analysis and morphological studies provide additional insight into the mechanism responsible for capacitive degradation. Furthermore, the capacitance and impedance behavior of vanadium oxide electrochemical capacitor electrodes is compared for both aqueous and nonaqueous electrolyte-solvent systems. Alkali metal chloride and bromide electrolytes were studied in aqueous systems, and nonaqueous systems containing alkali metal bromides were studied in polar aprotic propylene carbonate (PC) or dimethyl sulfoxide (DMSO) solvents. The preferred aqueous and nonaqueous systems identified in the half-cell studies were utilized in symmetric vanadium oxide whole-cells. An aqueous system utilizing a 3.0 M NaCl electrolyte at pH 3.0 exhibited an excellent 96% capacitance retention over 3000 cycles at 10 mV s^{-1}. An equivalent system tested at 500 mV s^{-1} displayed an increase in capacitance over the first several thousands of cycles, and eventually stabilized over 50,000 cycles. Electrodes cycled in nonaqueous 1.0 M LiBr in PC exhibited mostly non-capacitive charge-storage, and electrodes cycled in LiBr-DMSO exhibited a gradual capacitive decay over 10,000 cycles at 500 mV s^{-1}. Morphological and compositional analyses, as well as electrochemical impedance modeling, provide additional insight into the cause of the cycing behavior. Lastly, reduced graphene oxide and vanadium oxide nanowire composites have been successfully synthesized using electrophoretic deposition for electrochemical capacitor electrodes. The composite material was found to perform with a higher capacitance than electrodes containing only vanadium oxide nanowires by a factor of 4.0 at 10 mV s^{-1} and 7.5 at 500 mV s^{-1}. The thermally reduced composite material was examined in both symmetric and asymmetric whole cell electrochemical capacitor devices, and although the asymmetric cell achieved both higher energy and power density, the symmetric cell retained a higher capacitance over 50,000 cycles at 200 mV s^{-1}.

Dedication

To Mom, Dad, Erika, Melanie and Chris for their endless support.

Table of Contents

List of Figures

List of Tables

List of Symbols and Abbreviations

A, CPE_a	Surface area [m^2] or Coefficient corresponding to constant phase element, CPE_A, associated with double layer charging mechanism [$S \cdot s^a$]
a	Exponent corresponding to constant phase element, CPE_A, where $a = 1$ represents ideal capacitive behavior
B, CPE_b	Coefficient corresponding to constant phase element, CPE_B, associated with the direct passage of current across the electrode/electrolyte interface according to the pseudocapacitive mechanism [$S \cdot s^b$]
b	Exponent corresponding to constant phase element, CPE_B, where $b = 1$ represents ideal capacitive behavior
C	Capacitance [F]
C_b	Capacitance associated with the direct passage of current across the electrode/electrolyte interface according to the pseudocapacitive mechanism [F]
C_s	Specific Capacitance [F g^{-1} or F cm^{-1}]
GCD	Galvanostatic charge/discharge
CV	Cyclic voltammetry
CPE	Constant phase element
crGO	Chemically reduced graphene oxide
cr(GO/V_xO_y)	Chemically reduced graphene oxide and vanadium oxide composite
D	Defect-induced Raman scattering band in graphene sheets
D’	Defect-induced Raman scattering band in graphene sheets
d	Distance between plates in parallel plate capacitor [m]
DMSO	Dimethyl sulfoxide
E_s	Specific energy density [Wh kg^{-1}]
EC	Electrochemical capacitor
EDLC	Electrochemical double layer capacitor
EDS	Energy dispersive spectrometry
EIS	Electrochemical impedance spectroscopy
ESR	Equivalent series resistance [Ω]
G	Raman scattering band associated with the optical vibrational mode of two neighboring carbon atoms on a graphene layer
G’	Second order Raman scattering band or overtone of the defect-induced D band, sensitive to defects along the c-axis in the stacking order of graphene sheets
GO	Graphene oxide
GO/V_xO_y	As-deposited graphene oxide and vanadium oxide composite
i	Current [A]

I_D/I_G	Ratio of the integrated area of the D and G Raman peaks
j	$\sqrt{-1}$
LF Ag/AgCl	Leak-free silver/silver chloride reference electrode
m	Mass of the electrode [g]
P_s	Specific maximum power density [kW kg^{-1}]
PC	Propylene carbonate
Q ,q	Charge [C]
R_a	Charge-transfer resistance [Ω]
R_b	Resistance associated with the direct passage of current across the electrode/electrolyte interface according to pseudocapacitive mechanism [Ω]
R_s	Equivalent series resistance [Ω]
SEM	Scanning electron microscopy
SHE	Standard hydrogen electrode
t_{disch}	Time of discharge half-cycle [s]
trGO	Thermally reduced graphene oxide
tr(GO/V_xO_y)	Thermally reduced graphene oxide and vanadium oxide composite
V	Potential or potential window [V]
V_{window}	Potential window [V]
V_xO_y	Mixed-valence vanadium oxide
W	Coefficient corresponding to the Warburg diffusional impedance [$S \cdot s^{0.5}$]
WDS	Wavelength dispersive spectrometry
Z	Total Impedance [Ω]
Z'	Real component of the total impendence [Ω]
Z''	Imaginary component of the total impedance [Ω]
ε	Dielectric constant [F m^{-1}]
ε_0	Permittivity of free space = 8.85 × 10-12 F m^{-1}
v	Scan rate [V s^{-1}]
ω	Frequency [Hz or s^{-1}]

Acknowledgements

I would like to first acknowledge the funding sources that supported the research herein. This material is based upon work supported by the National Science Foundation Graduate Research Fellowship under Grant No. DGE-1106400 and under Grant # EEC-1059472 to the American Society for Engineering Education.

I would next like to thank the people who made such a significant impact on my graduate experience throughout my time at UC Berkeley.

First and foremost, I want to acknowledge my advisor, Prof. Fiona Doyle, whose support and mentorship I greatly value and cherish. Since the inception of my dissertation research, she has encouraged me to develop and pursue my research interests, which not only facilitated my research progress but also helped me to grow professionally, to think more critically and to gain confidence in my knowledge and capabilities. Thank you, Prof. Doyle, for the many motivating and uplifting conversations, which never failed to renew my passion for research.

I would also like to thank Prof. Elton Cairns and Prof. James Evans for their advisement. I am extremely grateful for their willingness to make time to discuss my research and for their suggestions for improvement.

I also want to extend my gratitude to the collaborators and colleagues at UC Berkeley, who helped me to achieve my research goals, including Tim Teague for assistance with the SEM and EDS as well as Sean Mulcahy for performing WDS.

Over the last few years I have had the amazing opportunity to work with several co-workers and collaborators. I must acknowledge my lab mates, who worked beside me through the ups and downs that accompany experimental research. Thank you for your support and friendship: Daniel Riffe, Anahit Raygani, Gretchen Lapidus-Lavine, Hongxu "Shu" Liu, Brandon Wood, Alyssa Maich, Yegan Erdem, Akshita Dutta, Gagandeep Sidhu and Andrew Dussault.

Toward the end of my research, I had the great fortune to collaborate with Dr. Bin Chen of LC Tech at NASA Ames Research Center. Her passion for engineering and innovation was a daily source of inspiration, and I greatly admired her ability to create a challenging and competitive atmosphere for her team while still managing to make the collaboration such an exciting and enjoyable experience.

Additionally, I would like to thank my colleagues at NASA Ames Research Center: Daniel Gutierrez for assistance with Raman and four-point probe measurements, Mohamad Raad and Vivek Jayan for aiding with SEM and Robin Young for vanadium oxide nanowire synthesis.

I am so grateful to my wonderful family for their endless support and love. I must thank my sister, Erika, a.k.a. "DrE". I am so grateful for her advice, guidance and encouragement

throughout every stage of my life. I will always treasure our time together at ASU; I was so fortunate to have the opportunity to work with such an amazing person, let alone my sister. Erika, thank you for lending an ear and helping me through the most challenging moments of graduate school. I could never thank you enough. Thanks to Melanie, my twin sister, who can usually tell how I'm feeling before I do. Thank you for the many car rides full of laughs and biology lessons, both of which I deeply appreciate more than you know. Thank you, Mom and Dad, for always finding a way to bring a little bit of home to me every Sunday over Skype. It was my lifeline to all of you whom I love and missed every day while away at school.

Next, I must convey my endless appreciation to Chris, my fiancé and love of my life. He has been alongside me throughout these last five years, and I will be forever grateful for his strength, patience, understanding and sense of humor through it all. Thank you, and I love you.

Chapter 1 – Introduction

1.1 Historical Overview

The discovery of charge separation with the invention of the Leyden jar in 1745 is attributed to Dean Kleist at Leyden and almost simultaneously to Musschenbroek at Kamin, Pomerania. The condenser, or later referred to as a capacitor, was composed of a glass jar containing an immersed electrode suspended in an aqueous electrolyte, and wrapped around the outside of the jar was a metal foil. It was discovered that an amount of charge could be stored when a potential difference was applied between the electrode and the foil, with the glass acting as the dielectric [1]. However, it wasn't until nearly 140 years later that the mechanisms of electrical charge storage in capacitors could start to be fully understood.

Twenty four years after the Leyden jar, "voltaic electricity" was discovered by Alessandro Volta of Como, Italy, which marked the invention of the battery [1,2]. However, it wasn't until 1881 when von Helmholtz reached the conclusion that Faraday's laws implied a fundamental unit of electrical charge that a comprehensive understanding of charge-storage phenomena could begin. In the same year Johnstone Stoney coined the term "electron" from the Greek word ελεκτον for amber referring to the fundamental unit of electricity. This breakthrough paved the way for a more quantitative, fundamental approach to better understand electrochemistry [1].

In 1947 the double layer model by Grahame furthered the electrochemical community's understanding of the electrode/solution interface [1]. Utilizing the concept of double layer capacitance H. E. Becker proposed the first practical application of double layer capacitance in his 1957 patent describing porous carbon materials in contact with an aqueous electrolyte [3]. Further commercial applications of electrochemical capacitors followed such as the Supercapacitor coined by Nippon Electric Company under license from SOHIO in 1978 and the Ultracapacitor coined by Pinnacle Research for military applications based on the research by Conway in the 1970s and 1980s [1,4]. The study of transition metal oxides for utilization in electrochemical capacitors began with the discovery of the capacitive properties of hydrated ruthenium oxide [5], but in 1999, Lee and Goodenough were the first to describe vanadium oxide as a more cost-effective material for electrochemical capacitors [6].

1.2 Introduction

1.2.1 Global Energy Storage

The recent projection that global energy consumption will double over the next five decades has increased awareness and stimulated funding for energy storage research, development and implementation on a global scale [7]. The push for higher contributions from renewable energy

sources such as solar and wind require efficient electrical energy storage systems to effectively level their innate cyclic nature.

In 2009 the U.S. Department of Energy (DOE) launched a significant energy storage program as part of the funding from the American Recovery and Reinvestment Act (ARRA), which provided a total investment of $772 million that produced 537 MW of new storage systems to be added to the grid. In 2010-2011 DOE's Advanced Research Projects Agency-Energy (ARPA-E) invested over $55 million in grid-scale, rampable intermittent dispatchable storage projects, and in 2012 the budget contained $550 million for continued ARPA-E activities including $40 million for the Energy Storage Technology Program [8].

According to a report from Pike Research in 2011, the global energy storage capacity is projected to multiply 100-fold from 121 GW to 12535 GW by 2021 [9]. Although the industry is dominated by pumped hydro technology, responsible for 95% in the U.S. and 98% of the global energy storage capacity, the fastest growing systems are "fast storage" technologies for applications such as frequency response regulation [8]. Even second-to-second fluctuations in the power supply cause major disruptions that lead to tens of billions of dollars in estimated annual costs [7]. Batteries and electrochemical capacitors lead this critical area of technological development.

1.2.2 Charge Storage in Electrochemical Capacitors

Electrochemical capacitors (ECs) are an important class of energy storage because they provide higher energy densities than traditional electrostatic capacitors and higher power densities than battery systems [1,10]. They are further distinguished by the two primary charge storage mechanisms that dominate these devices. The first, the electrochemical double layer capacitor (EDLC), is closely related to traditional capacitors because the charge is stored electrostatically across the double layer that forms at the electrode/electrolyte interface and ideally no Faradaic charge transfer occurs across the interface unlike the second type of device, the pseudocapacitor. Its energy storage mechanism is dominated by highly reversible redox reactions at the surface and in the bulk of the material, i.e. the transition between the various oxidation states in transition metal oxides accompanied by the intercalation and deintercalation of electrolyte ions. ECs are regarded for their high specific capacitance, high specific power and energy density, low material cost and toxicity as well as a long cycle life owing to high reversibility [1,10-13].

To understand the capacitive mechanism behind the EDLC, it is first necessary to review the capacitance behavior of a classical electrostatic parallel-plate capacitor. The capacitance of a parallel-plate capacitor (see Figure 1.1) is defined as the amount of charge, q, stored on two opposing electrodes per volt of the applied potential difference, V, separated by a dielectric. According to electrostatics, the capacitance (see Eq. 1.1) is inversely proportional to the distance between the plates and directly proportional to the dielectric constant [1].

An EDLC device achieves relatively larger specific capacitance than traditional electrostatic capacitors because the separation distance of opposing charges is on the order of 0.5 - 0.6 nm in the compact region of the double layer as illustrated in Figure 1.2 as opposed to the few tens of microns that typically limits traditional capacitors [1,14]. Additionally, EDLCs are typically

constructed with high surface area carbon materials on the order of 2000 $m^2\ g^{-1}$, which effectually increases the area, *A*, in Eq. 1.1.

$$C = \frac{q}{V} = \frac{A\varepsilon\varepsilon_0}{d} \tag{1.1}$$

Due to the electrostatic nature of the double layer charging mechanism, these devices exhibit almost ideal reversibility, which leads to an almost limitless cycle life. All electrochemical systems including pseudocapacitors exhibit double layer charging, which is estimated to account for about 5-10% of the total measured capacitance [1].

Pseudocapacitive ECs exhibit battery-type behavior due to Faradaic processes but also exhibit capacitor-type electrical characteristics where a functional relationship between the extent of charge, *q*, accommodated and the change in potential, *V*, of the electrode results in a derivative *dq/dV* corresponding to a capacitance. This property is termed a "pseudo" capacitance since it originates in a fundamentally different way to classical electrostatic capacitance as in traditional capacitors or EDLCs [1]. Transition metal oxides have been recognized for their pseudocapacitance properties ever since the paper by Trasatti and Buzzanca that reported the capacitive properties of ruthenium oxide [5]. The capacitance of hydrated $RuO_2 \cdot nH_2O$ has reached as high as 900 $F\ g^{-1}$ [15]. However, this material is prohibitively expensive for commercial applications and thus other transition metal oxides have been explored [11,12,16]. Vanadium oxide is a desirable active material due to its wide range of stable oxidation states (V, IV, III and II) and its relatively low cost and toxicity compared to RuO_2 [6,17].

In addition to double layer charging exhibited by all electrochemical systems, the pseudocapacitive charge storage mechanism in transition metal oxides involves the reduction and oxidation between oxidation states creating a local buildup of charge in the material that is compensated by adsorption or intercalation of ions from the electrolyte [11]. For the hydrated vanadium oxide system, two possible mechanisms may occur involving either a proton-electronic mechanism or an ionic adsorption/desorption mechanism whose equilibrium is demonstrated in Equations 1.2 and 1.3, respectively [18]. The position of equilibrium is clearly

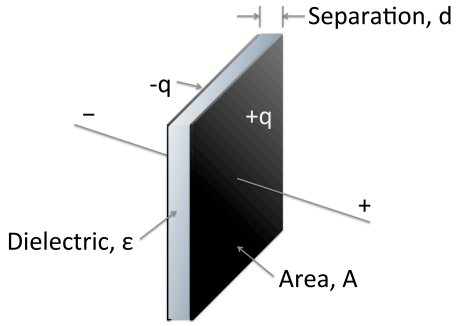

Figure 1.1: Charged capacitor with charge ± q on each plate of surface area, *A*, with separation distance, *d*, between the plates and a dielectric medium separating the plates with dielectric constant *ε*.

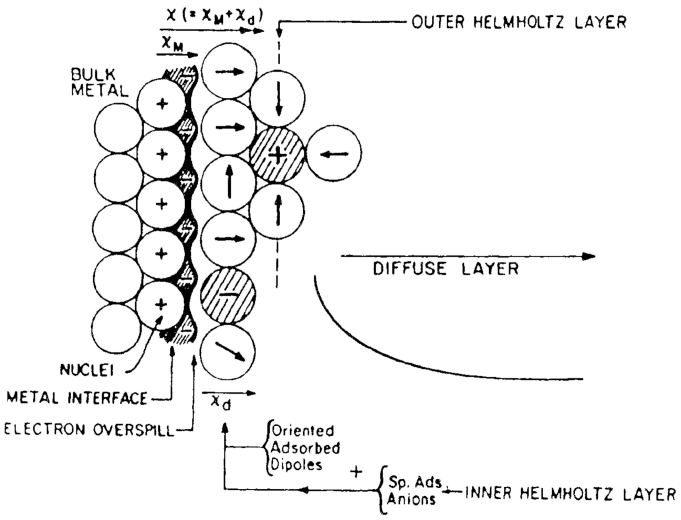

Figure 1.2: Double layer that arises at the electrode/solution interface.

dependent upon the electrochemical potential; thus, the potential can be manipulated to control the direction of current flow.

$$VO_a(OH)_b + \delta H^+ + \delta e^- \rightleftharpoons VO_{a-\delta}(OH)_{b+\delta} \tag{1.2}$$

$$VO_a(OH)_b + \delta Na^+ + \delta e^- \rightleftharpoons Na_\delta VO_a(OH)_b \tag{1.3}$$

This material exhibits excellent specific capacitance ranging from 90 to 870 F g^{-1} depending upon the structure, composition and morphology as determined by the synthesis and processing methods as well as the testing environment [6,17-23]. However, it also exhibits significant degradation upon cycling [17,19,24,25]. A more comprehensive study of the interfacial phenomena leading to pseudocapacitance and degradation in vanadium oxides is necessary to effectively exploit this material in electrochemical capacitor energy storage devices.

1.3 Technical Approach

Pseudocapacitors exhibit characteristics of both double layer charging as in EDLCs and Faradaic charge-transfer associated with battery systems. Thus, they may be able to address the critical performance gaps that exist between these two most common classes of electrical energy storage devices [7]. However, the pseudocapacitive EC has not been as commercially viable as the double layer type of EC in the energy storage industry [4]. In 2007 the Office of Basic Energy Sciences within the DOE Office of Science convened a workshop to identify the basic research needs and opportunities of current electrical energy storage technologies. With regards to pseudocapacitive materials, it was concluded that research directives in future fundamental research should not only include the discovery of new materials and architectures but should also aspire toward a fundamental understanding of interfacial phenomena including the charge-

storage process [7]. Thus, an investigation was performed of the structure, composition and electrical properties using a variety of characterization techniques to understand the phenomena associated with pseudocapacitance, possible degradation upon cycling and overall performance characteristics of vanadium oxide and graphene oxide/vanadium oxide composites in electrochemical capacitors.

1.4 Chapter Layout

Chapter 2 reports the investigation into the capacitive degradation mechanism of electrodeposited vanadium oxide in aqueous electrolytes in various pH environments upon galvanostatic charge/discharge and voltammetric cycling.

Chapter 3 provides the results from the study of aqueous and nonaqueous electrolyte-solvent systems tested for electrodeposited vanadium oxide. Electrochemical and morphological analyses are utilized to determine the preferred systems for utilization in the whole-cell analysis presented in Chapter 4. In this chapter, the separator design is investigated and both aqueous and nonaqueous systems at relatively fast and slow cycle rates are investigated regarding their resulting power and energy density as well as cycle behavior.

Chapter 5 outlines the study into electrophoretically deposited graphene oxide and vanadium oxide composite electrodes. Both chemical and thermal reduction methods are investigated. Furthermore, the whole-cell energy density, power density and cycling behavior are measured for symmetric and asymmetric electrochemical capacitor cells containing the composite electrodes.

Chapter 6 contains a summary of the most significant conclusions from the work outlined in the preceding chapters. It also includes suggestions for future research and development of vanadium oxide electrochemical capacitor electrodes.

Chapter 2 – Exploring the Cycling Behavior of Electrodeposited Vanadium Oxide in Various Aqueous Environments

This material has been previously published:

A. M. Engstrom, F. M. Doyle, J. Power Sources 228 (2013) 120-131.

Abstract

Electrodeposited vanadium oxide has emerged as a potential electrochemical capacitor material due to its attractive initial pseudocapacitive performance. However, it suffers from capacitive degradation upon charge/discharge cycling in aqueous electrolytes. Possible degradation mechanisms, including material dissolution, are discussed. To test these possible mechanisms, an agar gel coating is deposited on the films to reduce mass transport between the electrode-electrolyte interface. The electrochemical cycling behavior of vanadium oxide films with various surface treatments is investigated at different pH. Quantitative compositional analysis and morphological studies provide additional insight into the mechanism responsible for capacitive degradation.

2.1 Introduction

In 2011 the world's population exceeded 7 billion. Energy demand is at an all time high, and it will only go up. An essential part of this energy demand is its capture, storage and release, and although traditional batteries and capacitors have dominated this area, electrochemical capacitors have emerged as a complementary technology with unique energy storage characteristics.

Generally referred to as electrochemical capacitors, these devices include supercapacitors and ultracapacitors, which were coined by Nippon Electric Company and Pinnacle Research Institute, respectively. These electrical energy storage devices bridge the gap between high power density capacitors and high energy density batteries [1]. These devices are utilized in high pulsed-power and time-dependent usage applications, such as power sources in hybrid electric vehicles and as backup sources for memories and microcomputers [12]. Much broader

deployment is clearly possible when one considers the potential for capturing and redirecting large bursts of waste energy over short timespans to improve energy efficiency.

The two types of electrochemical capacitors are characterized by their primary charge storage mechanisms: those that store energy in the electrochemical double layer and those that also exhibit pseudocapacitance. Electrical double layer capacitors store energy by charge separation across the double layer that exists between the electrode surface and the electrolyte. High surface area materials, such as activated carbon, are commonly used for this technology. In addition to double layer charging, materials that exhibit pseudocapacitance store charge via reversible Faradaic reduction or oxidation (redox) reactions. For transition metal oxides, the redox reactions may simply be reduction and oxidation between the transition metal oxidation states. As the redox reactions take place in the material, local charge-buildup is compensated by intercalation of ions from the electrolyte [11]. Figure 2.1 illustrates this mechanism for a whole cell electrochemical capacitor device. Upon charging, the cathode undergoes reduction, which induces the cations from the electrolyte to intercalate into the structure. Meanwhile, oxidation occurs at the anode, where the cations deintercalate.

For the vanadium oxide system, Eq. 2.1 shows the equilibrium between V(V) oxide, monovalent cations from the electrolyte, M^+, and the oxide in which the V(V) has been reduced to V(IV) (without disruption of the oxide lattice), with the resulting charge compensated by intercalation of the monovalent cations. The position of equilibrium is clearly dependent upon the electrochemical potential; thus, the potential can be manipulated to control the direction of current flow.

$$(V_2O_5)_{surface} + 2M^+ + 2e^- \leftrightarrow (V_2O_5^{2-}M_2^{2+})_{surface} \tag{2.1}$$

The metal oxides most widely studied for electrochemical capacitor applications are RuO_2 and MnO_2. Unfortunately, RuO_2 is expensive and toxic, while MnO_2 can only be used at high-pH in

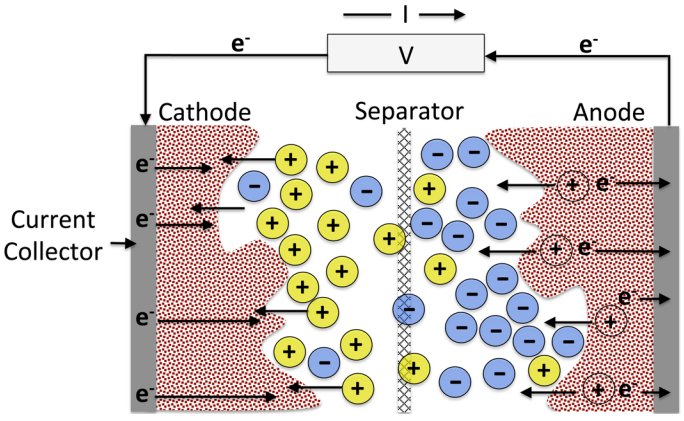

Figure 2.1: Charging of an electrochemical capacitor device containing transition metal oxide anode and cathode materials. The metal oxidation state is reduced at the cathode, which induces cations to intercalate from the electrolyte. In contrast, oxidation at the anode causes deintercalation.

aqueous environments. Vanadium oxide is only five percent of the cost of RuO_2, and it has been shown to discharge 1.6 times faster, other things being equal [6]. Although nanostructured vanadium oxides may be synthesized by a variety of methods, electrochemical deposition provides a means of controlling the surface morphology and crystallinity by varying the electrochemical parameters [20,21,24,26-34].

Despite the attractive initial capacitance, vanadium oxide films typically exhibit performance degradation during cycling, particularly in aqueous environments, which are intrinsically attractive because of their high conductivity; material dissolution may be the primary cause [35]. In the current work, vanadium oxide films were synthesized by anodic electrodeposition, and an agar gel coating was tested as a means of reducing mass transport of dissolved vanadium species from the surface of the electrode in aqueous media. These structures were used to investigate not only the V_2O_5, but also the V_2O_4 and V_2O_3 aqueous stability regimes. The capacitive and cycling performance of the oxide and oxide/gel electrodes were tested in various aqueous environments.

2.2 Experimental Methods

2.2.1 Electrochemical Synthesis

Vanadium oxide films were synthesized using a three-electrode cell comprising a saturated KCl Ag/AgCl reference electrode (0.199 V vs. SHE) from Koslow Scientific, a 5 x 5 cm Pt gauze from Sigma Aldrich as the counter electrode and a 0.5 cm diameter planar Pt electrode for the working electrode and substrate for the vanadium oxide. The films were deposited at 1.1 V vs. Ag/AgCl in 1.0 M $VOSO_4$, 0.1 M Na_2SO_4, pH 1.8 aqueous solution prepared using 18 MΩ Millipore water. A total of 3.0 C of charge was passed. The pH was selected to correspond to the solubility minimum for V_2O_5 under oxidizing conditions [36]. The potentiostatic deposition potential was chosen at the center of the broad deposition peak on an anodic 2 mV s^{-1} linear voltammetric sweep from the open circuit potential until the initiation of oxygen evolution. Following deposition, the films were rinsed in water, 18 MΩ Millipore, and dried either under N_2 flow at 25 °C for approximately 5 min or in a dry oven at 100 ± 10 °C for 30 min, then at 25 °C for an additional 5 min. The vanadium oxide films weighed 0.3 ± 0.1 mg (measured for several samples).

2.2.2 Electrochemical Characterization

The oxides were electrochemically characterized in 1.0 M aqueous KCl at pH 1.8, 3.0, 5.0 or 7.5 using cyclic voltammetry (CV) and galvanostatic charge/discharge (GCD) cycles between potential ranges of -0.15 to 0.85, -0.25 to 0.75, -0.35 to 0.65 or -0.55 to 0.45 V vs. Ag/AgCl, respectively. Arrows in the E-pH diagram shown in Figure 2.2 depict these ranges. The diagram is plotted for three different activities, *a*, of dissolved species, namely 0.01, 1, and 100 (the thickness of the lines separating predominance regions increases with an increase in activity). Although the higher activities are unrealistic for bulk solutions, high concentrations and activity coefficients are not inconceivable in the boundary layers adjacent to electrodes during dissolution.

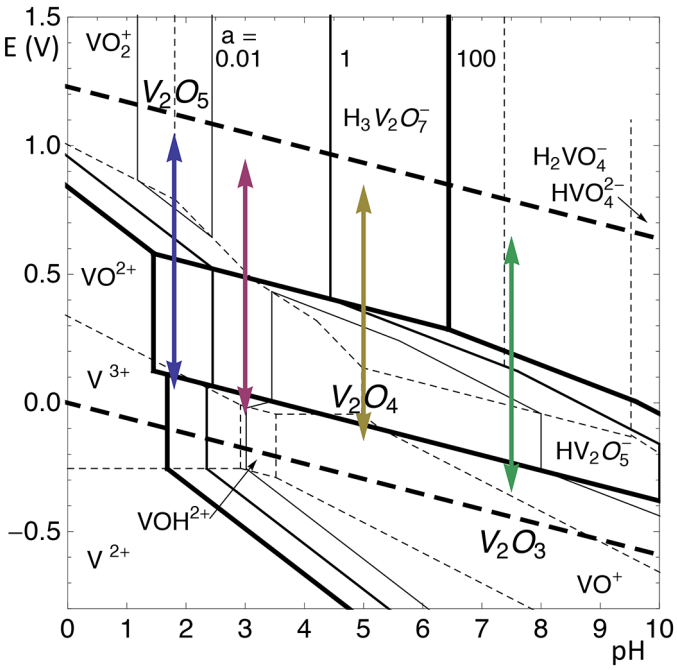

Figure 2.2: E-pH diagram of the vanadium-water system for various activities of the dissolved species plotted at a = 0.01, 1 and 100. Solid lines indicate equilibria involving at least one solid species whereas the dashed lines separate the predominance regions of two dissolved species. The arrows depict the potential ranges (SHE) and pH's at which the vanadium oxide films were tested.

The specific capacitance was calculated from the CV and GCD curves (see Figures 2.3c and 2.3d for examples) using Equations 2.2 and 2.3, respectively, where i is the galvanostatic current, $t_{disch.}$ is the time spent during the discharge portion of the cycle, V_{window} is the potential window, m is the mass of the deposited vanadium oxide film and ν is the CV scan rate.

$$C_{S,CV} = \frac{\int_{disch} i\, dV}{V_{window} \upsilon m} \tag{2.2}$$

$$C_{S,CD} = \frac{i\, t_{disch}}{V_{window} m} \tag{2.3}$$

The electrolyte pH was measured with an Orion, Thermo Scientific 915600 pH electrode connected to an Orion 290A pH meter calibrated with pH 7.0, 4.0 and 1.0 buffer solutions prior to each measurement. The pH of each aqueous KCl solution was adjusted using HCl and KOH. Electrochemical deposition as well as CV and GCD measurements were performed using a PAR 273 potentiostat.

Electrochemical Impedance Spectroscopy (EIS) was performed using a Gamry Series G™ potentiostat and modeled using Echem Analyst™ Software. The impedance of the vanadium oxide films with and without an agar gel coating was measured in 1.0 M aqueous KCl at pH 3.0.

The AC voltage amplitude was set to 10 mV with respect to the open circuit potential vs. Ag/AgCl over a frequency range of 100 kHz to 10 mHz.

2.2.3 Gel Synthesis and Deposition

Gel coatings with an agar concentration of 6.67 g L^{-1} were prepared by dissolving agar powder in either boiling water [37] or 1.0 M KCl at pH 6. Ideally the aqueous phase within the agar gel would be identical to the test electrolyte. After preliminary work had identified pH 3.0 as the most promising pH, gel coatings were also prepared with 1.0 M pH 3.0 KCl. However, because gelation of agar is pH-dependent (gelation involves the formation of helices stabilized by the hydroxyl groups through hydrogen bonding [38], which is disrupted by protonation of the hydroxyl groups at low pH), gels made with 6.67 g L^{-1} agar concentration in pH 3.0 electrolyte were mechanically weak. Therefore some of the pH 3.0 gels utilized 13.34 g L^{-1} agar. Agar solutions were cooled to 50 °C under forced convection for approximately 30 min, by which time visual inspection indicated that gelation had commenced, with concurrent increase in viscosity. The desired volume was drop-deposited on the dry vanadium oxide film. Upon complete gelation, the electrode was transferred to the testing electrolyte.

2.2.4 Compositional and Morphological Characterization

In order to characterize the vanadium materials, they were prepared electrochemically, as described above, but using a modified working electrode that could be removed for *ex situ* examination without disrupting the deposited films. A 7.0 mm square Pt foil was placed over the 0.5 cm diameter planar Pt electrode, which provided electrical connection. A mask made by punching a 0.5 cm diameter hole in a Parafilm® M sheet was placed over the foil to secure it to the Pt electrode while exposing the same surface area as in the previous electrodeposition experiments. After deposition and cycling the Parafilm® M was removed, leaving the vanadium oxide on the Pt foil substrate. The vanadium oxide films were synthesized by anodic potentiostatic electrochemical deposition in 1.0 M $VOSO_4$, 0.1 M Na_2SO_4 at pH 1.8 aqueous solution using 18 MΩ Millipore water at 1.4 V vs. Ag/AgCl until 3.0 C of charge had passed. The potentiostatic deposition potential for the Pt foil electrodes was chosen using the same procedure as the planar Pt electrode as described in section 2.1. Although the electrodes exhibited slightly different polarization behavior, the chosen potential in both cases ensured transport-controlled deposition. After deposition, the films were rinsed in water, 18 MΩ Millipore, and dried under N_2 flow at 25 °C. Agar was prepared and deposited as described in section 2.3. The cycled electrodes were prepared by performing thirty (30) ± 1.67 A g^{-1} GCD cycles in 1.0 M aqueous KCl at either pH 1.8, 3.0, 5.0 or 7.5 between potential ranges of -0.15 to 0.85, -0.25 to 0.75, -0.35 to 0.65 or -0.55 to 0.45 V vs. Ag/AgCl, respectively. The agar coating was removed by briefly contacting with the testing electrolyte at an elevated temperature, approximately 100 °C. All electrodes were then dried under N_2 flow at 25 °C and stored under Ar until further analysis.

Quantitative compositional analysis of the films, on the Pt foil substrates, was performed using a Cameca SX-51 electron microprobe for wavelength dispersive spectrometry (WDS). The morphology of the as-deposited and cycled films was examined with a Leo 430 SEM.

2.3 Results and Discussion

2.3.1 Pseudocapacitive Behavior of As-Deposited Vanadium Oxide

Electrodeposited vanadium oxide films dried at 25 °C under N_2 flow exhibit pseudocapacitive behavior when subsequently cycled using either CV or GCD methods in 1.0 M aqueous KCl at pH 1.8, as shown in Figures 2.3a and 2.3b. The large CV hysteresis and lack of defined peaks indicate that the total capacitive behavior is due not only to double layer charging, but also to reversible redox reactions involving a nearly continuous electron transfer mechanism [11]. This suggests that a pseudocapacitive mechanism such as described in Equation 1.1 could be at work. The film dried at 100 °C in the dry oven exhibited the same basic shape but with lower current density (CV) or faster discharge times (GCD).

The specific capacitance for samples prepared by both drying procedures was calculated from the CV and GCD data using Equations 2.2 and 2.3, and is plotted in Figures 2.3c and 2.3d, respectively. The decrease in capacitance with increasing scan rate would be expected for highly porous materials such as these because the ion intercalation and deintercalation process depends upon mass transfer from the electrolyte through the porous network. Under fast charge/discharge conditions this limits the accessibility of the charge storage potential of the bulk material. The specific capacitance as a function of the time of the discharge half-cycle is shown in Figure 2.3e. The CV and GCD methods appear to be in good agreement based on the overlapping regions.

As the CV scan rate or GCD current is increased, the time required for each cycle decreased. The decrease in capacitance with increasing scan rate or current raises the possibility that the reduced cycle time, rather than the scan rate *per se*, limits the charge stored by pseudocapacitance. The limiting factor may be electrical transport due to the poor electrical conductivity of the oxide, or mass transport associated with intercalation throughout the porous network. For either CV or GCD testing, the film dried at 25 °C with N_2 exhibited a larger pseudocapacitive response than the film dried at 100 °C. This is probably due to a reduction in surface area upon coarsening at the higher temperature. It is also possible that dehydration inhibits wetting of the oxide surface when returned to the electrolyte, making part of the surface inaccessible.

The cycle lives of the as-deposited oxide films were investigated by 500 mV s^{-1} CV and ± 1.67 A g^{-1} GCD analysis as plotted in Figures 2.4a and 2.4b, respectively. The specific capacitance, calculated from each of these cycles using Equations 2.2 and 2.3, is plotted in Figures 2.4c and 2.4d. Whether cycled under CV or GCD, the capacitance of the oxides decreased with protracted cycling, albeit after an initial increase in the case of CV cycling. The drying procedure did not significantly affect the rate of degradation, but since the 25 °C drying procedure gave higher capacitances, all following investigations utilized oxide dried at 25 °C.

It is striking that the capacitance decreased much faster under GCD cycling than under CV conditions, but that the initial capacitance values were much higher for GCD cycling than for CV cycling. A major difference between these two cycling techniques is the time required for a total charge/discharge cycle. Figure 2.3b shows that it took about 280 s for the ± 1.67 A g^{-1} GCD current to complete a single cycle, whereas when scanning at 500 mV s^{-1} the CV scan only took

4 s, almost two orders of magnitude faster. The slower charging under galvanostatic conditions at low current would be expected to yield higher capacitance, given the relatively slow kinetics that would be expected for intercalation. Less obviously, however, the differences in charging/discharging rates could also account for the differences in degradation rate if the degradation mechanism were mass transport limited. Visual inspection revealed that after

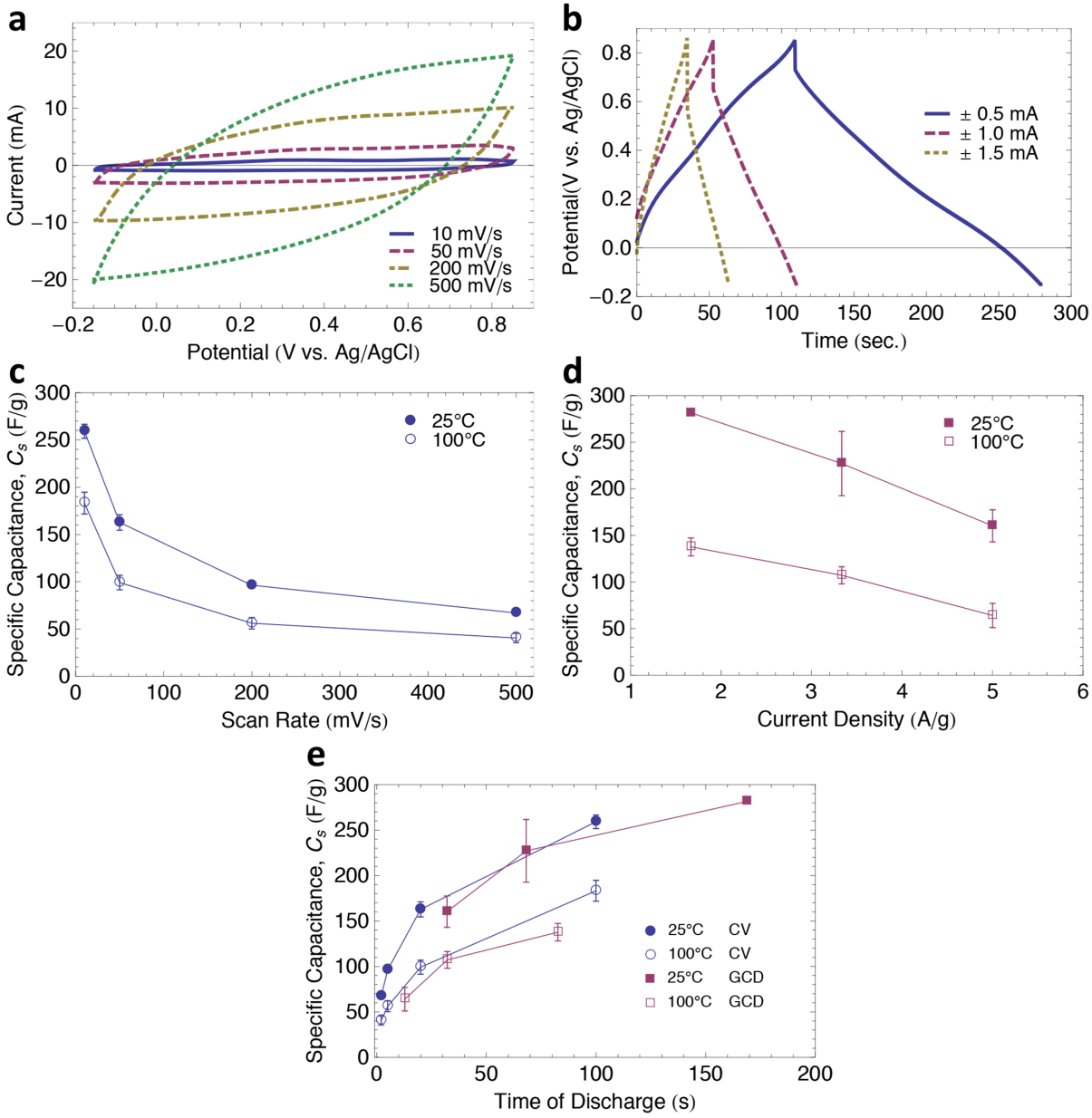

Figure 2.3: As-deposited vanadium oxide films dried at 25 °C and tested in 1.0 M KCl at pH 1.8 using a) CV and b) GCD cycles at various scan rates and currents, respectively. The specific capacitance was then calculated from the c) CV and d) GCD cycles using Equations 2.2 and 2.3, respectively, for both the 25 °C N_2 flow or 100 °C dry oven drying procedures. The specific capacitance e) as a function of the discharge time shows good agreement between the two techniques.

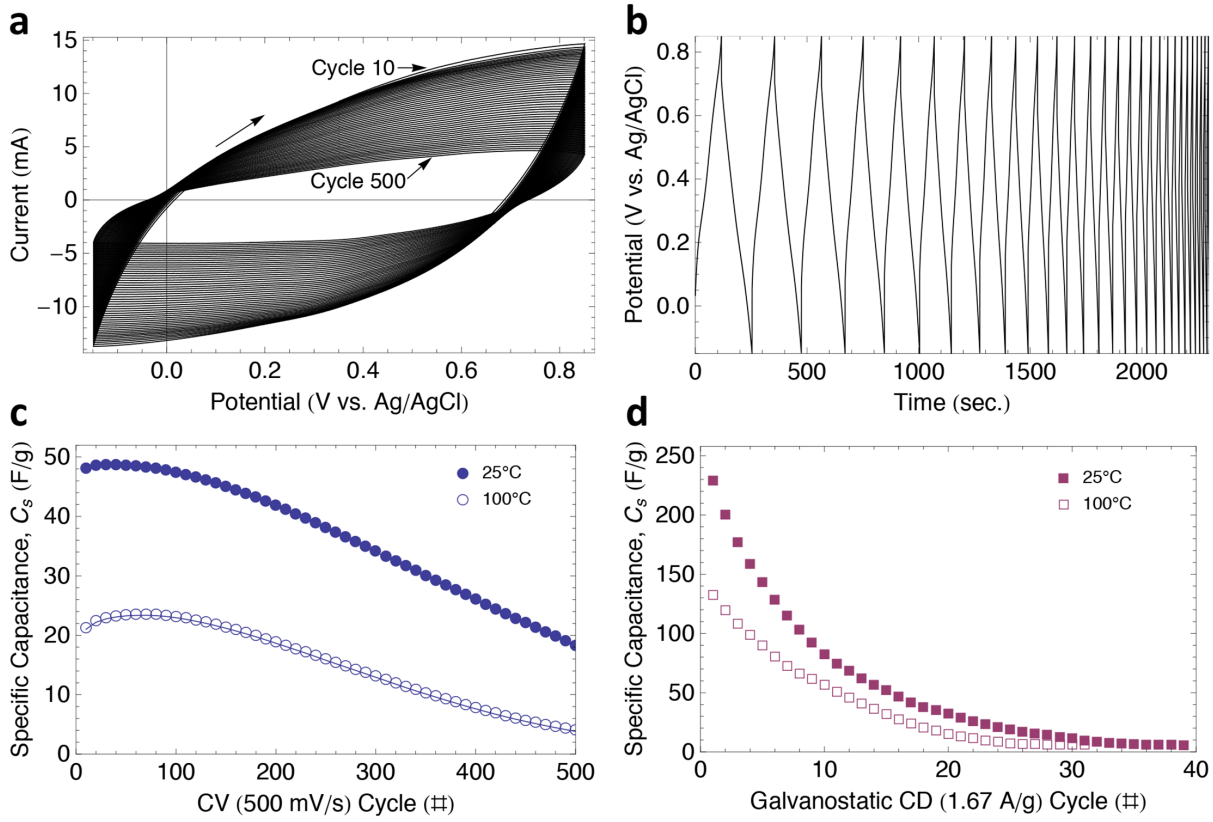

Figure 2.4: Cycle behavior of the as-deposited vanadium oxide dried at 25 °C and tested in 1.0 M KCl at pH 1.8 using a) CV at 500 mV s^{-1} and b) GCD with ± 1.67 A g^{-1}. The cycle lives for both the 25 °C and the 100 °C drying procedures are compared for the c) CV and d) GCD cycling.

cycling, the oxide film coverage on the underlying platinum substrate and its volume were diminished, suggesting partial dissolution of the oxide into the electrolyte. From Figure 2.2, it is evident that at pH 1.8 V_2O_5 is the predominant species at the higher potentials reached during cycling; however, this will be in equilibrium with low activities of VO_2^+ (Equation 2.4) and undergoes reductive dissolution to VO^{2+} at the lower potentials (Equation 2.5) [36].

$$(V_2O_5)_{surface} + 2H^+ \leftrightarrow 2VO_2^+ + H_2O \tag{2.4}$$

$$(V_2O_5^{2-})_{surface} + 6H^+ + 2e^- \leftrightarrow 2VO_2^{2+} + 3H_2O \tag{2.5}$$

Consequently, reductive dissolution would be most pronounced during the cathodic discharge curve when the potential is approaching the lower bound. Therefore, it is instructive to compare the amount of charge passed during the charging and discharging curves of each cycle; differences in these values would suggest irreversible processes. Figure 2.5 reports the ratio of the charge passed during the cathodic discharge half-cycle to the charge passed during the anodic charging half-cycle. A value of 1 is ideal for electrochemical capacitor systems, and a value greater than 1 implies that not all of the charge passed during discharge can be returned to the

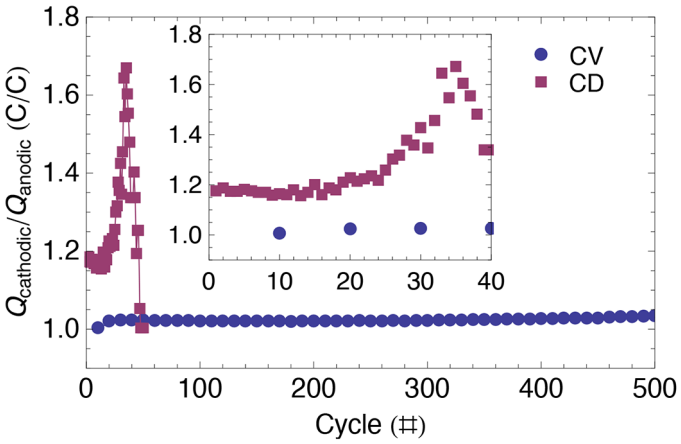

Figure 2.5: Comparison of the ratio of the charge passed during the cathodic discharge half-cycle to the charge passed during the anodic charging half-cycle with cycle life using 500 mV s^{-1} CV and ± 1.67 A g^{-1} GCD on as-deposited vanadium oxide film dried at 25 °C.

oxide during charging. The most likely explanation is that some of the charge is passing as reductive dissolution, rather than solid-state reduction with compensating intercalation, followed by transport of the dissolved V species away from the electrode, so that they are not available for redeposition during the charging half cycle. The deviation from ideal behavior is much more pronounced for the GCD scan, and it appears to increase until cycle 35, at which point the capacitance has declined to zero (Figure 2.4d), and the material has failed. Given the longer cycle times of the GCD conditions, this is consistent with some reductive dissolution. In contrast, during the relatively short CV cycles, less time is available for dissolution and subsequent mass transfer away from the electrode surface, so one would expect less degradation, and hence behavior closer to ideality, in a given cycle.

Although the observed behavior is consistent with reductive dissolution, capacitive degradation may also be due to reduction of the surface area upon cycling, due to smoothing induced by surface diffusion or dissolution/reprecipitation. Smoothing could also be affected by the magnitude of the current passed per cycle. The maximum current passed during the CV cycles was approximately forty (40) times greater than the maximum current tested under GCD conditions. Lower current densities are known to promote smoother, more crystalline structures while higher current densities promote higher surface area nodular or dendritic structures [39]. A reduction in surface area over many cycles would certainly reduce the measured capacitance by limiting the mass transport of intercalation ions to the bulk of the oxide.

2.3.2 Vanadium Oxide Films Using Agar Gel Coating

To further study the degradation of the oxide films, agar gel coatings were applied to reduce the mass transport between the electrode surface and the bulk electrolyte. Agar was selected for the gel barrier because it gels below 50 °C and it is easily dissolved at elevated temperatures. Initially, it was necessary to investigate how the gel would affect the as-deposited vanadium oxide. As shown in Figure 2.6, the pseudocapacitive properties were greatly diminished for agar

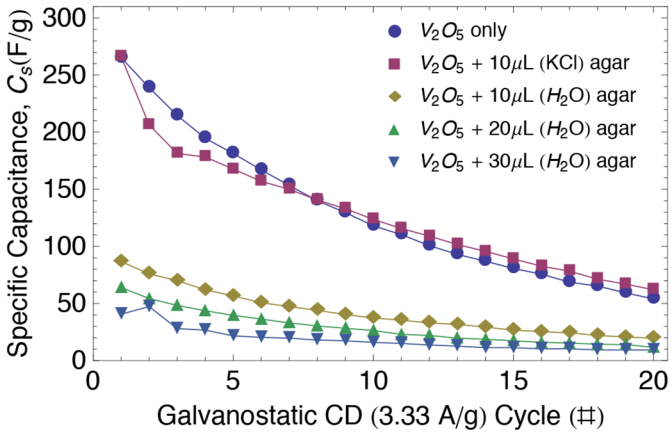

Figure 2.6: Pseudocapacitive behavior of vanadium oxide as-deposited and with various amounts of agar gel prepared with 6.67 g L^{-1} agar in either water or 1.0 M KCl and tested with ± 3.33 A g^{-1} GCD in 1.0 M KCl at pH 1.8.

prepared using only water, particularly for the thickest gel layers. This could indicate that the gel hindered the transport of cations from the testing electrolyte to the surface, thereby reducing ion intercalation, or it could be due to the higher resistivity of the gel. Agar gel prepared using 1.0 M aqueous KCl at pH 6.0 applied over vanadium oxide yielded pseudocapacitive properties strikingly similar to those of V_2O_5 alone. The KCl in the agar gel provides surface proximity for ionic intercalation species and improves the conductivity of the gel.

It is, of course, possible that agar itself contributed to the measured capacitance. Figure 2.7 shows cyclic voltammograms obtained at 50 mV s^{-1} in 1.0 M KCl at pH 1.8 for a clean Pt surface, a 30 µL drop of agar prepared with water and a 30 µL drop of agar prepared with 1.0 M KCl on a clean Pt surface. The agar gel seems to block the Pt surface from H adsorption and Pt oxidation, as indicated by the reduced redox peaks. These peaks are non-capacitive in nature,

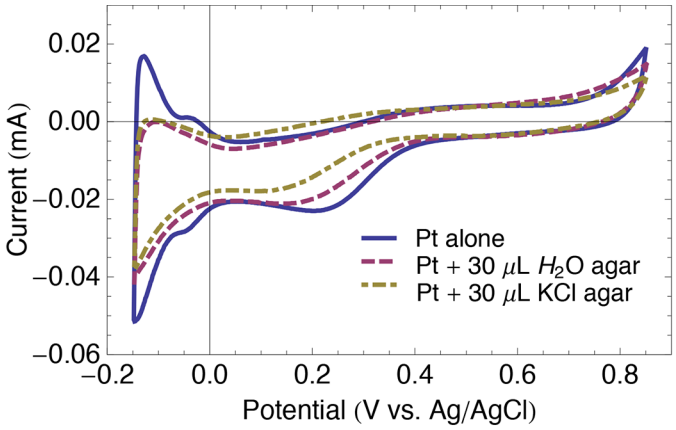

Figure 2.7: Cyclic voltammetry at 50 mV s^{-1} of the Pt alone and with a gel prepared with 6.67 g L^{-1} agar powder in water or 1.0 M KCl.

and thus are ignored when discussing any contribution to the capacitance of the system. When compared to cyclic voltammetry of the oxide alone and the oxide/agar gel electrodes, the contribution from the agar or Pt by hydrogen or chloride adsorption potentially provides less than 2 % to the measured capacitance.

Considering the background contribution to the galvanostatic cycle data, Figure 2.8 plots this percentage over several GCD cycles. The contribution was calculated by performing galvanostatic cycling for the Pt alone as well as Pt with water or KCl based agar then normalizing the capacitance response to the data from the electrodes containing vanadium oxide. The background contribution increases with increasing cycles because the capacitance response from the vanadium oxide decreased. For cyclic voltammetry and galvanostatic cycle measurements, the Pt substrate and agar coating seem to have a relatively insignificant contribution to the overall capacitance.

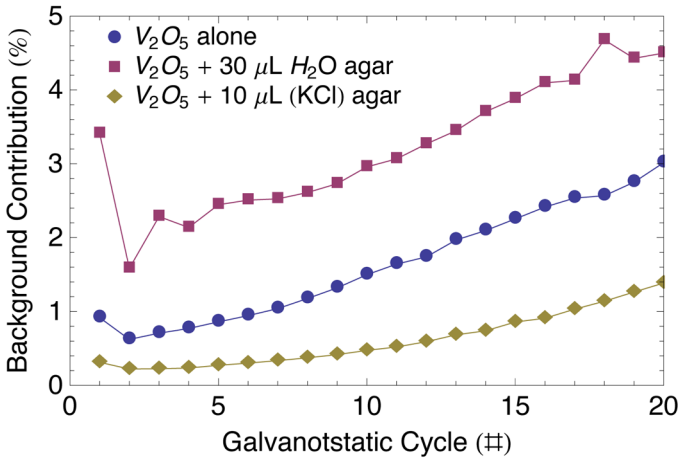

Figure 2.8: Background contribution for galvanostatic cycles of the Pt alone and with a gel prepared with 6.67 g L^{-1} agar powder in water or 1.0 M KCl.

2.3.3 Vanadium Oxide/Gel Cycle Life in Various V_xO_y Stability Regime

It is apparent from Figure 2.6 that even with agar gel inhibiting mass transport, the capacitance of the vanadium oxide films still declined with cycling. In these systems, the agar gel was a modest 10 µL volume dropped over a 0.196 cm^2 planar surface area, providing a very short distance from the electrode surface to the electrolyte, between 0 (at the edge of the oxide) and 0.76 mm (at the center) assuming an oblate semi-spheroidal shape. For comparison, Figure 2.9 shows the effect of cycling on V_2O_5 alone and V_2O_5 with the maximum amount of agar gel that could be dropped on the electrode surface, approximately 400 µL, which coated to the end of the electrode that was encased in a 2.5 mm thick epoxy. The drop also produced an oblate semi-spheroidal shape allowing for a diffusional distance, through the agar gel, between the electrolyte

and the oxide surface between 2.5 and 7.6 mm. This coating increased the diffusional distance by at least a factor of 10.

These systems were tested in 1.0 M KCl at pH 1.8, 5.0 and 7.5 which, as mentioned above, correspond to the V_2O_5, V_2O_4 and V_2O_3 stability region; however, these electrodes were also studied at pH 3.0, which is an intermediate region that corresponds to the maximum stability region for all three solid oxide forms (see Figure 2.2), using a higher agar concentration to ensure gelation. Figure 2.10 demonstrates that the higher agar concentration did not alter the initial capacitance or cycle behavior.

For both the ± 1.67 A g^{-1} GCD and 500 mV s^{-1} CV cycle data, the agar-coated electrodes exhibited an improved cycle life over the oxide alone. The larger volume and thus increased distance from the surface to the electrolyte seems to impede mass transport. Also, for all systems, the cycle life is drastically higher for the CV testing than for the GCD tests. As discussed above, this is most likely due to dissolution-related material loss attributed to longer GCD cycle times or to surface area reduction by surface reconstruction upon dissolution/reprecipitation at the lower currents applied in GCD cycling.

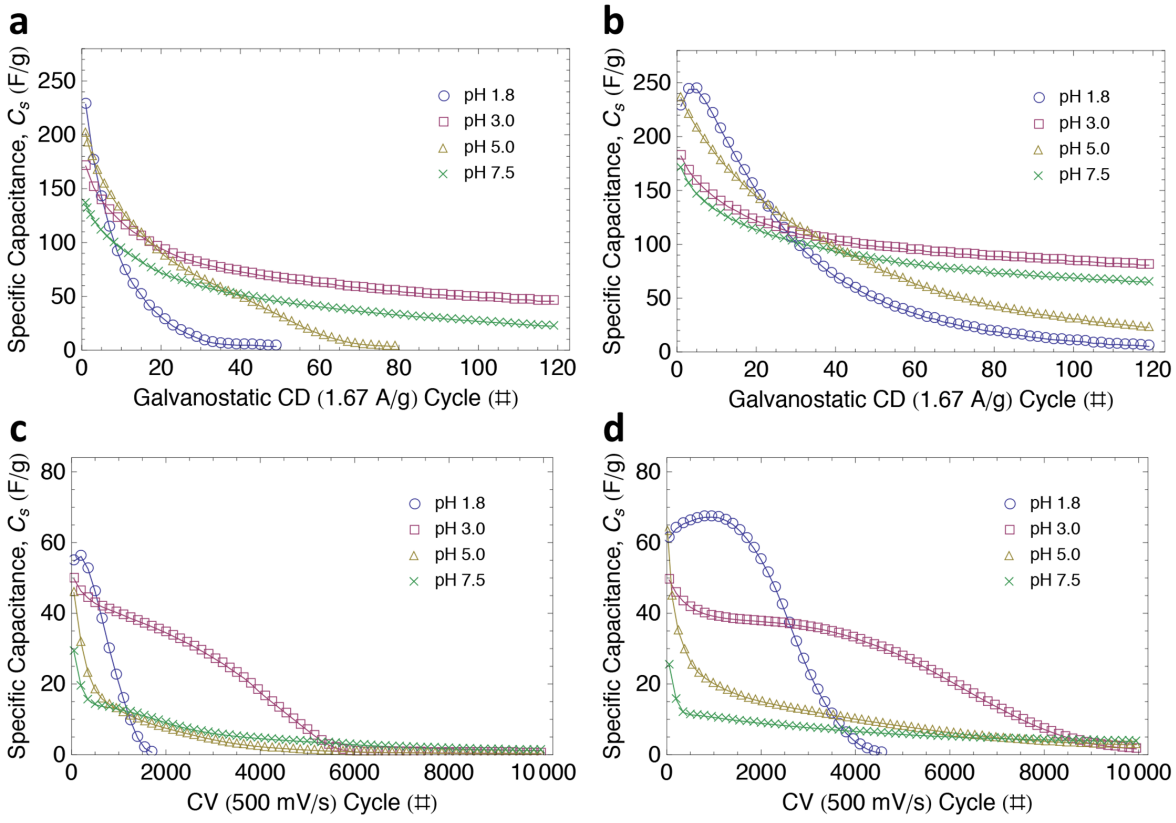

Figure 2.9: Cycle behavior of vanadium oxide using ± 1.67 A g^{-1} GCD on a) V_2O_5 alone and b) V_2O_5 with approx. 400 µL KCl agar gel and tested using 500 mV s^{-1} CV on c) V_2O_5 alone and d) V_2O_5 with approx. 400 µL KCl agar gel.

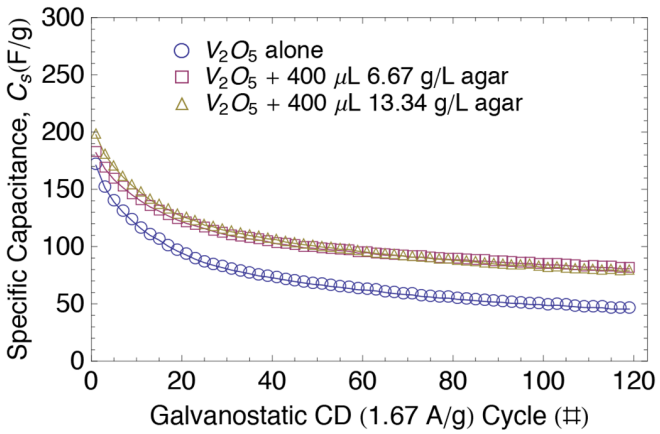

Figure 2.10: Cycle behavior of vanadium oxide using ± 1.67 A g^{-1} GCD on V_2O_5 alone and V_2O_5 with approximately 400 µL agar gel prepared with either 6.67 or 13.34 g L^{-1} agar powder in 1.0 M pH 3.0 KCl.

Examination of the behavior at different pH uncovers trends that exist independent of whether agar coats the oxide surface. The initial capacitance response is largest at pH 1.8; however, the cycle life is inferior to that at higher pH. The small increase in capacitance near the beginning of testing may be due to a surface area increase during the high current CV scans. The initial capacitance was slightly lower at pH 5.0, but the capacitance was retained better over its cycle life. At pH 7.5 the initial capacitance was even lower, but the capacitance retention was better than at pH 5.0. The most promising environment was at pH 3.0; despite its moderate initial capacitance, its superior capacitance retention provided a longer cycle life for both the CV and GCD testing. Since the pH 3.0 environment represents the minimal solubility region, the fact that it exhibits the longest cycle life supports the hypothesis that degradation is dominated by dissolution.

To further explore the electrochemical behavior of the vanadium oxide half-cells, EIS was performed on the three-electrode systems with and without the agar gel coating as well as before and after thirty (30) ± 1.67 A g^{-1} GCD cycles. The Nyquist plot is reported in Figure 2.11a, and the equivalent circuit model used to fit the data is illustrated in Figure 2.11b. The model utilizes constant phase elements (CPEs) rather than capacitive elements to account for the non-ideal behavior of capacitors during EIS. The impedance of the CPEs is described in Eq. 2.6 where ω is the frequency and j is $\sqrt{-1}$. The equation describes the behavior of ideal capacitor elements when the exponents a and b are equal to 1.

$$Z_{CPEa} = \frac{1}{A\,(j\omega)^a} \tag{2.6a}$$

$$Z_{CPEb} = \frac{1}{B\,(j\omega)^b} \tag{2.6b}$$

The resistive parameters, R_S and R_a, represent the equivalent series resistance (ESR) and the charge-transfer resistance, respectively. The constant phase element, CPE_a, is related to the double layer capacitance, and the parallel elements, R_b and CPE_b, have replaced the typical

Warburg impedance and pseudocapacitive elements that represent the passage of DC across the electrode/electrolyte interface [40].

The fitting parameter results are listed in Table 2.1. Comparing the two oxide surface preparations before cycling, the ESR is not significantly different, but the R_a is smaller for the sample containing the agar gel coating. Also, the CPE_a and CPE_b values are larger for the sample with the gel coating, which is consistent with capacitive data in Figure 2.10 where the samples containing agar had a larger initial capacitance as compared to the oxide alone.

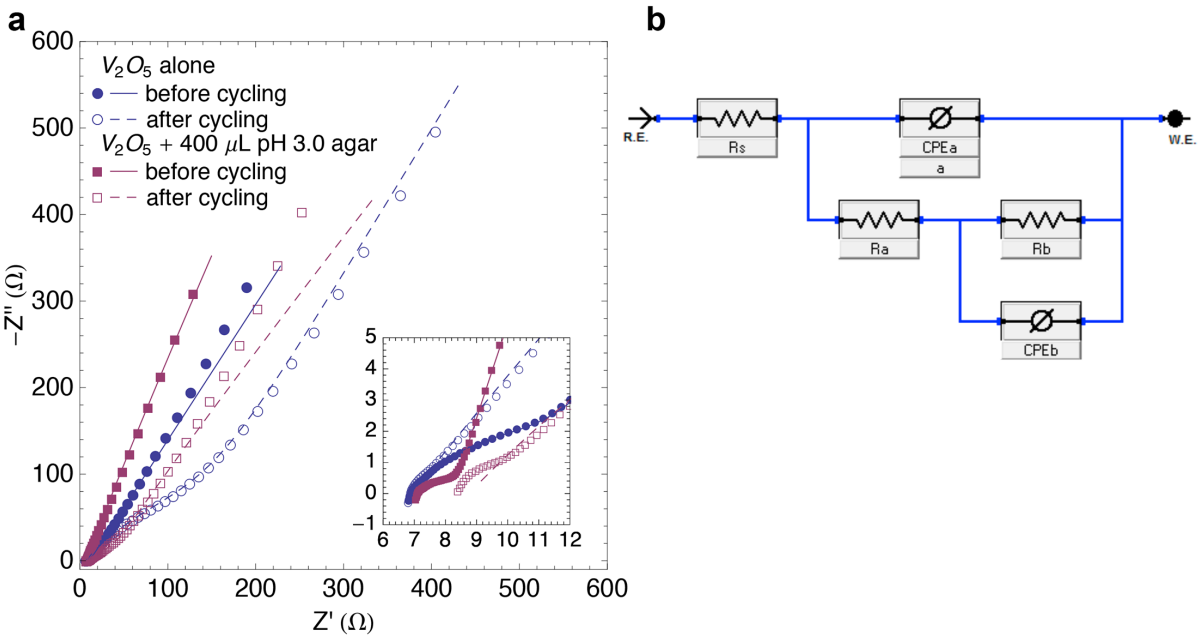

Figure 2.11: EIS (a) Nyquist plot and (b) equivalent circuit model for vanadium oxide with and without 400 µL agar gel prepared with 13.34 g L^{-1} agar powder in 1.0 M pH 3.0 KCl. EIS was performed before and after thirty (30) ± 1.67 A g^{-1} GCD cycles in 1.0 M pH 3.0 KCl. The markers represent the data, and the lines represent the fitted model using the parameters reported in Table 2.1.

Table 2.1: EIS Fitting Parameter Results

Parameter	Units	V_2O_5 alone		V_2O_5 + 400 µL pH 3.0 agar	
		Before cycling	After cycling	Before cycling	After cycling
R_a	ohms	6.2	286.5	1.5	55.2
R_S	ohms	6.9	6.9	7.1	8.8
A (CPE_a)	mS s^a	2.76	3.63	5.89	4.76
a		0.6152	0.5725	0.6226	0.5127
B (CPE_b)	mS s^b	14.0	7.51	20.7	7.00
b		0.6436	0.7193	0.8254	0.6847
R_b	Gohms	0.6	371.3	10.4	684.7
Goodness of Fit		3.86×10^{-4}	5.00×10^{-4}	1.26×10^{-4}	1.60×10^{-3}

Comparing the samples before and after cycling, the resistive elements, R_a and R_b, increase significantly with cycling, and the CPE_b decreases. This result is consistent with the observed capacitive degradation with cycling in Figure 2.10.

Lastly, it is observed that the ESR remains constant during cycling for the oxide without agar; however, the sample with the agar coating exhibits a relatively small increase in ESR after cycling. One possible explanation for this behavior is the accumulation of dissolved species in the agar gel near the oxide surface due to a reduction in mass transport. The presence of the bulky dissolved ionic species in the solution of the gel matrix would likely reduce the electrolyte conductivity. The EIS results appear to be consistent with the cycle behavior observed for the GCD data, and they offer additional support for the hypothesis that dissolution occurs upon cycling.

Further electrochemical support for the dissolution-related degradation hypothesis is provided by Figure 2.12, which relates the degradation rate to the length of discharge for GCD experiments using 10 µL 1.0 M KCl agar at pH 6.0 cycled at ± 1.67 and ± 3.33 A g^{-1}. Whereas Figure 2.12a appears to show two distinctly different curves, Figure 2.12b replots the same data to show the change in capacitance as a function of the time spent during the discharge portion of the cycle. Although the cycle lives differ for the two galvanostatic current conditions, the change in the capacitance seems to depend linearly on the length of time of discharge and be independent of the current itself. A longer cycle time (lower current) would allow for more dissolution and thus more degradation. Thus the behavior depicted in Figure 2.12 further supports the hypothesis that dissolution is responsible for degradation.

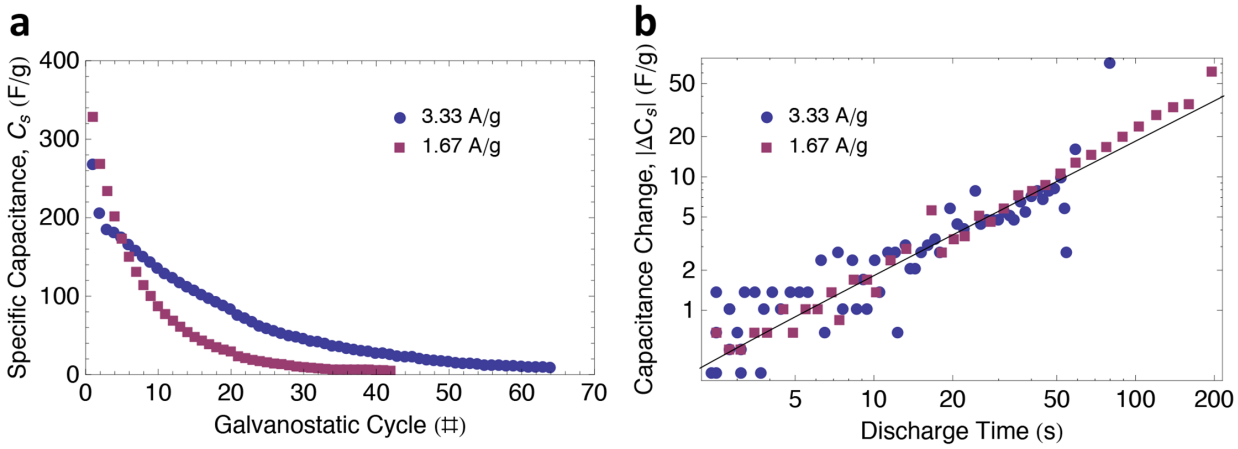

Figure 2.12: Vanadium oxide with a 10 µL 1.0 M pH 6.0 KCl agar coating cycled using GCD cycles at ± 1.67 and ± 3.33 A g^{-1}. This figure reports the same data where a) shows the capacitance behavior over many cycles and b) shows the change in capacitance as a function of the total time passed during discharge.

2.3.4 Quantitative Compositional Analysis with WDS

Compositional analysis of the oxides was performed using WDS. Figure 2.13 shows the composition as a function of the electrolyte pH environment for both the as-prepared and cycled samples. The vanadium oxide was deposited at pH 1.8 and rinsed in water. No Na was detected by WDS, indicating that rinsing was effective. The data points at higher pH values for the as-prepared samples in Figure 2.13a represent oxide films that had been deposited and subsequently coated with an agar film containing an aqueous phase at either pH 3.0 or pH 6.0. The agar was then removed by briefly contacting with the testing electrolyte at an elevated temperature, approximately 100 °C. The cycled samples underwent GCD cycling after coating with agar, which was removed post-cycling. The samples that had had an agar coating applied and removed were not rinsed with water, as the resulting change in pH may have induced compositional changes. Although as much solution as possible was removed before drying the oxides, K^+ and Cl^- are present in all samples that had been coated with gel. The amount of stoichiometric K^+ and Cl^- representing this excess electrolyte was subtracted from the raw data and is not reported in Figure 2.13. For all samples that had been coated with gel, an excess of K^+ was detected in the oxide films, presumably due to intercalation into the oxide. According to the mechanism for pseudocapacitance, K^+ intercalation occurs during the reduction half-cycle to compensate for the negative charge build-up. Therefore, an excess amount of K in the oxide indicates an overall reduction in the vanadium oxidation state.

To examine the data further, the WDS data reported in Figure 2.13 were used to determine the vanadium oxidation state for the various stages of testing. The empirical formula for the vanadium oxide detected by WDS is represented by $N(V_2^{x+}O_x^{2-})$ where $x+$ is the average oxidation state of the vanadium, and the value N is a weighting factor. The stoichiometric relationship between the ionic abundance and oxidation state led to the definitions in Eq. 2.7 where $[X]$ is the WDS-measured concentration of X and $[O^{2-}]_{Kint}$ is the concentration of oxygen whose negative charge is compensated by intercalated potassium ions, namely by the stoichiometric excess of K^+.

$$xN = [O^{2-}] - [O^{2-}]_{Kint}$$

$$2N = [V^{x+}] \tag{2.7}$$

$$[O^{2-}]_{Kint} = \frac{1}{2}K^+_{excess} = 1/2([K^+] - [Cl^-])$$

Solving for x from Eq. 2.7 led to Eq. 2.8 where the WDS data were used to calculate the average vanadium oxidation state.

$$x+ = \frac{2[O^{2-}] - [K^+] + [Cl^-]}{[V^{x+}]} \tag{2.8}$$

The calculated vanadium oxidation state for the as-prepared and cycled samples is reported as a function of pH in Figure 2.14. The as-deposited oxide, which did not contain a gel coating and is represented by the as-prepared data point at pH 1.8, seems to be a mixed oxide between V(IV) and V(V). After the as-prepared samples had been exposed to the higher pH environment of the

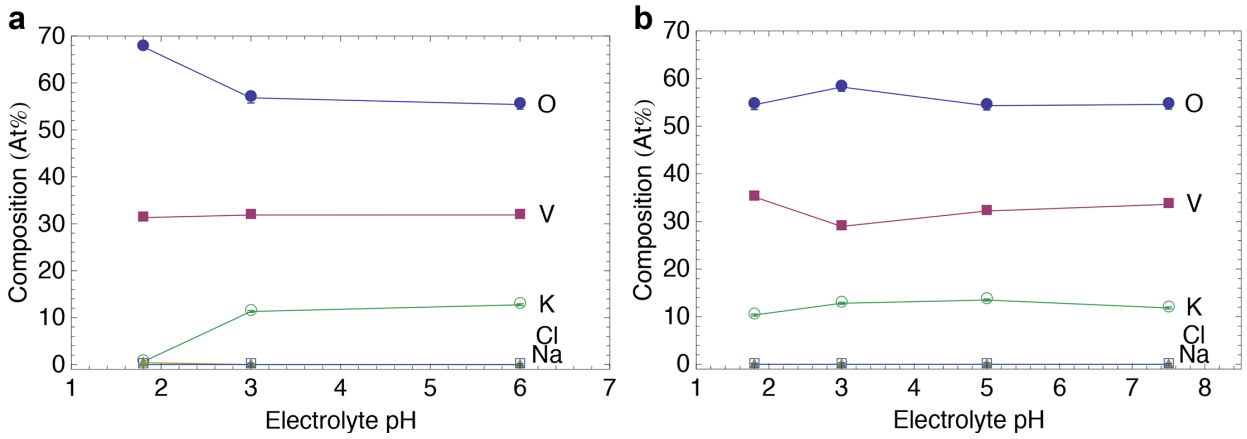

Figure 2.13: Sample composition of the a) as-prepared and b) cycled vanadium oxide electrodes exposed to various pH environments measured by WDS. The amount of stoichiometric K^+ and Cl^- representing excess electrolyte on the surface was subtracted from the data.

gel coatings, the measured oxidation state decreased. For these samples, no potential was applied, so this transition occurred spontaneously. According to Figure 2.2, the solid form most stable at pH 1.8 in the water stability region is the V(V) oxide, V_2O_5. However, at higher pH levels, the stable solid forms are the V(IV) and V(III) oxides, V_2O_4 and V_2O_3, respectively. The increase in local pH seems to induce a reduction in vanadium oxidation state with subsequent K^+ intercalation for charge compensation. After cycling, the oxidation state seems to be approximately the same for pH 1.8, 5.0 and 7.5. The pH 5.0 and 7.5 samples were cycled in potential ranges where solid V(IV) and V(III) as well as dissolved V(V) species are most stable. Over the cycling, the vanadium may have transitioned to a lower oxidation state according to the more thermodynamically favorable state. However, the pH 1.8 environment was cycled in a potential range where solid V(V) and dissolved V(IV) and V(III) are stable. It is possible that

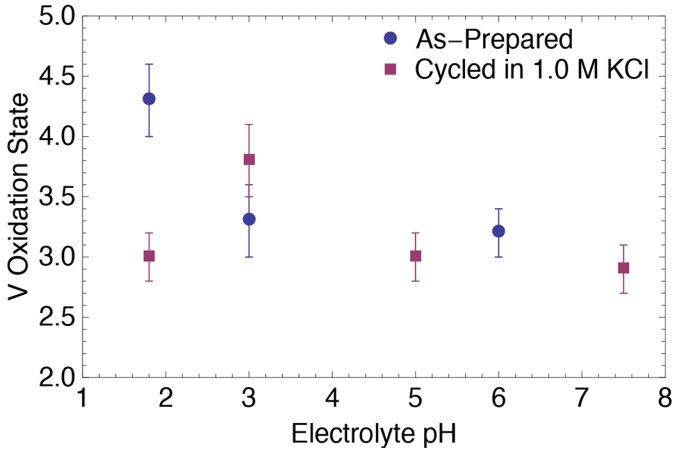

Figure 2.14: Average vanadium oxidation state of the as-prepared and cycled electrodes calculated from WDS data of the samples exposed to various aqueous environments.

over the course of cycling at pH 1.8, the oxide underwent irreversible reductive dissolution, and that dissolved species remaining on the surface were detected in the WDS measurement. The vanadium oxide cycled at pH 3.0 exhibited a much higher oxidation state than oxides cycled at other pHs, and higher than the oxidation state of the as-prepared sample before cycling. Thermodynamically, this pH and potential region corresponds to the minimal solubility of the various solid oxide forms. The higher measured oxidation state could be due to either a relatively higher oxidation state of the solid form, or it could be due to residual dissolved species on the surface.

2.3.5 Morphological Characterization using SEM

Although the electrochemical analysis points to dissolution as the mechanism responsible for degradation of capacitance, the morphology of the films was examined to determine whether surface area reduction upon cycling could also be a contributing factor. Figure 2.15 shows

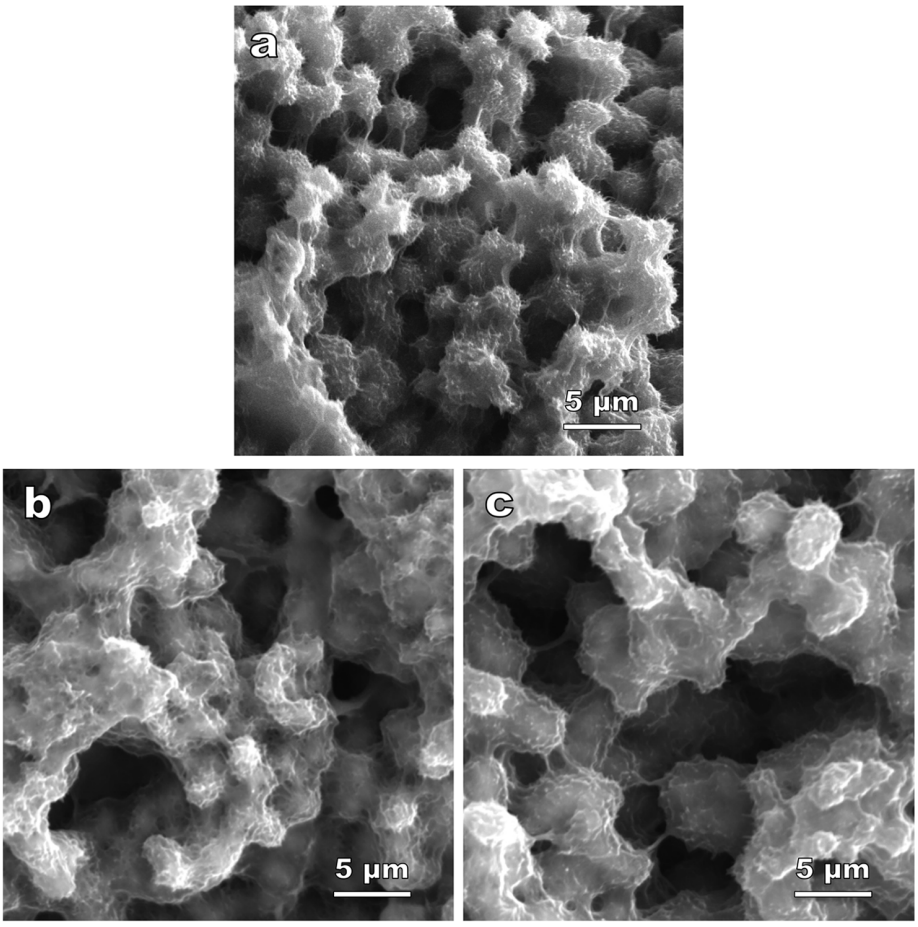

Figure 2.15: Secondary electron images of as-prepared a) vanadium oxide alone, b) vanadium oxide coated with 1.0 M, pH 3.0 KCl agar that was removed before SEM analysis and c) vanadium oxide coated with 1.0 M pH 6.0 KCl agar that was removed before SEM analysis. Agar coatings were removed using electrolyte at approximately 100 °C.

secondary electron SEM images for the as-prepared samples, which were not electrochemically cycled. Samples were prepared with vanadium oxide alone and oxides coated with agar made with 1.0 M aqueous KCl at pH 3.0 and pH 6.0. The gel coating was allowed to set for a few minutes before removal from the oxide surface according to the procedure described in Section 2.2.4 to allow imaging of the oxide surface. The nodular morphology of the vanadium oxide appeared to be unchanged by the agar deposition and removal procedure, but the size of the nodules appeared to increase with increasing pH of the agar. A similar trend was observed for the images of the cycled samples reported in Figure 2.16. These samples were all coated with approximately 400 µL, 1.0 M KCl agar and cycled in 1.0 M KCl at pH 1.8, 3.0, 5.0 or 7.5 by GCD cycling before removing the agar and examining by SEM. As the pH increased, the nodular diameter also increased. This was especially noticeable between the pH 5.0 and 7.5 environments.

A coarser microstructure corresponds to a smaller active specific surface area, and thus the pseudocapacitive response would be reduced. This phenomenon could help to explain the

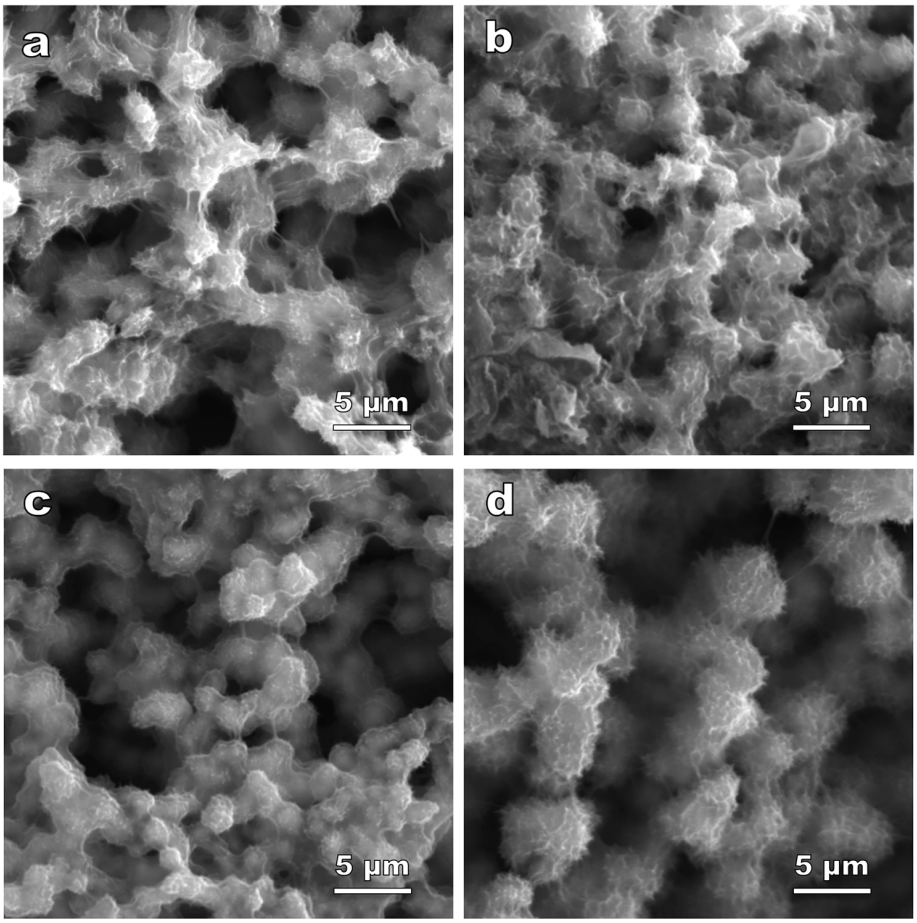

Figure 2.16: Secondary electron images of vanadium oxide samples coated with approx. 400 µL 1.0 M KCl agar after thirty (30) ± 1.67 A g^{-1} GCD cycles in 1.0 M KCl at a) pH 1.8, b) pH 3.0, c) pH 5.0 and d) pH 7.5, followed by removal of the agar coatings using the testing electrolyte at approximately 100 °C.

behavior observed in Figure 2.8, such as the initial increase in measured capacitance of the pH 1.8 sample. The morphology of the sample before and after cycling is represented by the SEM images in Figures 2.15c and 2.16a, respectively. Figure 2.16a indicates that exposure to pH 1.8 reduced the nodular diameter producing a larger surface area. The capacitance is directly related to the active surface area, thus an increase in surface area would increase the measured capacitance. The increase in nodular diameter with increasing pH might, at first sight, be attributed to Ostwald ripening, but this would not be reversible upon pH reduction. Perhaps, upon an increase in pH, an additional swelling is induced by K+ intercalation, which may be reversible with decreasing pH. As cycling continues, oxide dissolution eventually dominates, which results in the sharp decrease in capacitance.

Also observed in Figure 2.8 is the lower initial capacitance but longer cycle life of the oxide tested at pH 7.5 as compared to pH 5.0. Although this could reflect an innate characteristic of the slightly lower oxidation state demonstrated in the WDS results, it could also be due to the larger nodular size and reduced surface area for this environment. The lower surface area microstructure observed in the higher pH environment could in part explain the lower initial capacitance. Furthermore, the lower oxide surface-electrolyte interfacial area would decrease the rate of vanadium oxide dissolution explaining the longer cycle life for the higher pH environment.

Lastly, when comparing the as-prepared and cycled morphologies, although the structure coarsens with increasing pH, it seems invariant upon cycling. With the current image resolution, there does not seem to be a change in the surface area under the tested conditions. Therefore, the capacitive degradation mechanism does not seem to be significantly associated with a change in the vanadium oxide surface morphology.

2.3.6 Degradation Mechanisms in Various Aqueous Environments

Both the electrochemical cycling data and the SEM morphological study support dissolution as the primary degradation mechanism responsible for reduced cycle life. Reductive dissolution to VO^{2+} in pH 1.8 was discussed in section 3.1. However, this species is not the most stable dissolved species for every pH tested, as seen in Figure 2.2. Fortuitously, the agar gel was transparent, making it easy to detect color changes due to dissolved species diffusing away from the electrode surface. Furthermore, the color of vanadium aquo ions depends on the oxidation state. Table 2.2 lists the thermodynamically favorable dissolved species for the various pHs in the potential ranges tested, the color of those dissolved species according to [36] and also the observed color of the gel during cycling.

By comparing the known color of dissolved species that are stable at some potential for a given pH with the observed color of the gel coating during cycling, those species that appear to predominate were identified. These are labeled with asterisks in Table 2.2. The blue-green color of the gel coating during cycling at pH 1.8 suggests reductive dissolution producing high concentrations of VO^{2+}, giving the blue color, and perhaps low activities of VO_2^{+}, known to be a light yellow color, or V^{3+}, which is green, which would give the additional greenish hue. The light yellow color observed in the pH 3.0 system supports oxidative dissolution to $H_3V_2O_7^{-}$, which is orange, but may appear yellow at low concentrations. The pH 5.0 system is similar to

Table 2.2: Predominant Dissolved Species During Cycling				
Solution pH	Dissolved Species	V oxidation state	Solution Color with Dissolved Ion [37]	Observed Gel Color During Cycling
pH 1.8	VO_2^+	V	Light yellow	Blue-green
	$H_3V_2O_7^-$	V	Orange	
	$*VO^{2+}$	IV	Blue	
	V^{3+}	III	Green	
pH 3.0	$*H_3V_2O_7^-$	V	Orange	Light yellow
	VO^{2+}	IV	Blue	
	VOH^{2+}	III	Green	
	V^{3+}	III	Green	
pH 5.0	$*H_3V_2O_7^-$	V	Orange	Yellow
	VO^{2+}	IV	Blue	
	$HV_2O_5^-$	IV	Red-brown	
	VO^+	III	Green	
pH 7.5	$*H_3V_2O_7^-$	V	Orange	Dark brown-yellow
	$*H_2VO_4^-$	V	Colorless	
	$*HV_2O_5^-$	IV	Red-brown	
	VO^+	III	Green	

the pH 3.0 system with a yellow color, albeit more intense. This suggests that a higher concentration of $H_3V_2O_7^-$ was formed and moving through the gel. A dark brown-yellow color was observed during cycling in pH 7.5. This appears to be a combination of $H_3V_2O_7^-$, which diluted could add a yellow tint, $H_2VO_4^-$, which is thermodynamically stable but colorless, and $HV_2O_5^-$, which most likely provides the brown tint.

2.4. Conclusion

Electrodeposited vanadium oxide exhibits pseudocapacitive behavior well-suited for use in electrochemical capacitor electrodes. Unfortunately, it also presents a poor cycle life in aqueous systems due to dissolution upon cycling. Agar gel coatings have been used to control mass transport of the dissolved species, thereby lowering capacitive degradation in all pH environments tested. However, with or without the gel coating the vanadium oxide film tested in the 1.0 M KCl, pH 3.0 environment exhibited the best overall performance. Quantitative compositional analysis found that the vanadium oxidation state is depends somewhat on the pH, but dissolved species remaining on the surface of the electrode may have contributed to the

apparent oxidation state. A study of the oxide morphology showed that the microstructure coarsened with increasing pH, which may partially explain the observed behavior that the oxides cycled at higher pH that exhibited a lower initial capacitance but a longer cycle life. Further study indicated that the microstructure did not change with cycling. Therefore, the electrochemical and characterization data indicate that the dominant mechanism for capacitive degradation is dissolution-related material loss, and the precise dissolved species produced during cycling depend on the pH of the testing electrolyte.

Chapter 3 – Study of Aqueous and Nonaqueous Electrolyte-Solvent Systems

This material has been submitted for publication:

A. M. Engstrom, F. M. Doyle, submitted to Electrochimica Acta (2013).

Abstract

The capacitance and impedance behavior of vanadium oxide electrochemical capacitor electrodes is compared for both aqueous and nonaqueous electrolyte-solvent systems. Alkali metal chloride and bromide electrolytes were studied in aqueous systems, and nonaqueous systems containing alkali metal bromides were studied in polar aprotic propylene carbonate (PC) or dimethyl sulfoxide (DMSO) solvents. Of the electrolytes studied for aqueous systems, the half-cell containing sodium chloride exhibited the highest capacitive performance and a moderate ESR value suitable for high power density devices. In nonaqueous DMSO, lithium bromide exhibited the lowest ESR and highest capacitive performance compared to the other alkali metal bromides. Comparison of the two nonaqueous solvents demonstrates that the PC system performs best at slower cycle rates whereas the DMSO system is best at higher cycle rates.

3.1 Introduction

The solution to the energy crisis will not simply be a single source or technology but a combination of several sources utilizing a variety of different technologies, for both generation and storage of energy. Therefore, it is not surprising that a large increase in the quantity and variety of energy storage research has emerged for devices such as capacitors, batteries and most recently, electrochemical capacitors. Capacitors exhibit very high power density, and batteries are essential for their high energy density. However, electrochemical capacitors show significant promise for applications where both high energy and high power density are needed [1,10].

Electrochemical capacitors (ECs) include two types of devices distinguishable by the dominant energy storage mechanism. Electrochemical double layer capacitors, which include high surface area carbon materials, store energy in the double layer that exists at the electrode-electrolyte interface. The charge-storage is electrostatic in nature, involving no electron transfer across the interface. In contrast, the second type of device, the pseudocapacitor, stores energy mainly by

highly reversible redox reactions at the surface of the material, for example by changing the oxidation states in transition metal oxides, accompanied by the intercalation and deintercalation of electrolyte ions to maintain charge neutrality. ECs are valued for their high capacitance, high specific power and energy density, long cycle life as well as low material cost and toxicity [1,10-13]. Vanadium oxide is a desirable active material due to its wide range of stable oxidation states (V, IV, III and II) and its relatively low cost and toxicity compared to RuO_2 [6,17]. The capacitive properties and degradation mechanisms for electrodeposited vanadium oxide were previously studied in a variety of pH environments using aqueous KCl electrolyte solutions [41].

The specific energy and maximum specific power density, E_s and P_s, respectively, are calculated [1,10,11,13] by:

$$E_s = \frac{1}{2} C_s V^2 \tag{3.1}$$

$$P_s = \frac{V^2}{4\,ESR\,m} \tag{3.2}$$

where C_s is the specific capacitance calculated from cyclic voltammetry (CV) or galvanostatic charge/discharge (GCD) experiments as previously reported, V is the operating voltage, ESR is the equivalent series resistance and m is the mass of the electrode material. These equations assume purely capacitive behavior, and although they may not represent the true energy and power density for the complex pseudocapacitive system studied here, they act as common benchmarks used in the literature, and therefore are useful for comparison purposes. However, these equations will not be calculated until later chapters. They are simply mentioned here in order to refer to the significance of the operating voltage and ESR values that differ between the various electrolyte-solvent systems and how they pertain to the energy and power density.

Although aqueous solutions generally have very low ESR due to high ionic conductivities that ensure high pulsed-power capabilities, the relatively small electrochemical stability window of water limits the operating cell voltage and thus limits the energy density. Organic electrolytes and room-temperature ionic liquids (RTILs) allow for much larger voltage windows, but their relatively higher resistance, toxicity, cost and the potential flammability of some organic solvents create other challenges [1,11]. Depending on the power and energy specifications of a given application, either system may be more or less appropriate; therefore, both aqueous and nonaqueous systems warrant further study. The most commonly studied nonaqueous systems utilized $LiClO_4$ in propylene carbonate (PC) [26,29,31,33,42-44], and one group studied a lithium-containing room temperature ionic liquid [44]. PC is widely used for EC applications because it is a highly polar, aprotic solvent with a high dielectric constant and a large electrochemical stability window [45], and lithium perchlorate is an attractive electrolyte for PC due to its high solubility [46]. Dimethyl sulfoxide (DMSO) is another potentially useful polar aprotic solvent. Although it has a slightly lower dielectric constant and a relatively smaller electrochemical potential stability window compared to PC, it has a higher donicity, lower viscosity and relatively higher ionic conductivity [1,45]. The solubilities of alkali metal electrolytes follow the trend $ClO_4^- > Br^- > Cl^-$ in PC [46], and $NO_3^- > Br^- > Cl^-$ for DMSO [47]. Although perchlorates are also highly soluble in DMSO, they are known to be explosive in organic solvents, particular in DMSO [48,49]. Therefore, the electrolytes with the highest

solubility and compatibility in both PC and DMSO are the alkali metal bromides. For both PC and DMSO, the alkali metal bromides follow the trend for solubility LiBr > NaBr > KBr. The solubility limit of KBr and LiBr in PC is 0.003 M and 1.10 M, respectively; the solubility of KBr and LiBr in DMSO is 0.55 M and 3.61 M, respectively [46-48].

The most commonly studied aqueous systems with vanadium oxide electrodes include various aqueous alkali metal chlorides [6,19,21,23,25,42,50], sulfates [17,24,51,52] and nitrates [52]. It has been reported that ECs containing alkali metal nitrate and chloride electrolytes exhibit a slightly higher capacitance than sulfate electrolytes owing to their relatively smaller size, and thus faster chemisorption [52,53]. Therefore, for the aqueous electrolyte study a variety of alkali metal chlorides were chosen along with bromides due to their high solubilities [54], and to allow comparison with the nonaqueous alkali metal bromide-solvent systems.

In the current study, electrodeposited vanadium oxide electrodes were studied in aqueous solutions containing alkali metal bromides and chlorides adjusted to pH 3.0 based on previous work performed in a wide range of pH environments with this material [41]. In addition, solutions containing alkali metal bromides in PC, DMSO and a mixture of the two solvents were studied for nonaqueous electrolyte-solvent systems.

3.2 Experimental Methods

3.2.1 Electrochemical Synthesis

Vanadium oxide films were synthesized using a three-electrode cell comprising a saturated KCl Ag/AgCl reference electrode (0.199 V vs. SHE) from Koslow Scientific, a 5 x 5 cm^2 Pt gauze from Sigma Aldrich as the counter electrode and a modified 0.5 cm diameter planar Pt electrode for the working electrode and substrate for the vanadium oxide. In order to characterize the vanadium materials, the working electrode was modified to facilitate removal for *ex situ* examination without disrupting the deposited films [41]; a 7.0 mm square Pt foil was placed over a 0.5 cm diameter planar Pt electrode, which provided electrical connection. A mask made by punching a 0.5 cm diameter hole in a Parafilm® M sheet was placed over the foil to secure it to the Pt electrode while exposing the same 0.5 cm diameter surface area. The films were deposited at 1.4 V vs. Ag/AgCl in 1.0 M $VOSO_4$, 0.1 M Na_2SO_4, pH 1.8 aqueous solution prepared using 18 MΩ Millipore water. A total of 3.0 C of charge was passed. The pH of 1.8 corresponds to the solubility minimum for V_2O_5 under oxidizing conditions [28,36]. The potentiostatic deposition potential was chosen at the center of the broad deposition peak on an anodic 2 mV s^{-1} linear voltammetric sweep from the open circuit potential until the initiation of oxygen evolution. Following deposition, the films were rinsed in water, 18 MΩ Millipore, and dried under N_2 flow at 25 °C for approximately 5 min. The vanadium oxide films weighed 0.3 ± 0.1 mg (measured for several samples).

3.2.2 Electrolyte Solution Preparation

The vanadium oxide electrodes were studied in both aqueous and nonaqueous electrolyte-solvent systems.

Aqueous electrolytes were prepared with 18 MΩ Millipore water. According to previous results, the optimal pH region for the vanadium oxide system in KCl was found to be pH 3.0 [41]. Consequently, all aqueous electrolytes were adjusted to pH 3.0. The electrolyte pH was measured with an Orion, Thermo Scientific 915600 pH electrode connected to an Orion 290A pH meter calibrated with pH 7.0, 4.0 and 1.0 buffer solutions prior to each measurement. Electrolytes containing chlorides were adjusted using HCl, and electrolytes containing bromides were adjusted using H_2SO_4.

Electrolyte solutions in nonaqueous solvents were prepared in a dry glove box under a nitrogen environment. Propylene carbonate (PC) was stored over 5 Å molecular sieves and dimethyl sulfoxide (DMSO) was stored over 4 Å molecular sieves to remove any contaminant water content. All solvents and molecular sieves were purchased from Alfa Aesar. Each batch of molecular sieves was checked for activity prior to use by measuring a temperature change of at least 4 °C when a small amount of water was dropped over a test sample of the molecular sieves. Electrolytes were weighed in air outside the dry box in sample containers that had been cleaned in 18 MΩ Millipore water and dried at approximately 90 °C. The containers containing the electrolytes were immediately transferred to the dry box where the samples underwent several evacuation and backfill steps to exchange the atmosphere with dry nitrogen. In the dry box the solvents were decanted from their storage containers to prepare the individual electrolyte solutions.

3.2.3 Half-Cell Design

The vanadium oxides were characterized electrochemically in three-electrode cells that varied with the type of solvent. The aqueous half-cells were comprised of a 5 x 5 cm^2 Pt gauze from Sigma Aldrich as the counter electrode aligned parallel to the electrodeposited vanadium oxide as the working electrode with a saturated KCl Ag/AgCl reference electrode (0.199 V vs. SHE) from Koslow Scientific positioned immediately adjacent to the working electrode surface, all immersed in the electrolyte solutions. The nonaqueous half-cells contained the same working and counter electrodes as the aqueous systems; however, the reference electrode differed. The preferred electrode for the nonaqueous systems was a 1 mm diameter leak-free (LF) Ag/AgCl reference electrode (measured at 0.223 V vs. SHE) from Harvard Apparatus designed for DMSO and similar solvents. However, the limited solubility and high solution resistance of the 0.3 M nonaqueous electrolytes, particularly the KBr and NaBr solutions, prevented the utilization of this electrode. Therefore, a Pt wire was used as a pseudo-reference for the alkali metal bromide study in DMSO (see Figure 3.3). All other nonaqueous electrochemical characterization was performed with the LF Ag/AgCl reference electrode due to the higher conductivity of the LiBr electrolyte. The aqueous systems were assembled in air, and the nonaqueous cells were assembled in the dry box under nitrogen. They were sealed with Parafilm® M, and removed from the dry box to gain access to the potentiostats.

3.2.4 Electrochemical Characterization

The vanadium oxides were electrochemically characterized using cyclic voltammetry (CV) and galvanostatic charge/discharge (GCD) cycles. The aqueous systems were characterized between -0.25 and 0.75 V vs. Ag/AgCl, and the nonaqueous systems were tested between -0.5 and 1.5 V vs. LF Ag/AgCl for the half-cells containing PC and between -0.9 and 1.1 V vs. LF Ag/AgCl for the cells containing DMSO. For the half-cells cycled with respect to the Pt pseudo-reference, the potential of the Pt wire was measured vs. LF Ag/AgCl between each experiment to maintain a constant potential range. The 0.3 M KBr in DMSO was cycled between -1.3 and 0.7 V vs. LF Ag/AgCl, but the NaBr and LiBr were both cycled between -0.9 and 1.1 V vs. LF Ag/AgCl. The nonaqueous half-cell potential ranges were chosen based on CV symmetry and electrolyte-solvent system electrochemical stability. The potentiostatic electrochemical deposition, CV and GCD measurements were performed using a PAR 273 potentiostat.

Electrochemical Impedance Spectroscopy (EIS) was performed using a Gamry Series G™ potentiostat and modeled using Echem Analyst™ Software. The impedance of the vanadium oxide films in the various electrolyte solutions was measured using an AC voltage amplitude of 10 mV with respect to the open circuit potential at frequencies from 100 kHz to 10 mHz unless otherwise noted.

3.2.5 Morphological and Compositional Characterization

After deposition and cycling any remaining Parafilm® M was removed, leaving only the vanadium oxide on the Pt foil substrate. The morphological and qualitative compositional analyses were performed with a Leo 430 SEM equipped with EDS.

3.3 Results and Discussion

3.3.1 Aqueous Systems

The specific capacitance of vanadium oxide electrodes was calculated using both CV and galvanonstatic CD testing methods. The specific capacitance of the half-cells containing various aqueous electrolyte solutions is reported in Figure 3.1. The broad peaks observed in Figure 3.1c at 10 mV s^{-1} are indicative of a pseudocapacitive mechanism, and it is consistent with the behavior reported previously for 1.0 M KCl at various pH [41]. For both testing methods and anions tested, the capacitance decreased with the following trend for the alkali metal cations: $Na^+ > K^+ > Li^+$. This trend is consistent with results for vanadium oxide tested with alkali metal sulfates and nitrates [52] as well as manganese oxide tested in alkali metal chlorides [53].

In order to more fully understand the interaction between the vanadium oxide electrode and the electrolyte solutions, the aqueous half-cells were further characterized by EIS as shown by the Nyquist plot in Figure 3.2a. The markers indicate the experimental data collected between 100 kHz and 10 mHz, and the corresponding lines plot the fitted equivalent circuit model illustrated in Figure 3.2b. The model impedance is calculated by:

$$Z = Z' + jZ'' = R_s + \frac{1}{A(j\omega)^a + \frac{1}{R_a + \frac{1}{\frac{1}{R_b} + jC_b\omega} + \frac{1}{W\sqrt{j\omega}}}} \quad (3.3)$$

where *Z'* and *Z''* are the real (resistive) and imaginary (capacitive) components of *Z*, the total impedance. R_s is the equivlent series resistance or ESR, ω is the frequency in Hz, j is $\sqrt{-1}$ and the term $1/[A(j\omega)^a]$ is the impedance of the constant phase element, CPE_a, related to the double layer capacitance where $0 < a < 1$. Values of a less than 1 indicate deviation from ideal capacitive behavior. R_a is related to the interfacial charge transfer resistance. C_b and R_b are the elements related to pseudocapacitance arising from charge transfer across the electrode-electrolyte interface, and $1/[W\sqrt{j\omega}]$ is the diffusional Warburg impedance associated with a porous electrode [10,40].

The parameters used in the fitted model in Figure 3.2 are reported in Table 3.1. The R_s or ESR values reported agree well with the experimental data shown in the inset graph in Figure 3.2a, which shows the high frequency domain of the impedance response. The R_s value is defined as the point at which the imaginary component, *Z''*, goes to zero [1]. The ESR is relatively independent of the anion but decreases with increasing size of the cation. This result may be explained by the relative mobilities of the ions in solution. Hydrated chloride and bromide ions exhibit very similar mobilities, but the ionic mobility of alkali metal cations is known to increase significantly with increasing atomic number of the cation. Although the hydration numbers in the first solvation shell increase with increasing cation size, the strength of the interaction between the ion and the hydrating water molecules decreases. This is demonstrated by the reduced exchange kinetics of the water molecules in the solvation shell surrounding smaller cations thus leading to lower ionic mobility with decreasing atomic number [55,56]. In fact, the lithium ion is known to retain a second solvation shell thus increasing its effective ionic radius in aqueous solutions [57]. Therefore, this effect would suggest that the largest cation, K^+, would promote the best performance, and indeed, the ESR values follow this trend. However, once at the surface the solvation shell(s) is(are) stripped from the cation, and the overall capacitance benefits from the smaller cations allowing for higher density packing during adsorption or intercalation. This effect suggests the opposite trend, that the smaller ion, Li^+, would produce the largest capacitance. Therefore, these competing factors may very well explain the higher overall capacitance observed with the intermediate sodium cation, which exhibits a higher mobility in solution compared to Li^+ and a smaller ionic radii compared to K^+ after desolvation.

Although the ESR values did not change significantly with the anion of the salt solutions, the measured capacitance was slightly larger for the chloride salts than the bromides when the solution contained Na^+ or K^+ cations and when the scan rates or current densities were high. As the scan rate and current density decreased, the capacitances with the bromide and chloride electrolytes were comparable. It has been reported that ECs containing alkali metal nitrate and chloride electrolytes exhibit a slightly higher capacitance than sulfate electrolytes [52,53]. These studies attributed the improved capacitance to the relatively smaller size, and thus faster chemisorption of the nitrate and chloride anions, compared to sulfate. However, the current study can not be fully explained by the size of the anion alone due to the differing behavior observed for the electrolytes containing lithium. Unlike the potassium and sodium salts, the vanadium oxide exposed to the LiBr electrolyte exhibited a much larger capacitance than the

LiCl electrolyte. The exchange kinetics of the water molecules in the solvation shells surrounding bromide are slightly faster than for chloride but both are much faster than the those in the solvation shell surrounding lithium [56]. The much slower mobility of the lithium cation may result in a larger dependence of the capacitive performance on the anion mobilities.

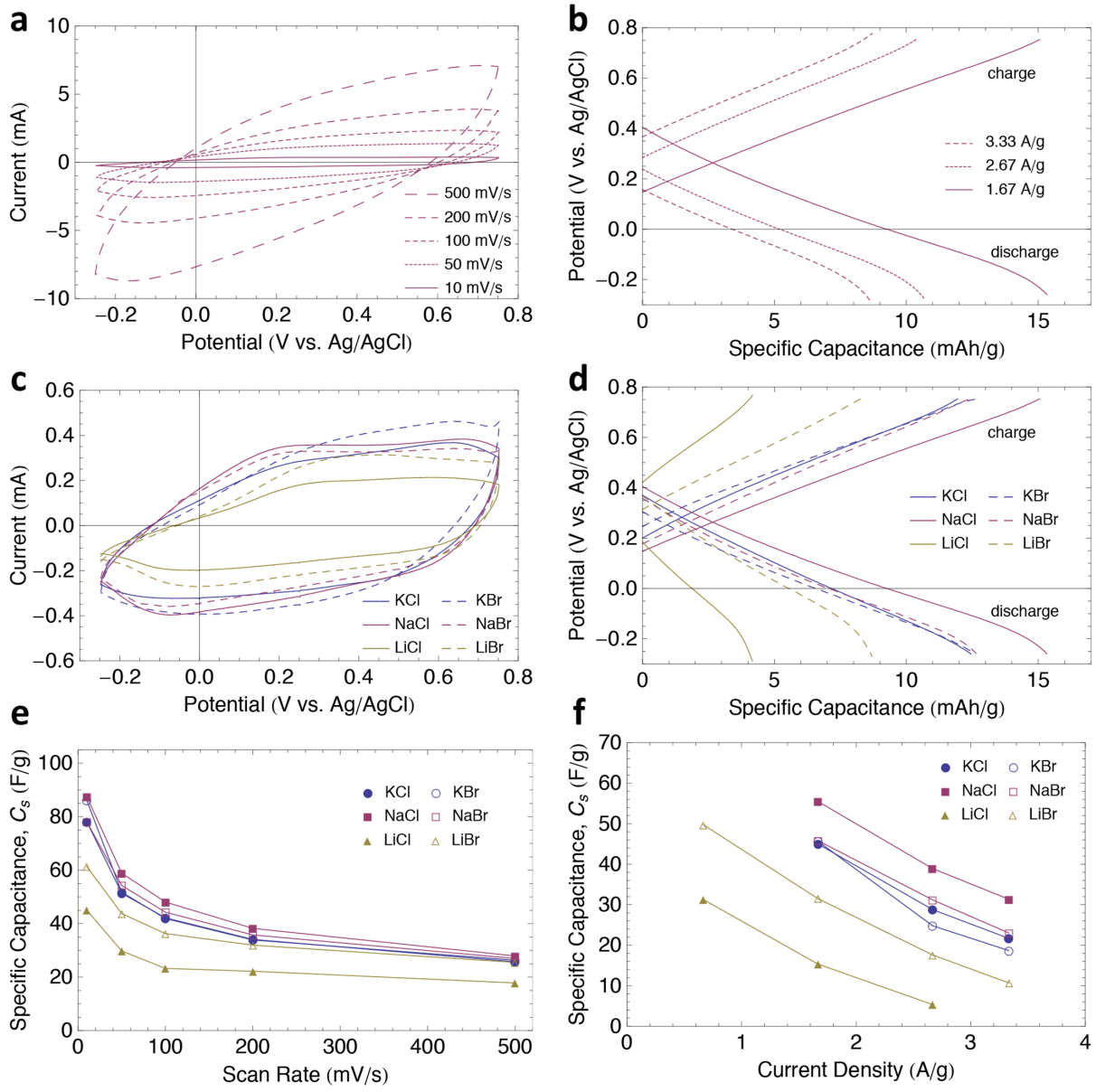

Figure 3.1: The pseudocapacitive characteristics of electrodeposited vanadium oxide in various aqueous electrolytes were studied using CV and GCD methods: a) CV curves at various scan rates and b) GCD profiles for various current densities in 3.0 M NaCl at pH 3.0; c) CV curves at 10 mV s^{-1} and d) 1.67 A g^{-1} GCD profiles for various aqueous electrolyte solutions; the capacitance of aqueous half-cells was calculated from e) CV and f) GCD for various 3.0 M electrolytes at pH 3.0.

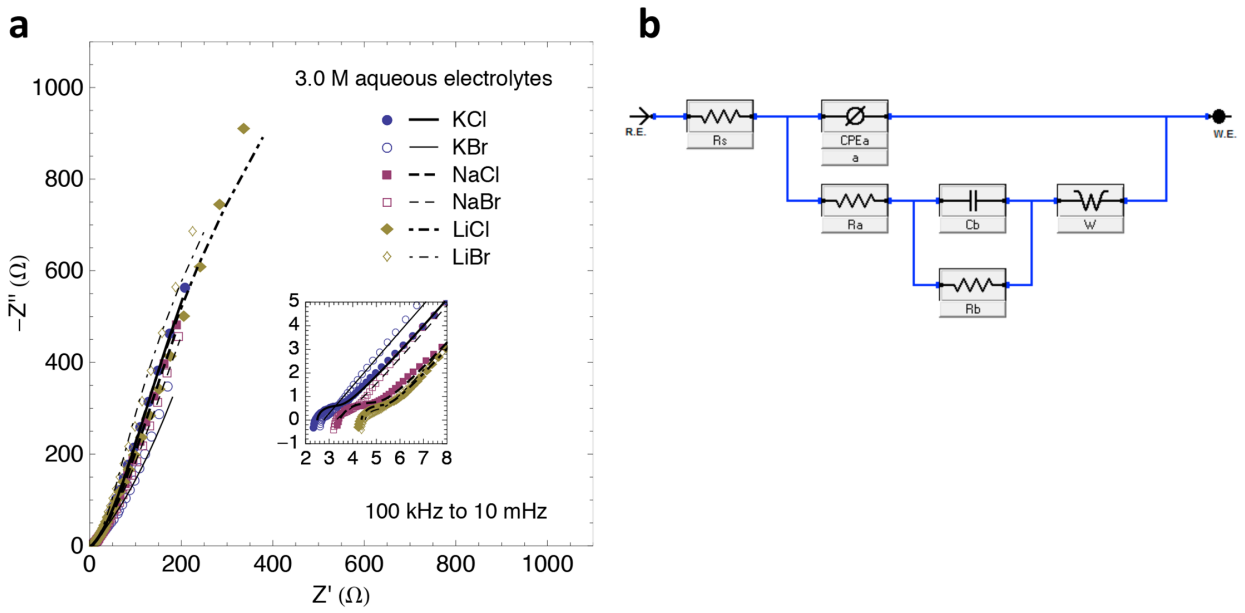

Figure 3.2: EIS a) data and b) equivalent circuit model for aqueous half-cells with various 3.0 M electrolytes at pH 3.0. The markers represent the real data and the corresponding lines represent the fitted model with parameters reported in Table 3.1. The inset graph depicts the high frequency region of the EIS data and fitted model.

Table 3.1: Fitting Parameters for EIS Modeling of Aqueous Systems at pH 3.0

Electrolyte	R_s (Ω)	A ($S \cdot s^a$)	a	R_a (Ω)	C_b (F)	R_b (Ω)	W ($S \cdot s^{0.5}$)	Goodness of Fit
3.0 M KCl	2.500	2.69×10^{-5}	0.9973	0.8377	4.114×10^{-2}	3.533×10^{3}	1.78×10^{-2}	1.61×10^{-3}
3.0 M KBr	2.777	1.30×10^{-3}	0.7524	0.2865	1.046×10^{-1}	1.465×10^{9}	1.47×10^{-2}	1.51×10^{-3}
3.0 M NaCl	3.439	1.63×10^{-4}	0.7740	1.6620	4.920×10^{-2}	3.280×10^{3}	1.82×10^{-2}	9.68×10^{-4}
3.0 M NaBr	3.317	1.36×10^{-3}	0.6751	0.6594	4.991×10^{-2}	4.462×10^{3}	1.52×10^{-2}	1.22×10^{-3}
3.0 M LiCl	4.376	1.59×10^{-5}	1.0000	0.8733	2.179×10^{-2}	2.960×10^{3}	1.38×10^{-2}	4.46×10^{-4}
3.0 M LiBr	4.537	4.83×10^{-5}	0.9703	0.6202	2.703×10^{-2}	2.842×10^{3}	2.10×10^{-2}	5.87×10^{-4}

The preferred electrolyte in aqueous solutions for electrochemical capacitor applications must exhibit both low ESR values for optimal power output as well as high capacitance for optimal energy density. The combination of the moderately low ESR as well as the high capacitive performance of the NaCl electrolyte solution demonstrates that it is a suitable system for aqueous vanadium oxide electrochemical capacitor devices.

3.3.2 Nonaqueous Electrolyte-DMSO Systems

In addition to the study of aqueous electrolyte solutions, nonaqueous systems were tested in vanadium oxide half-cells.

The specific capacitance of the vanadium oxide electrode in 0.3 M alkali metal bromide electrolytes in DMSO is reported in Figure 3.3. This experiment was not duplicated in PC due to the much lower solubilities of NaBr and especially KBr (0.003 M) [46]. Over the tested scan rates, LiBr exhibited the largest pseudocapacitive response followed by KBr and then NaBr. This is the opposite of the trend observed in Figure 3.1 for aqueous electrolytes.

These DMSO systems were further studied using EIS between 10 kHz and 10 mHz, and the results are reported as a Nyquist plot in Figure 3.4a. The markers represent the experimental data, and the corresponding lines plot the fitted equivalent circuit model illustrated in Figure 3.4b. The model is comparable to that used for the aqueous half-cells in Figure 3.2b, except that

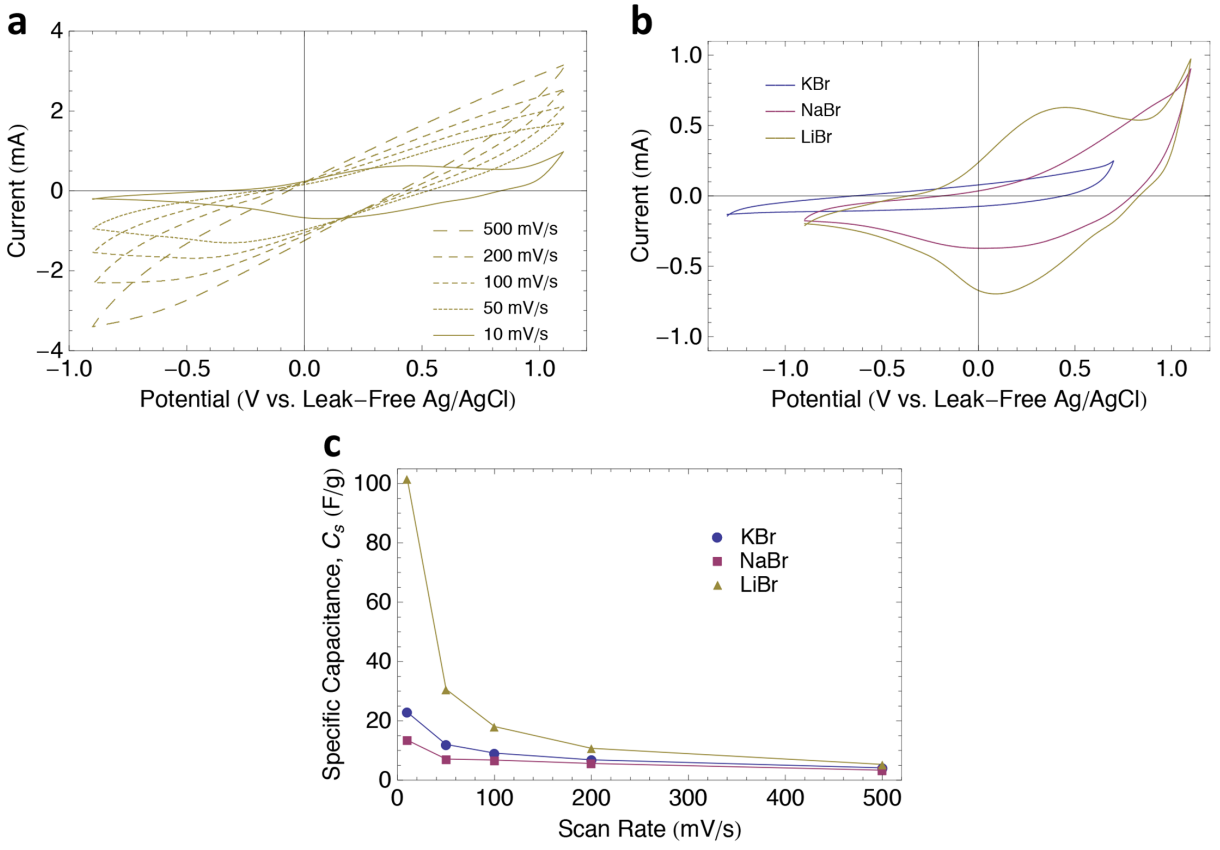

Figure 3.3: The capacitance was investigated for various nonaqueous alkali metal bromides in DMSO: a) CV curves at various scan rates for 0.3 M LiBr in DMSO, b) CV curves at 10 mV s^{-1} for various alkali metal bromide solutions with 0.3 M concentration in DMSO and c) the capacitance of all nonaqueous half-cells for various 0.3 M electrolytes in DMSO over a range of scan rates.

the constant phase element, CPE_b, replaced the capacitive element, C_b. The impedance of the circuit is calculated by

$$Z = Z' + jZ'' = R_s + \frac{1}{A(j\omega)^a + \frac{1}{R_a + \frac{R_b}{1+BR_b(j\omega)^b} + \frac{1}{W\sqrt{j\omega}}}} \tag{3.4}$$

where the term $1/[B(j\omega)^b]$ is the impedance of the constant phase element, CPE_b, where $0 < b < 1$. This change represents a non-ideal capacitive behavior associated with the pseudocapacitive mechanism as compared to the aqueous half-cells. The remaining variables are equivalent to those in Eq. 3.3. The parameters for the fitted model are reported in Table 3.2.

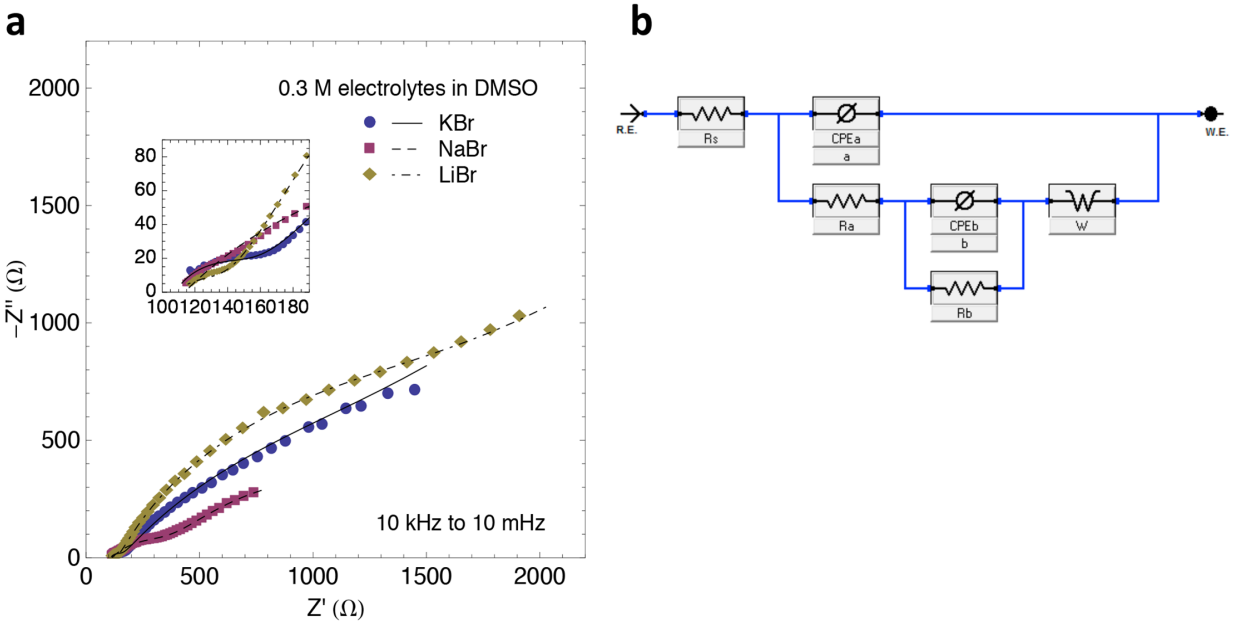

Figure 3.4: EIS data for a) 0.3 M nonaqueous electrolytes in DMSO as well as the b) equivalent circuit model used to fit the data. The markers represent the real data and the corresponding lines represent the fitted model with parameters reported in Table 3.2. The inset graphs depict the high frequency region of the EIS data and fitted model.

Table 3.2: Fitting Parameters for EIS Modeling of Nonaqueous Systems with Various Electrolytes

Electrolyte in DMSO	R_s (Ω)	A ($S \cdot s^a$)	a	R_a (Ω)	B ($S \cdot s^b$)	b	R_b (Ω)	W ($S \cdot s^{0.5}$)	Goodness of Fit
0.3 M KBr	108.0	7.22×10^{-5}	0.6567	54.3	2.42×10^{-3}	0.5574	1.117×10^{3}	5.36×10^{-3}	1.07×10^{-2}
0.3 M NaBr	113.6	8.83×10^{-4}	0.4910	331.9	6.85×10^{-3}	0.5564	1.338×10^{3}	1.97×10^{0}	8.08×10^{-4}
0.3 M LiBr	107.6	6.73×10^{-4}	0.4215	43.3	8.55×10^{-4}	0.8596	2.443×10^{3}	2.87×10^{-3}	5.75×10^{-4}

The interfacial charge transfer resistance, R_a, may help to explain the trend in the capacitive behavior of the vanadium oxide exposed to the various nonaqueous electrolytes. The equivalent series interfacial charge transfer resistance increases in the following trend: LiBr > KBr > NaBr, which is oppositely correlated with the capacitance observed in Figure 3.3. Additionally, the capacitance exhibited by the LiBr system may be further enhanced by its higher solubility limit. The 0.3 M solution concentration is much closer to the solubility limit of NaBr, and especially KBr, than the solubility of LiBr [48,49]. At this concentration, LiBr may exhibit a larger degree of dissociation, which would result in a higher electrolyte conductance, acting as a supplementary contribution to the difference in the capacitive behavior between the LiBr and NaBr or KBr electrolyte solutions.

The capacitive performance and EIS behavior of the vanadium oxide exposed to nonaqueous electrolyte-DMSO solutions both indicated that LiBr was the most suitable electrolyte for further nonaqueous solution studies. Additionally, the higher solubility of LiBr in nonaqueous solvents such as DMSO and PC was utilized to maximize the bulk electrolytic conductance by using higher electrolyte concentrations in the following variable-solvent study.

3.3.3 Nonaqueous LiBr-Solvent Systems

In aqueous systems vanadium oxide undergoes material dissolution-related capacitive degradation upon cycling in half-cells [41]. Nonaqueous aprotic solvents such as DMSO and PC have the potential to reduce this type of degradation. Figure 3.5 reports the capacitive cycle behavior of vanadium oxide in LiBr half-cells using DMSO, PC and a mixture of 80% PC, 20% DMSO by volume for both 500 mV s^{-1} and 10 mV s^{-1} CV scan rates. Compared to the DMSO system, solutions containing PC exhibited significant capacitive retention for both scan rates. Furthermore, the capacitance calculated from both CV and GCD over a range of scan rates and current densities, respectively, before and after the cycling demonstrated in Figure 3.5b is reported in Figure 3.6. Notably, the pure DMSO system exhibited a higher initial capacitance

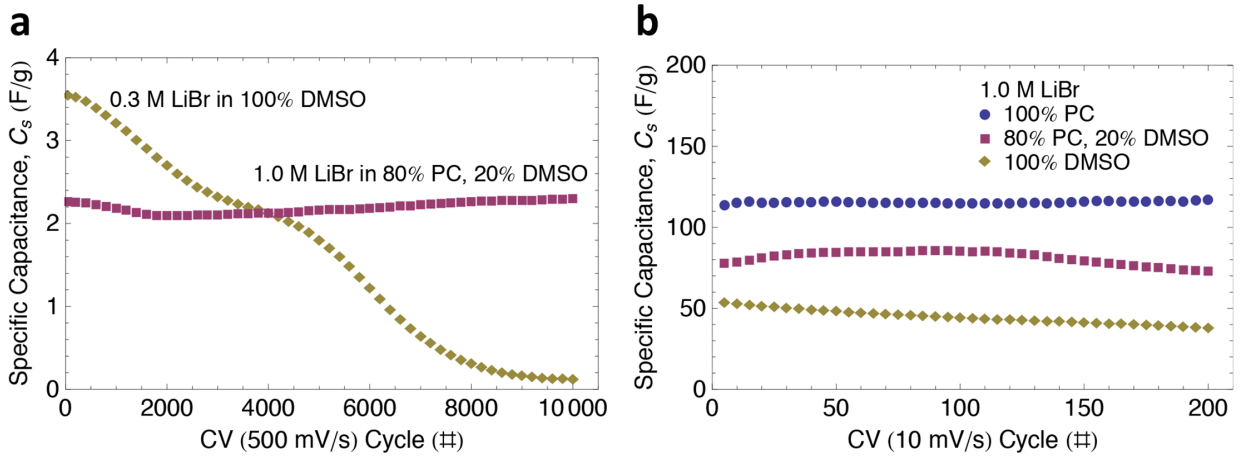

Figure 3.5: Capacitive cycle behavior of nonaqueous LiBr half-cells in various solvents calculated from CV at a) 500 mV s^{-1} and b) 10 mV s^{-1}.

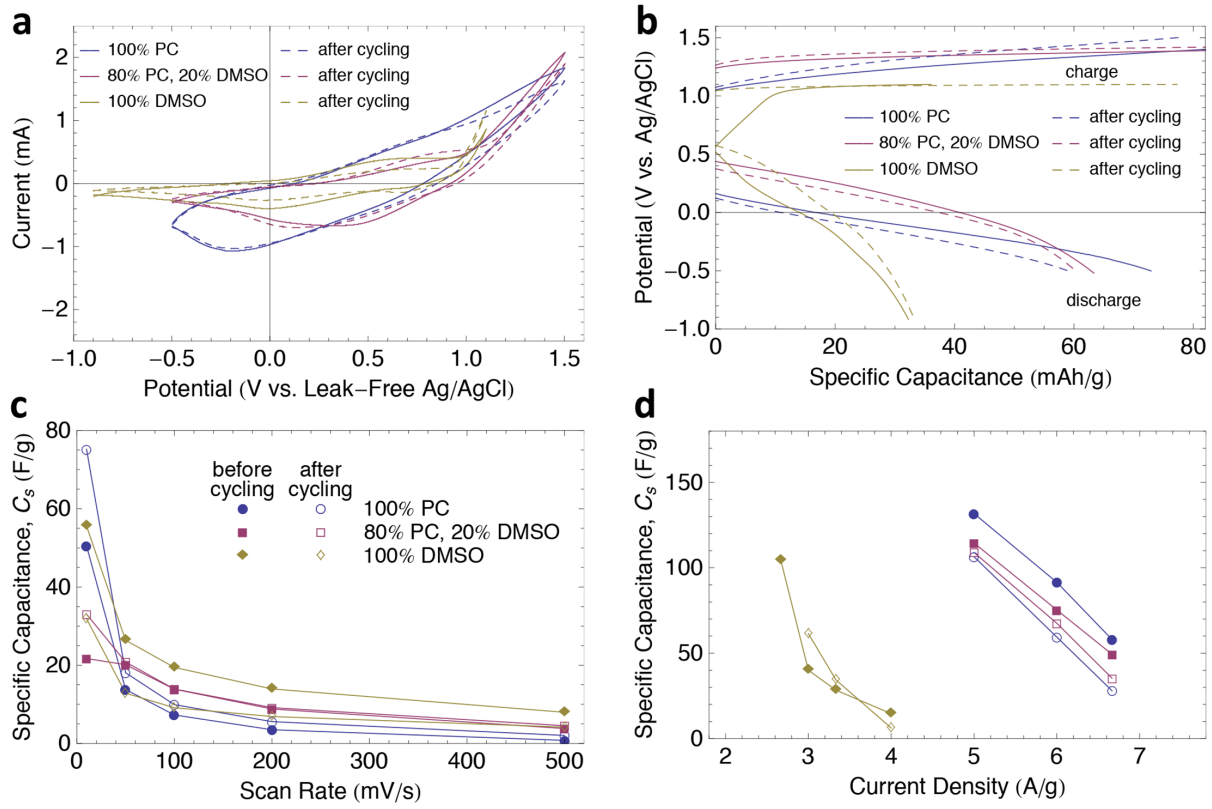

Figure 3.6: The capacitive behavior of electrodeposited vanadium oxide in contact with various nonaqueous 1.0 M LiBr-solvent systems was studied using CV and GCD: a) CV curves at 10 mV s^{-1} and b) GCD profiles at the lowest current density tested for 1.0 M LiBr systems in various solvents plotted before and after cycling as reported in Figure 3.5b; the capacitance of all nonaqueous half-cells were calculated using c) CV at various scan rates and d) GCD at various current densities for 1.0 M LiBr-solvent systems.

cycled at 500 mV s^{-1} compared to the mixed and pure PC solvents. The pure PC system exhibited a higher initial capacitance cycled at 10 mV s^{-1} and using the GCD method over a relatively slow cycle rate range. Therefore, the CV and GCD data both indicate an optimal capacitance using DMSO at high cycle rates and PC at slow cycle rates. According to the CV data, the crossover point occurs approximately between 10 and 50 mV s^{-1}.

EIS was then utilized to further study the solvent systems before and after the cycling reported in Figure 3.5b. Figure 3.7 reports the results between 10 kHz and 10 mHz in a Nyquist plot where the markers represent the experimental data and the corresponding lines plot the fitted equivalent circuit model illustrated in Figure 3.4b and whose fitting parameters are listed in Table 3.3. Although PC exhibited an ESR value 3.5 times higher and an interfacial charge transfer resistance approximately 3.1 times higher than the DMSO system, the charge transfer resistance decreased by 23% for the PC system after cycling whereas it increased by almost two orders of magnitude for the DMSO system. After cycling, both systems exhibited a small increase in the series resistance, an increase in the capacitive element, *B*, and a decrease in the resistive element,

R_b, associated with charge transfer related to the pseudocapacitive mechanism. The performance in the mixed solvent was characterized by values intermediate of the pure solvents. Overall, the EIS data along with the CV and GCD data all support the conclusion that the LiBr-DMSO system optimizes the vanadium oxide capacitance in the high frequency or scan rate range whereas the LiBr-PC system is optimal for low frequency or scan rate applications.

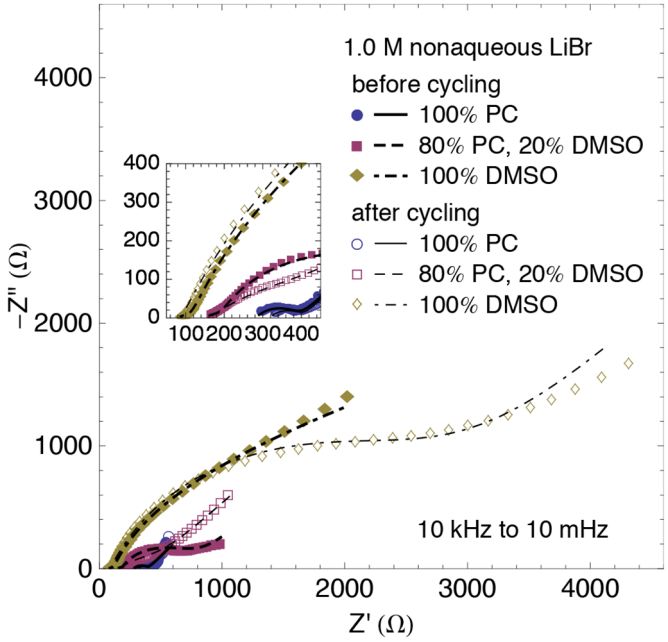

Figure 3.7: EIS data for 1.0 M nonaqueous LiBr in various solvents. The markers represent the real data and the corresponding lines represent the fitted model (Figure 4.4b) with parameters reported in Table 3.3. The inset graph depicts the high frequency region of the EIS data and fitted model.

Table 3.3: Fitting Parameters for EIS Modeling of Nonaqueous Systems with Various Solvents

1.0 M LiBr Solvent System	R_s (Ω)	A ($S \cdot s^a$)	a	R_a (Ω)	B ($S \cdot s^b$)	b	R_b (Ω)	W ($S \cdot s^{0.5}$)	Goodness of Fit
PC	280.8	2.64×10^{-4}	0.4894	118.5	1.43×10^{-1}	0.2631	1.283×10^{1}	1.75×10^{-2}	4.26×10^{-3}
PC, cycled	317.0	2.85×10^{-4}	0.4862	90.8	1.16×10^{1}	0.8880	2.180×10^{-2}	1.43×10^{-2}	3.41×10^{-3}
80%PC, 20%DMSO	149.8	6.06×10^{-4}	0.3904	65.7	2.34×10^{-4}	0.7480	6.987×10^{2}	1.52×10^{-2}	7.23×10^{-4}
80%PC, 20%DMSO cycled	160.4	1.04×10^{-3}	0.3982	564.7	3.63×10^{1}	0.9086	4.366×10^{-4}	3.10×10^{-3}	1.24×10^{-3}
DMSO	79.6	9.75×10^{-4}	0.3957	38.1	7.02×10^{-4}	0.9644	1.087×10^{4}	3.30×10^{-3}	1.92×10^{-4}
DMSO, cycled	88.9	1.53×10^{-4}	0.7110	2812.0	3.80×10^{1}	0.8716	3.843×10^{-7}	1.69×10^{-3}	1.12×10^{-3}

The morphology of the vanadium oxide electrodes was studied for samples with and without cycling at 10 mV s^{-1} for 200 cycles in half-cells containing 1.0 M nonaqueous LiBr electrolyte in pure PC, a mixture of 80% PC, 20% DMSO by volume and pure DMSO. Figure 3.8 shows the SEM images. Little variation was observed between the morphologies of the oxides exposed to the various solvents. However, the sample exposed to DMSO exhibited more charging during imaging despite carbon-coating during sample preparation to enhance surface conductivity. EIS results showed that with cycling and more exposure to DMSO, the charge transfer resistance increased significantly in DMSO. It is possible that during the long exposure to DMSO during the drying portion of the sample preparation, the solvent caused an increase in the contact resistance between the vanadium oxide and the Pt current collector by compromising the material at the interface. Additionally, the nodular morphology seems to be somewhat finer, with a smaller average nodular diameter. This may have been caused by material dissolution during cycling. A finer surface morphology along with a larger porosity may explain the significant improvement in the diffusion-related pseudocapacitive elements, B and R_b, discussed in section 3.2.1. Although these elements improved, a slight degradation was exhibited in the cycle behavior in Figure 3.5b. Material dissolution could help to explain this behavior as well due to the loss of active material mass and thus an overall reduction in intercalation sites. The

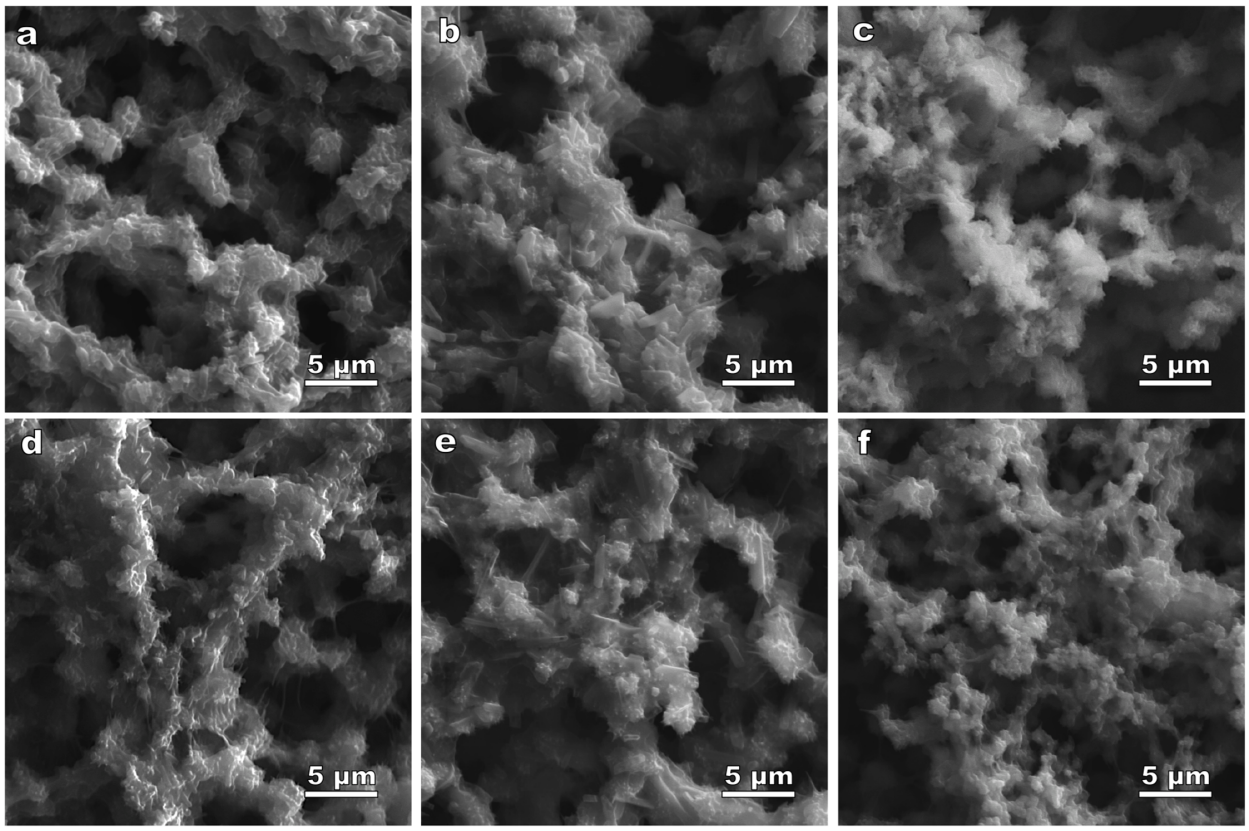

Figure 3.8: SEM images of vanadium oxide films as-prepared in a) 100% PC, b) 80% PC, 20% DMSO and c) 100% DMSO as well as films cycled at 10 mV s^{-1} for 200 cycles in d) 100% PC, e) 80% PC, 20% DMSO and f) 100% DMSO in 1.0 M nonaqueous LiBr half-cells.

morphologies of the vanadium oxide electrodes exposed to the solvents containing PC seem relatively unchanged after cycling, which is consistent with the almost constant capacitive cycle behavior.

In addition to the morphological characterization using SEM, qualitative composition analysis was conducted using EDS for an as-deposited sample not exposed to nonaqueous solvents, along with the samples with and without cycling at 10 mV s^{-1} for 200 cycles in half-cells containing 1.0 M nonaqueous LiBr electrolyte in pure PC, a mixture of 80% PC, 20% DMSO by volume and pure DMSO. Results for the as-deposited and nonaqueous solvent-exposed samples that did not undergo cycling are reported in Figure 3.9a, and the samples that underwent cycling are reported in Figure 3.9b. All samples contained C due to carbon-coating that was necessary to prevent surface charging due to the low-conductivity of vanadium oxide. Also, all samples contained Na and S, most likely due to remnants from the deposition electrolyte. As expected, the sample exposed to DMSO exhibited the highest signal intensity for sulfur. Also, all samples exposed to the LiBr-solvent systems indicated the presence of Br. With cycling, the signal intensity for Br increased for the solvent systems containing PC. Without quantitative data corresponding to the concentration of Br and Li on the surface, it is impossible to distinguish with certainty between excess electrolyte left on the surface from the drying process or possible intercalated species in the oxide itself.

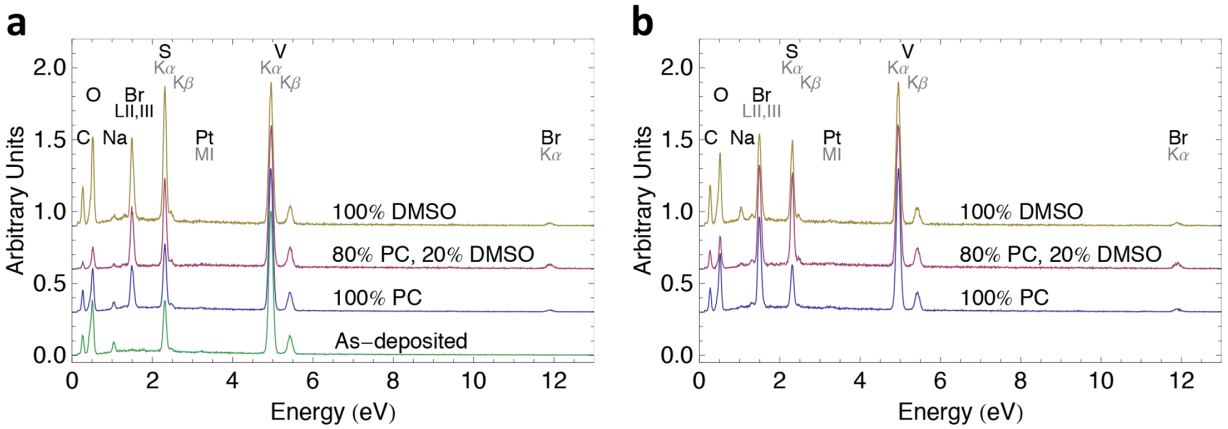

Figure 3.9: EDS of vanadium oxide films a) with no cycling and b) cycled at 10 mV s^{-1} for 200 cycles in 1.0 M nonaqueous LiBr half-cells with various solvents.

3.4 Conclusion

According to the capacitive performance and impedance data collected for aqueous half-cell systems, vanadium oxide exposed to solutions containing NaCl was identified as a suitable electrolyte for aqueous electrochemical capacitor applications. In nonaqueous DMSO LiBr was chosen over NaBr or KBr electrolytes due to both lower ESR and higher capacitive performance. A comparison of DMSO and PC nonaqueous solvents showed that the vanadium oxide electrode

exposed to the LiBr-PC system performed with a higher capacitance at slower cycle rates whereas the system containing DMSO as the solvent obtained a higher capacitance at the relatively faster cycle rates. The improved performance of the LiBr-DMSO system at high scan rates may be attributed to higher ionic conductivity. However, the durability of the vanadium oxide half-cells in the DMSO system may prove to be problematic as demonstrated by the significant increase in charge transfer resistance upon electrochemical cycling.

Chapter 4 – Cycling Behavior of Aqueous and Nonaqueous Vanadium Oxide Electrochemical Capacitors

This material has been submitted for publication:

A. M. Engstrom, F. M. Doyle, submitted to J. Power Sources (2013).

Abstract

The initial capacitance, electrochemical impedance and cycle behavior of symmetric vanadium oxide whole-cells were studied for aqueous and nonaqueous electrolyte-solution systems. An aqueous system utilizing a 3.0 M NaCl electrolyte at pH 3.0 exhibited an excellent 96% capacitance retention over 3000 cycles at 10 mV s^{-1}. An equivalent system tested at 500 mV s^{-1} displayed an increase in capacitance over the first several thousands of cycles, and eventually stabilized over 50,000 cycles. Electrodes cycled in nonaqueous 1.0 M LiBr in PC exhibited mostly non-capacitive charge-storage, most likely responsible for the observed morphological change, over the first 1000 cycles at 10 mV s^{-1}, and capacitive charge-storage dominated the last thousand cycles. Electrodes cycled in LiBr-DMSO exhibited a gradual capacitive decay over 10,000 cycles at 500 mV s^{-1}. Morphological and compositional analyses, as well as electrochemical impedance modeling, provide additional insight into the cause of the cycle behavior.

4.1 Introduction

Electrochemical capacitors (ECs) are an important class of energy storage device because they provide higher energy density than traditional electrostatic capacitors and higher power density than battery systems [1,10]. They are further distinguished by the two primary charge storage mechanisms that dominate these devices. The first, the electrochemical double layer capacitor, stores charge electrostatically across the double layer that forms at the electrode/electrolyte interface and ideally no Faradaic charge transfer occurs across the interface, which is unlike the second type of device, the pseudocapacitor. A pseudocapacitive EC primarily stores charge indirectly by highly reversible redox reactions at the surface and in the bulk of the material, i.e. the transition between the various oxidation states in transition metal oxides accompanied by the intercalation and deintercalation of electrolyte ions. The study of transition metal oxides for utilization in electrochemical capacitors began with the discovery of the capacitive properties of hydrated ruthenium oxide [5]. The capacitance of $RuO_2 \cdot nH_2O$ has reached as high as 900 F g^{-1}

[15]; however, this material is prohibitively expensive for commercial applications and thus other transition metal oxides have been explored [11,12,16]. In 1999, Lee and Goodenough were the first to describe vanadium oxide as a more cost-effective material for electrochemical capacitors [6]. Vanadium oxide is a desirable active material due to its wide range of stable oxidation states (V, IV, III and II) and its relatively higher abundance, low cost and toxicity compared to RuO_2 [6,17,58]. This material exhibits excellent specific capacitance ranging from 90 to 870 F g^{-1} depending upon the structure, composition and accessible surface morphology as determined by the synthesis and processing methods as well as the testing environment [6,17-23].

ECs are regarded for their high specific power and energy density, low material cost and toxicity as well as a long cycle life owing to high reversibility [1,10-13]. The specific energy and maximum specific power density, E_s and P_s, (reproduced for convenience, equivalent to Eq. 3.1 and 3.2) respectively, are calculated [1,10,11,13] by:

$$E_s = \frac{1}{2} C_s V^2 \tag{4.1}$$

$$P_s = \frac{V^2}{4\, ESR\, m} \tag{4.2}$$

where C_s is the specific capacitance calculated from cyclic voltammetry (CV) or galvanostatic charge/discharge (GCD) experiments calculated from [41]. V is the operating voltage, ESR is the equivalent series resistance and m is the mass of the electrode material. Some of the most critical factors affecting EC performance include the active material morphology and composition, the electrolyte solution properties such as concentration and conductivity, as well as the separator porosity and conductivity [1,11]. The separator in a two-electrode whole-cell device is essential to prevent direct electrical contact between the electrodes, which would short-circuit the device. However, its porosity and ionic conductivity must be optimized in order to minimize the ESR and thus maximize the power density, as calculated from Eq. 4.2. The most common practice is to choose separators that have pore sizes much larger than the size of the solvated ions to ensure a high ionic conductivity, such as with commercially available separators or filter paper [11]. However, it was previously found that vanadium oxide dissolves slightly during cycling in aqueous solutions [41]. Consequently, a separator that will conduct protons or small alkali metal cations, but prevent conduction of the larger dissolved vanadium cations, could improve the cycle performance of the cell by keeping the dissolved species close to the electrode from which they originated, allowing redeposition during the following half-cycle. This will simultaneously prevent an accumulation of material on one electrode of a whole-cell.

Electrolyte-solvent systems were previously studied for both aqueous and nonaqueous solutions. In this study, NaCl was identified as a suitable aqueous electrolyte, and LiBr-PC and LiBr-DMSO were identified as suitable nonaqueous systems for relatively slow and fast cycle-rate applications, respectively (see Chapter 3). In the current study, the previously identified aqueous and nonaqueous electrolyte-solution systems are further studied in symmetric two-electrode systems to study their cycle behavior and assess their power and energy density characteristics. Although the limited potential difference that can be applied across a symmetric two-electrode system would preclude the use of this for commercial energy storage applications, a symmetric

system allows more unambiguous examination of a full-cell system, which assists a fundamental examination of the impact of various experimental parameters.

The first part of the study compares the capacitive and impedance behavior of aqueous electrochemical capacitors with various separator materials and designs. The subsequent studies utilize morphological analyses and electrochemical impedance modeling to elucidate the observed cycle behavior of the aqueous and nonaqueous systems cycled in various cycle-rate regimes.

4.2 Experimental Methods

4.2.1 Electrochemical Synthesis

Vanadium oxide films were synthesized using a three-electrode cell comprising a saturated KCl Ag/AgCl reference electrode (0.199 V vs. SHE) from Koslow Scientific, a 5 x 5 cm Pt gauze from Sigma Aldrich as the counter electrode and a modified 0.5 cm diameter planar Pt electrode for the working electrode and substrate for the vanadium oxide. In order to characterize the vanadium materials, the working electrode was modified to facilitate removal for *ex situ* examination without disrupting the deposited films [41]; a 7.0 mm square Pt foil was placed over a 0.5 cm diameter planar Pt electrode, which provided electrical connection. A mask made by punching a 0.5 cm diameter hole in a Parafilm® M sheet was placed over the foil to secure it to the Pt electrode while exposing the same 0.5 cm diameter surface area. The films were deposited at 1.4 V vs. Ag/AgCl in 1.0 M $VOSO_4$, 0.1 M Na_2SO_4, pH 1.8 aqueous solution prepared using 18 MΩ Millipore water. A total of 3.0 C of charge was passed. The pH of 1.8 corresponds to the solubility minimum for V_2O_5 under oxidizing conditions [28,36]. The potentiostatic deposition potential was chosen at the center of the broad electrodeposition peak on an anodic 2 mV s^{-1} linear voltammetric sweep from the open circuit potential until the initiation of oxygen evolution. Following deposition, the films were rinsed in water, 18 MΩ Millipore, and dried under N_2 flow at 25 °C for approximately 5 min. The vanadium oxide films weighed 0.3 ± 0.1 mg (measured for several samples).

4.2.2 Electrolyte Solution Preparation

The vanadium oxide electrodes were studied in both aqueous and nonaqueous electrolyte-solvent systems.

Aqueous electrolyte solutions were prepared with 18 MΩ Millipore water. According to previous results, the optimal pH region for the vanadium oxide system was found to be pH 3.0 (see Chapter 2) and a later study identified the preferred electrolyte solution as 3.0 M NaCl (see Chapter 3). Consequently, all aqueous solutions contained 3.0 M NaCl adjusted to pH 3.0 using HCl. The electrolyte pH was measured with an Orion, Thermo Scientific 915600 pH electrode connected to an Orion 290A pH meter calibrated with pH 7.0, 4.0 and 1.0 buffer solutions prior to each measurement.

Agar gel electrolytes were prepared according to a previously reported technique [41]. The gels were prepared by dissolving 13.34 g L^{-1} agar powder in boiling 3.0 M NaCl, pH 3.0 electrolyte. The solution was allowed to cool to 50 °C under forced convection for approximately 30 min, by which time visual inspection indicated that gelation had commenced, with concurrent increase in viscosity. The desired volume was drop-deposited on the dry vanadium oxide film followed by its complete gelation before further cell assembly.

Electrolyte solutions in nonaqueous solvents were prepared in a dry glove box under a nitrogen environment. Propylene carbonate (PC) was stored over 5Å molecular sieves and dimethyl sulfoxide (DMSO) was stored over 4Å molecular sieves to remove any contaminant water content. All solvents and molecular sieves were purchased from Alfa Aesar. Each batch of molecular sieves was checked for activity prior to use by measuring a temperature change of at least 4 °C when a small amount of water was dropped over a test sample of the molecular sieves. Electrolytes were weighed in air outside the dry box in sample containers that had been cleaned in 18 MΩ Millipore water and dried at approximately 90 °C. The containers containing the electrolytes were immediately transferred to the dry box where the samples underwent several evacuation and backfill steps to exchange the atmosphere with dry nitrogen. In the dry box the solvents were decanted from their storage containers to prepare the individual electrolyte solutions.

4.2.3 Whole-Cell Design

All whole-cells utilized symmetric electrodeposited vanadium oxide as-deposited on the 7.0 mm square Pt foils for both electrodes. Different electrolytes and separator materials were examined. The separator materials tested were Millipore filter paper with a 0.45 μm pore size as well as Nafion® membranes with a thickness of 0.050 mm or 0.125 mm. Different electrolyte volumes and separator distances between the electrodes were also tested using annular spacers with a thickness of 1.0 mm cut from a 0.25 in. ID, 0.375 in. OD Teflon® tube. All cells utilized for the separator optimization contained 13.34 g L^{-1} agar gel electrolyte prepared with aqueous 3.0 M NaCl at pH 3.0. The gelled electrolyte provided a convenient means of preventing leakage from the spacer to maintain a controlled electrolyte volume between the electrodes. Earlier work had established that gellation with agar had little impact on the resistance of KCl solutions [41]. Subsequent whole-cells contained a 0.050 mm Nafion® membrane, and the electrolyte-solvent system was varied. All aqueous whole-cells were assembled in air, and the nonaqueous whole-cells were assembled in the dry box under a nitrogen environment. Pt foils contacting the back of the as-deposited electrodes acted as the current collectors, and Parafilm® M was utilized to compress and seal all whole-cells to prevent evaporation and water contamination for the nonaqueous cells.

4.2.4 Electrochemical Characterization

The oxides were electrochemically characterized using cyclic voltammetry (CV) and galvanostatic charge/discharge (GCD) cycles. The aqueous systems were characterized between -0.5 and 0.5 V, and the nonaqueous systems were tested between -1.0 and 1.0 V. The potentiostatic electrochemical deposition, CV and GCD measurements were performed using a PAR 273 potentiostat.

Electrochemical Impedance Spectroscopy (EIS) was performed using a Gamry Series G™ potentiostat and modeled using Echem Analyst™ Software. The impedance of the vanadium oxide films in the various electrolyte-solution systems were measured using an AC voltage amplitude of 10 mV with respect to the open circuit potential over a frequency range of 100 kHz to 10 mHz unless otherwise noted.

4.2.5 Morphological and Compositional Characterization

After deposition and cycling any remaining Parafilm® M was removed, leaving only the vanadium oxide on the Pt foil substrate. Samples containing a gel coating were exposed to the testing electrolyte at an elevated temperature, approximately 100 °C, to dissolve and remove the agar. All electrodes were then dried under N_2 flow at 25 °C and stored under Ar until further analysis. The morphological and qualitative compositional analyses were performed with a Leo 430 SEM equipped with EDS.

4.3 Results and Discussion

4.3.1 Separator Optimization

Various separator materials and designs were investigated for a symmetric vanadium oxide whole-cell containing 13.34 g L^{-1} agar gel electrolyte prepared with 3.0 M aqueous NaCl at pH 3.0. The specific capacitance values calculated from both CV and GCD methods are reported in Figure 4.1, and the EIS results measured between 100 kHz and 10 mHz are reported in Figure 4.2. The markers represent the experimental data, and the corresponding lines plot the fitted equivalent circuit model shown in Figure 4.2b. The model impedance is calculated by:

$$Z = Z' + jZ'' = R_s + \frac{1}{A(j\omega)^a + \frac{1}{R_a + \frac{R_b}{1+BR_b(j\omega)^b} + \frac{1}{W\sqrt{j\omega}}}} \tag{4.3}$$

where *Z'* and *Z''* are the real (resistive) and imaginary (capacitive) components of *Z*, the total impedance. R_s is the equivalent series resistance or ESR, ω is the frequency in Hz and j is $\sqrt{-1}$. The terms $1/[A(j\omega)^a]$ and $1/[B(j\omega)^b]$ represent the impedance of the constant phase elements, CPE_a and CPE_b, related to the double layer capacitance and the capacitive behavior associated with the pseudocapacitive mechanisms, respectivlty, where $0 < a < 1$ and $0 < b < 1$. Values of a or b less than 1 indicate deviation from ideal capacitive behavior. R_a is the interfacial charge transfer resistance, R_b is the resistance associated with the pseudocapacitive mechanisms, and $1/[W\sqrt{j\omega}]$ is the diffusional Warburg impedance associated with the porous electrode [10,40].

The parameters used in the fitted model in Figure 4.2a are reported in Table 4.1. The R_s or ESR values agree with the data shown in the inset graph in Figure 4.2a, which shows the high frequency domain of the impedance response. The R_s value is defined as the point at which the imaginary component, *Z''*, goes to zero [1].

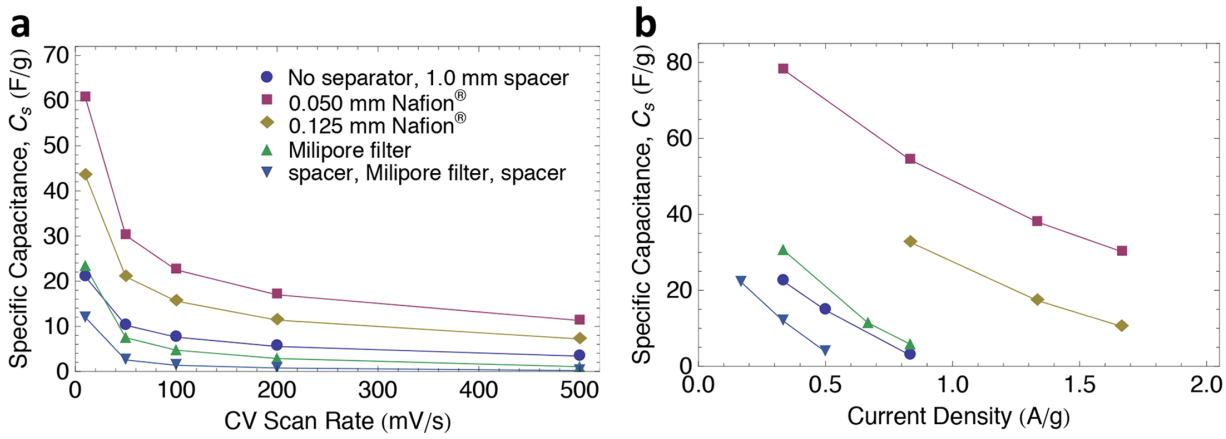

Figure 4.1: Capacitance of symmetric aqueous whole-cells with various separator designs calculated from a) CV and b) GCD composed of 13.34 g L^{-1} agar gel electrolyte prepared with 3.0 M NaCl at pH 3.0.

The designs consisted of three types of separator materials and in some tests utilization of annular spacers with a 1.0 mm thickness. One potential benefit in utilizing the spacers would be to increase the electrolyte volume in the cell. In order to prevent depletion of the electrolyte during cycling, the electrolyte concentration and volume must be sufficient compared to the available intercalation sites in the electrodes [10]. The gel-supported electrolyte was utilized to prevent electrolyte leakage from the spacer volume. Comparing the cell containing only a Milipore separator with the cell containing a spacer on either side of the Milipore separator shows a decrease in capacitive performance and a significant increase in the ESR, most likely due to the IR drop associated with a larger distance between the electrodes. Comparing the types of separators, the Milipore filter paper has a large pore size, 0.45 µm, but was thicker than the two types of proton-conducting Nafion® membranes. Of the three membranes, the thinnest Nafion® membrane, 0.050 mm, exhibited the lowest ESR and charge transfer resistance as well as the best capacitive performance. The final design consisted of a single spacer that was placed between the electrodes without any type of separator. Although the ESR and charge transfer resistance were minimized for this design, its capacitive response was inferior to the Nafion® membrane cells, most likely due to the increased distance between the electrodes. The advantage of improved ionic transport due to the lack of a separator could also lead to a key disadvantage with the no-separator design. Especially during cycling in aqueous electrolytes where degradation involves dissolution of the vanadium oxide electrodes, the lack of limitation on the ionic transport could potentially lead to capacitive degradation in a whole-cell due to unequal material accumulation. All things considered, the 0.050 mm Nafion® membrane was utilized for all remaining whole-cell studies.

4.3.2 Initial Capacitance

The following study compares the initial capacitive response of the optimized aqueous and nonaqueous symmetric vanadium oxide whole-cell systems. Figure 4.3 reports the capacitance calculated from both CV and galvanonstatic CD methods for systems containing 3.0 M aqueous

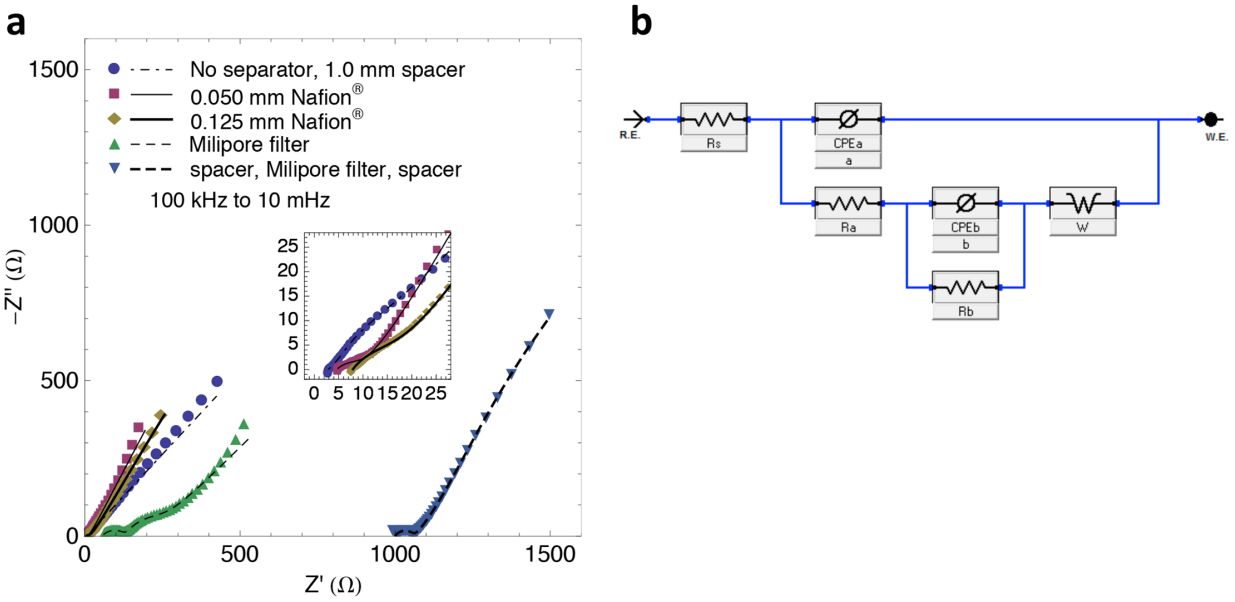

Figure 4.2: EIS data for a) symmetric aqueous systems with various separator designs composed of 13.34 g L^{-1} agar gel electrolyte prepared with 3.0 M NaCl at pH 3.0 b) equivalent circuit model used to fit the data. The markers represent the real data and the corresponding lines represent the fitted model with parameters reported in Table 4.1. The inset graph depicts the high frequency region of the EIS data and fitted model.

Table 4.1: Fitting Parameters for EIS Modeling of Aqueous Systems with Various Separator Designs

Separator	R_s (Ω)	A ($S \cdot s^a$)	a	R_a (Ω)	B ($S \cdot s^b$)	b	R_b (Ω)	W ($S \cdot s^{0.5}$)	Goodness of Fit
1.0 mm Spacer	2.95	1.91×10^{-3}	0.6347	3.55	5.950×10^{-4}	0.9995	1.029×10^{1}	5.250×10^{-3}	3.65×10^{-3}
0.050 mm Nafion®	4.65	3.224×10^{-3}	0.5004	6.52	2.582×10^{-2}	0.8567	5.368×10^{6}	2.570×10^{-2}	1.10×10^{-3}
0.125 mm Nafion®	7.89	2.925×10^{-3}	0.6077	13.97	2.218×10^{-2}	0.7935	6.099×10^{3}	1.744×10^{-2}	9.69×10^{-4}
Milipore filter	55.42	5.443×10^{-5}	0.5496	78.21	2.236×10^{-3}	0.7575	8.676×10^{1}	8.651×10^{-3}	1.55×10^{-4}
Spacer, Milipore, Spacer	999.70	5.180×10^{-5}	0.6289	61.96	2.770×10^{-2}	0.9255	2.005×10^{3}	9.497×10^{-3}	2.59×10^{-6}

NaCl at pH 3.0 with and without an agar gel-supported matrix, as well as systems containing nonaqueous 1.0 M LiBr in PC and DMSO. The similarity between the aqueous systems with and without the gel structure is consistent with previous results for thin gel electrolyte coating volumes. Only very large volumes of gelled electrolyte affect ionic transport [41]. As expected,

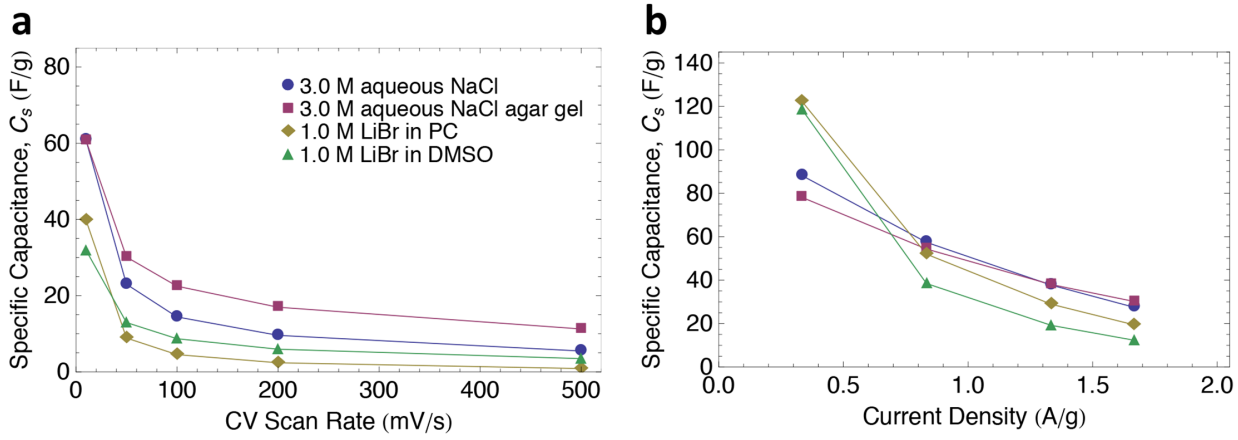

Figure 4.3: Initial capacitance of symmetric aqueous and nonaqueous whole-cells containing a 0.050 mm Nafion® membrane separator calculated from a) CV and b) GCD. The aqueous and nonaqueous whole-cells were cycled in a 1.0 and 2.0 V window, respectively.

except for very low current densities, the higher-conductivity aqueous systems exhibit a higher capacitance than the nonaqueous systems. However, the nonaqueous systems are cycled in a 2.0 V operating voltage window compared to the 1.0 V window of the aqueous systems. According to Eq. 4.1, the energy density is linearly related to the capacitance, but quadratically related to the operating voltage window. Therefore, a cell with a capacitance half as large but over double the voltage window, as in the case between the nonaqueous and aqueous systems at 10 mV s^{-1}, would perform with double the energy density. As for the nonaqueous systems, the cycle rate-related optimization is consistent with the half-cell studies; the DMSO system performs better at high scan rates, and the PC system performs best at slower scan rates (see Section 3.3.3). The crossover point occurs between 10 and 50 mV s^{-1}. As the scan rate and current density decreases, the capacitance exhibited by the nonaqueous systems becomes more comparable to the aqueous systems. In fact, at the lowest current density tested with the galvanonstatic CD method, both nonaqueous systems outperformed the aqueous systems. The combination of the slow cycle-rate as well as the larger potential window allows for the transition to a lower average mixed-valence oxidation state while also accounting for the higher solution resistance.

4.3.3 Cycle Behavior

The cycle behavior of the optimal aqueous and nonaqueous systems was studied using cyclic voltammetry. The capacitance calculated over several cycles is reported in Figure 4.4 for both the 10 and 500 mV s^{-1} experiments. The cyclic voltammograms for each of the five systems tested are plotted in Figure 4.5. For the 10 and 500 mV s^{-1} experiments every 40th and every 500th cycle is plotted, respectively. The shade of the voltammograms is graded from gray to black indicating the chronological progression of the scans. The optimal 3.0 M aqueous NaCl at pH 3.0 with or without a gel-supported matrix was tested at both 10 and 500 mV s^{-1}. The aqueous system exhibited an excellent 96% capacitance retention over 3000 10 mV s^{-1} cycles. With cycling, the shape of the CV became more rectangular, indicating more ideal

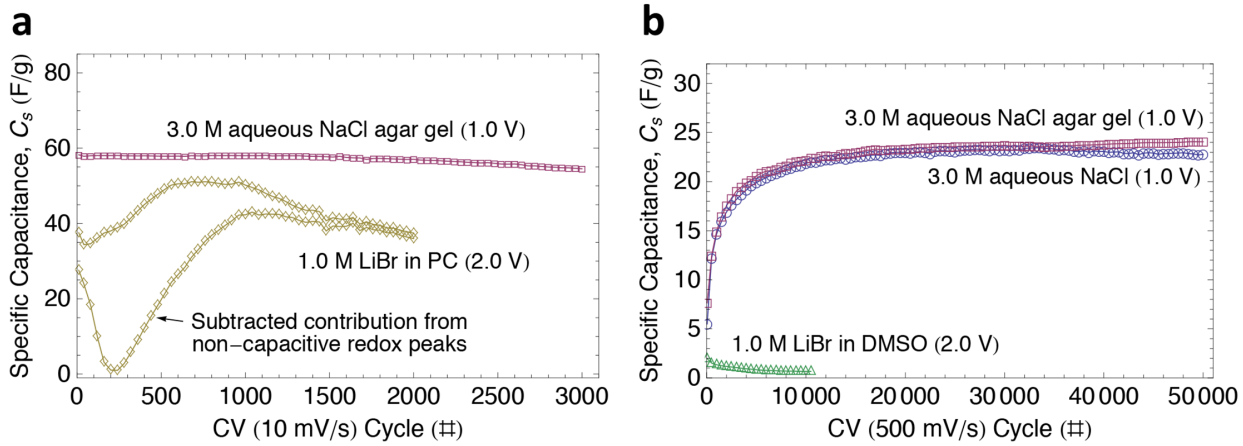

Figure 4.4: Capacitive cycle behavior of aqueous and nonaqueous whole-cells containing a 0.050 mm Nafion® membrane separator calculated from CV at a) 10 mV s^{-1} and at b) 500 mV s^{-1}.

pseudocapacitive behavior. The aqueous whole-cells with and without the agar gel matrix cycled at 500 mV s^{-1} experienced an increase in capacitance over the first several thousands of cycles, eventually stabilizing with no significant degradation after 50,000 cycles. This behavior could be explained by a morphological change or change in the electronic property of the vanadium oxide.

The 1.0 M LiBr in PC and DMSO systems were tested at 10 and 500 mV s^{-1}, respectively. The shape of the CV for the PC system (see Figure 4.5d) indicates that during cycling, distinguishable redox peaks begin to dominate and become more reversible as the capacitive contribution decreases. Eventually, the height of the redox peak decreases and the overall charge-stored becomes more capacitive. Figure 4.4a plots both the capacitance calculated from the overall charge passed as well as a curve where the charge associated with the redox peaks is subtracted to emphasize the portion that is dominated by non-capacitive charge-storage. Eventually, the capacitive charge-storage mechanism dominates, and after 2000 cycles the capacitance gradually starts to degrade. The shape of the CV associated with the 1.0 M LiBr in DMSO experiment cycled at 500 mV s^{-1} shown in Figure 4.5e also indicates the formation of a small redox peak, but overall, the capacitive behavior exhibits gradual degradation over 10,000 cycles. The specific capacitance before and after cycling for the aqueous and nonaqueous whole-cells calculated from CV and GCD methods is reported in Figure 4.6. The aqueous sample cycled at 10 mV s^{-1} displayed a slightly higher capacitance at higher scan rates and a slightly lower capacitance at the slower scan rates and lower current densities as compared to the sample before cycling. A similar effect occurred for the nonaqueous PC system where the capacitance increased for the relatively higher scan rates but decreased for the slower scan rates and low current densities. After 500 mV s^{-1} cycling, the aqueous systems show a much higher capacitance at all scan rates, but the system that did not contain the gelled matrix exhibited an even higher capacitance at especially slow scan rates and low current densities. For the nonaqueous DMSO system, the capacitive response decreased after cycling at 500 mV s^{-1} over the entire range of scan rates and current densities tested.

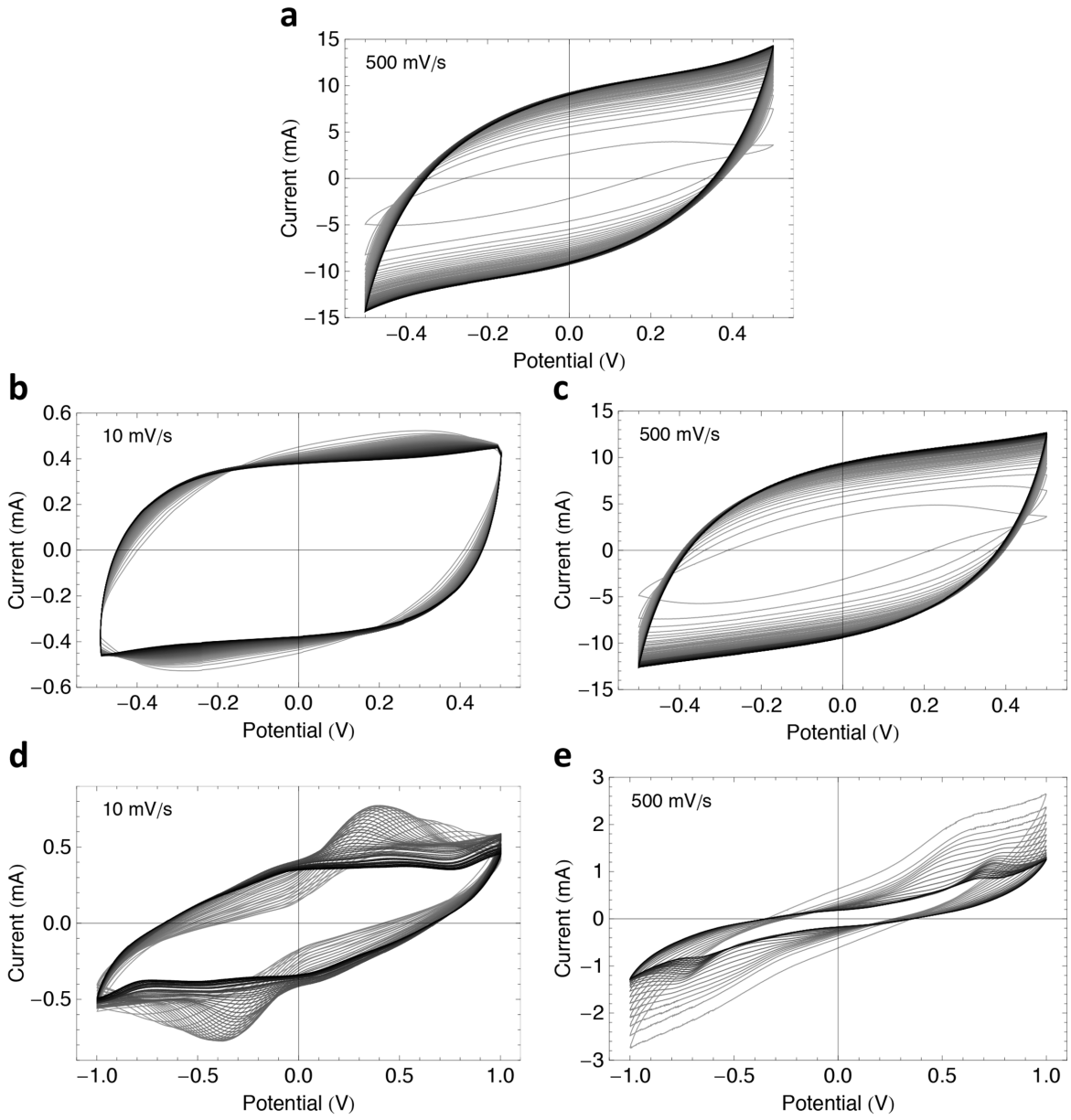

Figures 4.5: Cycle behavior of whole-cells containing a 0.050 mm Nafion® membrane separator and an aqueous electrolyte containing a) 3.0 M NaCl at pH 3.0 electrolyte cycled at 500 mV s^{-1}, b) 13.34 g L^{-1} agar electrolyte prepared with 3.0 M NaCl at pH 3.0 cycled at 10 mV s^{-1} or c) 500 mV s^{-1} as well as nonaqueous 1.0 M LiBr electrolytes in d) 100% PC cycled at 10 mV s^{-1} and e) 100% DMSO cycled at 500 mV s^{-1}. Every 40 cycles are shown for the 10 mV s^{-1} CV, and every 500 cycles are shown for the 500 mV s^{-1} CV. The color of the cycles is graded from gray to black indicating the progression from the first to the last CV cycle, respectively.

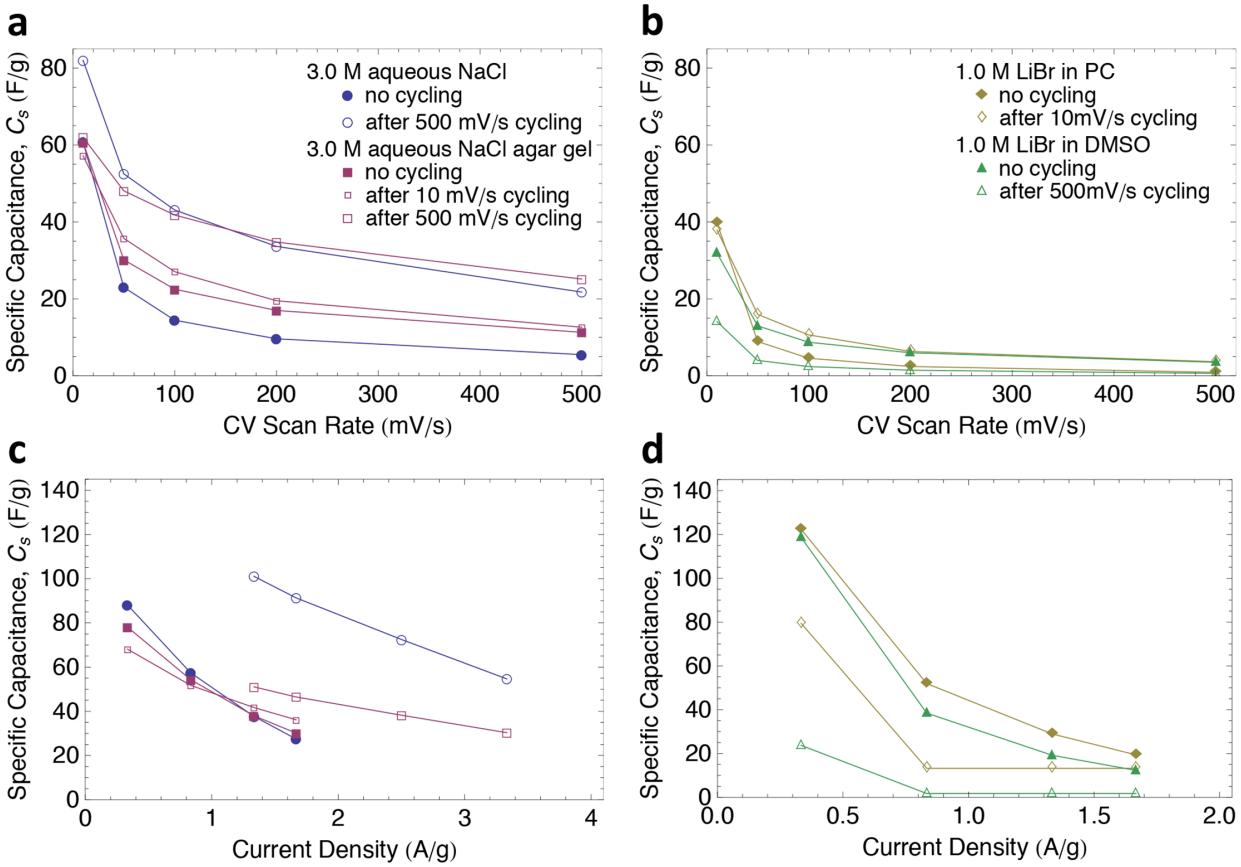

Figure 4.6: Capacitance of a, c) aqueous whole-cells and b, d) nonaqueous whole-cells before and after cycling calculated from CV and GCD, respectively. The aqueous and nonaqueous whole-cells were cycled in a 1.0 and 2.0 V window, respectively, and all whole-cells contain a 0.050 mm Nafion® membrane separator.

EIS data reported in Figure 4.7 were also utilized to study these systems. The markers represent the experimental data, and the corresponding lines plot the fitted equivalent circuit model shown in Figure 4.2b utilizing the parameters reported in Tables 4.2 and 4.3 and calculated by Eq. 4.3 for the aqueous and nonaqueous whole-cells, respectively. For both aqueous and nonaqueous systems the ESR decreased with cycling except for the aqueous system cycled in 10 mV s^{-1}, which exhibited a small increase in resistance. The PC system had the most marked improvement in the ESR by decreasing nearly 80%. For the aqueous systems and nonaqueous PC systems, the interfacial charge transfer resistance also decreased after cycling while the DMSO system experienced a significant increase. In general, the constant phase elements exhibited more ideal capacitive behavior for the cycled aqueous systems indicated by the larger values of a and b. The cycled PC system displayed an increase in B, b and a decrease in R_b indicating an increase in capacitance and decrease in resistance associated with the charge transfer involved in the pseudocapacitive mechanism. The cycled DMSO system experienced the opposite effect, which is consistent with the capacitive behavior reported in Figure 4.4.

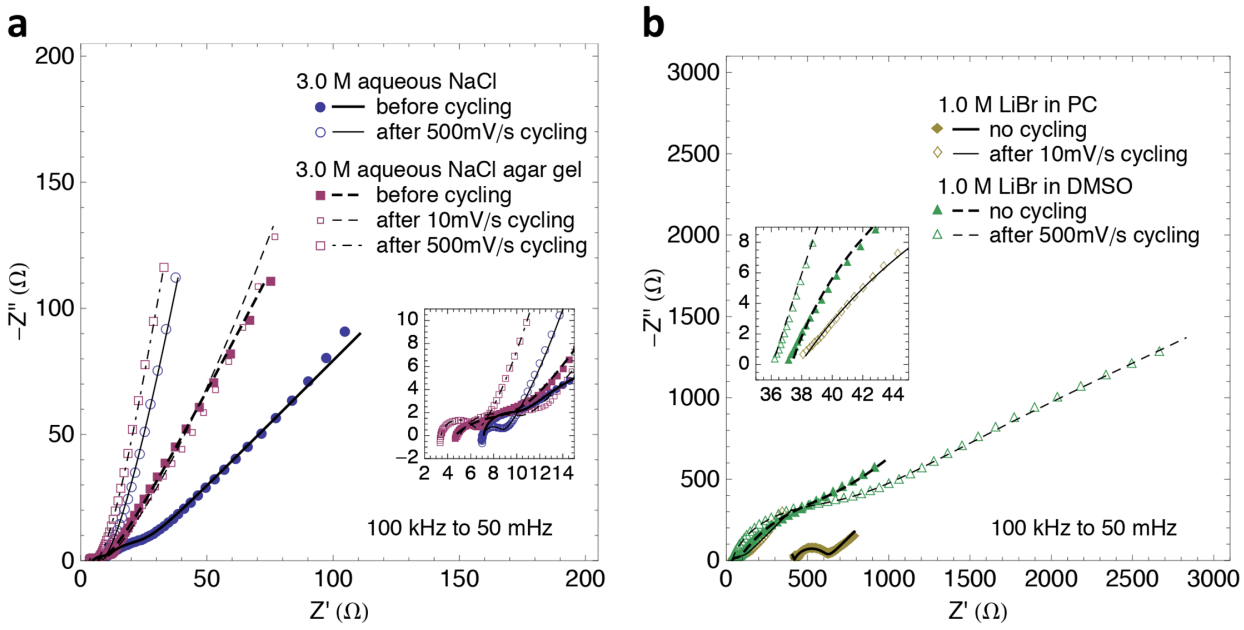

Figure 4.7: EIS of a) aqueous whole-cells and b) nonaqueous whole-cells before and after cycling. The markers represent the real data and the corresponding lines represent the fitted equivalent circuit model depicted in Figure 4.2b with parameters reported in Table 4.2 and 4.3 for the aqueous and nonaqueous systems, respectively. The inset graphs depict the high frequency region of the EIS data and fitted model. All whole-cells contain a 0.050 mm Nafion® membrane separator.

Table 4.2: Fitting Parameters for EIS Modeling of Aqueous Systems Utilizing 0.050 mm Nafion® Separator

Aqueous System	R_s (Ω)	A ($S \cdot s^a$)	a	R_a (Ω)	B ($S \cdot s^b$)	b	R_b (Ω)	W ($S \cdot s^{0.5}$)	Goodness of Fit
3.0 M NaCl, pH 3.0									
Before Cycling	7.154	1.040×10^{-5}	0.9849	3.282	1.850×10^{-3}	0.6971	1.044×10^{1}	1.40×10^{-2}	3.27×10^{-3}
Cycled 500 mV s^{-1}	7.115	7.699×10^{-5}	0.9333	1.567	3.139×10^{-2}	0.9312	8.388×10^{4}	6.33×10^{-2}	5.11×10^{-4}
3.0 M NaCl, pH 3.0 agar gel									
Before Cycling	4.651	3.224×10^{-3}	0.5004	6.515	2.582×10^{-2}	0.8567	5.368×10^{6}	2.57×10^{-2}	1.10×10^{-3}
Cycled 10 mV s^{-1}	5.057	1.898×10^{-4}	0.7364	5.290	3.702×10^{-2}	0.9183	1.213×10^{5}	2.21×10^{-2}	1.48×10^{-3}
Cycled 500 mV s^{-1}	3.451	4.035×10^{-5}	0.9408	2.905	3.070×10^{-2}	0.9528	8.453×10^{3}	6.96×10^{-2}	1.71×10^{-3}

Table 4.3: Fitting Parameters for EIS Modeling of Nonaqueous Systems Utilizing 0.050 mm Nafion® Separator

Nonaqueous System	R_s (Ω)	A (S·s^a)	a	R_a (Ω)	B (S·s^b)	b	R_b (Ω)	W (S·s$^{0.5}$)	Goodness of Fit
1.0 M LiBr in PC									
Before Cycling	180.8	2.71×10^{-9}	0.8950	237.1	6.15×10^{-5}	0.7710	1.950×10^{2}	8.02×10^{-3}	6.78×10^{-4}
Cycled 10 mV s^{-1}	37.9	2.54×10^{-4}	0.6237	51.1	5.05×10^{-4}	0.9997	1.588×10^{1}	4.36×10^{-3}	1.99×10^{-3}
1.0 M LiBr in DMSO									
Before Cycling	37.3	2.78×10^{-5}	0.8104	39.9	1.39×10^{-3}	0.7482	3.973×10^{2}	2.57×10^{-3}	3.36×10^{-4}
Cycled 500 mV s^{-1}	36.1	2.25×10^{-5}	0.8081	615.7	6.60×10^{-4}	0.4417	3.697×10^{3}	2.05×10^{-3}	3.41×10^{-4}

4.3.4 Morphological Characterization

The morphologies of the vanadium oxide electrodes tested in aqueous and nonaqueous whole-cell systems with and without cycling were characterized using SEM. The electrode morphologies from the 13.34 g L^{-1} agar gel electrolyte prepared with 3.0 M aqueous NaCl at pH 3.0 as well as the 1.0 M LiBr-PC nonaqueous system before and after cycling at 10 mV s^{-1} are reported in Figure 4.8. Before cycling, the electrode exposed to the aqueous agar gel electrolyte followed by its subsequent removal displays a three-dimensional nodular microstructure with nanostructured needle-like protrusions. For the sample that underwent cycling in the agar gel electrolyte, the morphology is indicative of a more fused-structure with more lateral interconnectivity in the oxide surface. This morphology may improve the conductivity and thus contribute to the observed decrease in charge transfer resistance. The electrode exposed to the 1.0 M LiBr-PC system also underwent a significant morphological change upon cycling. The textured nodular structure similar to that seen in the aqueous environment was converted to a more geometric, facetted morphology perhaps indicating a more crystalline structure. The non-capacitive redox current passed (see Figures 4.4a and 4.5d) during cycling was perhaps utilized in the dissolution and redeposition with each cycle creating a more thermodynamically stable microstructure. Although electrodeposited vanadium oxide is known to be poorly crystallized [26,34], the repeated, and to a small degree, irreversible intercalation and deintercalation of the Li ions may lead to a restructured $Li_xV_2O_5$ phase [59,60] or a similar but mixed-valence phase.

The electrode morphologies from the aqueous and nonaqueous systems cycled at 500 mV s^{-1} are shown in Figure 4.9. The morphologies for both of the aqueous electrolytes with and without the gelled matrix exhibit similar morphological characteristics before and after cycling. It was postulated in an earlier section that the improved capacitive response observed in Figure 4.4b could be explained by either a change in the morphology or a change in the electronic properties of the oxide itself. Considering the lack of morphological change, the conductivity of the oxide itself may explain the behavior. The electrical conductivity of V_2O_5 is dependent on electron hopping between the V^{5+} and V^{4+} impurity centers, and as the concentration of V^{4+} increases, the electronic conductivity increases [18,61]. With cycling, the pseudocapacitive mechanism

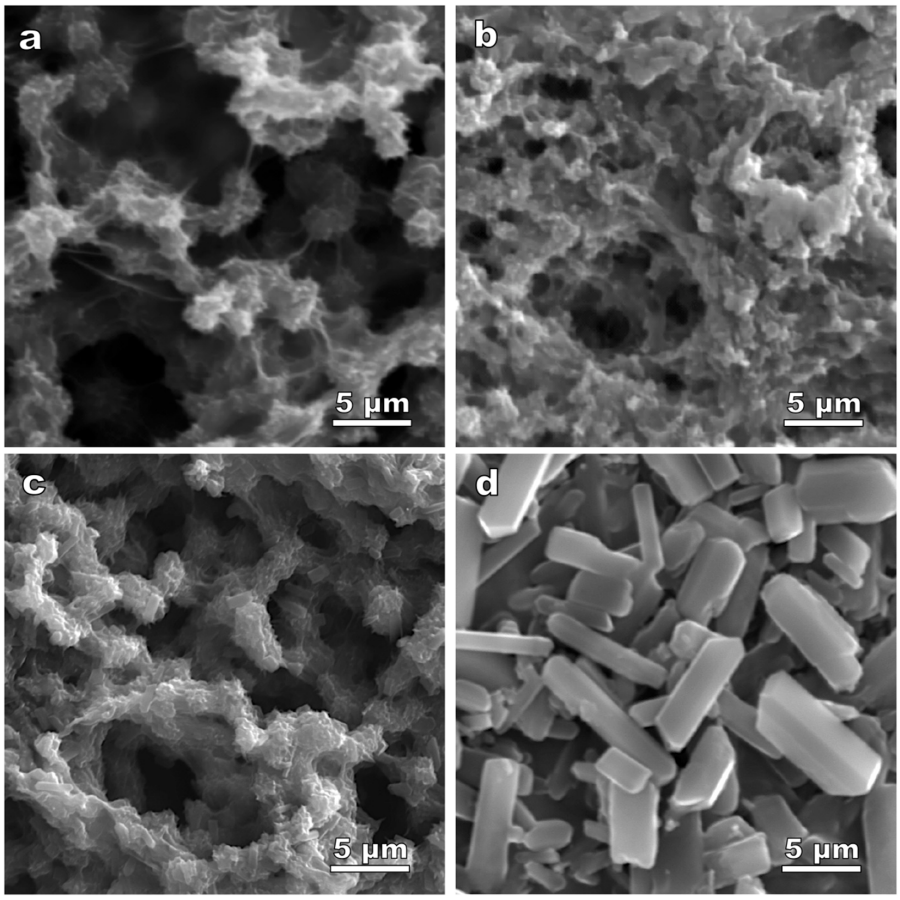

Figure 4.8: SEM images of vanadium oxide films from a) an aqueous whole cell with 13.34 g L^{-1} agar gel electrolyte prepared with 3.0 M NaCl at pH 3.0 with no cycling and b) after 10 mV s^{-1} cycling and from c) a nonaqueous whole cell with 1.0 M LiBr electrolyte in PC with no cycling and d) after 10 mV s^{-1} cycling. The agar gel was removed by brief exposure to 3.0 M NaCl at pH 3.0 and at approximately 100 °C.

involves the intercalation and deintercalation of the electrolyte ions, and some of the alkali cations remain in the material, causing the average oxidation state to decrease [41,62]. Consequently, electrical conductivity of vanadium oxide would be expected to increase during cycling. Additionally, an increase in conductivity of the electrode has been related to a decrease in interfacial charge transfer resistance [17]. The charge transfer resistance decreases by approximately a half after 500 mV s^{-1} cycling for both types of aqueous systems (see Table 4.2), and the capacitance increases by approximately a factor of 2 (see Figure 4.6a) indicating that the two properties may be related. The morphology of the electrode exposed to the 1.0 M LiBr nonaqueous DMSO system appears to have a similar morphology with perhaps a slightly larger nodular diameter. Perhaps the small redox peaks observed in Figure 4.5e were associated with the dissolution and redeposition of the oxide, resulting in a coarser microstructure. Or perhaps they were associated with the irreversible intercalation of the electrolyte ions, which would also result in a swelled microstructure.

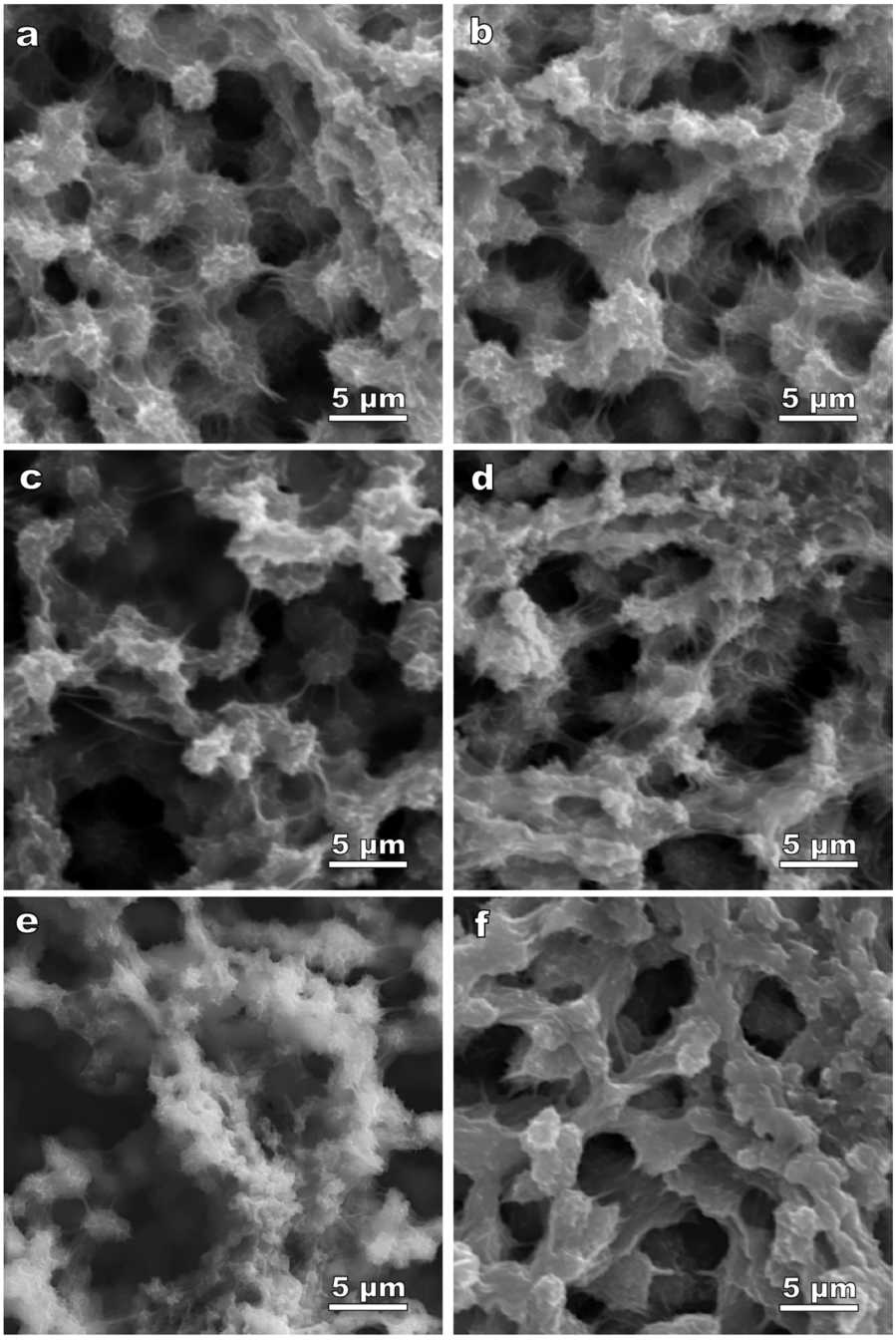

Figure 4.9: SEM images of vanadium oxide films from a) an aqueous whole cell with 3.0 M NaCl at pH 3.0 electrolyte with no cycling and b) after 500 mV s^{-1} cycling and from c) an aqueous whole-cell with 13.34 g L^{-1} agar gel electrolyte prepared with 3.0 M NaCl at pH 3.0 with no cycling and d) after 500 mV s^{-1} cycling and from e) a nonaqueous whole-cell with 1.0 M LiBr electrolyte in DMSO with no cycling and f) after 500 mV s^{-1} cycling. The agar gel was removed by brief exposure to 3.0 M NaCl at pH 3.0 and approximately 100 °C.

4.3.5 Qualitative Compositional Analysis

Compositional analysis was performed on the vanadium oxide electrodes tested in aqueous and nonaqueous whole-cell systems using EDS, and the results are reported in Figure 4.10. The electrodes cycled in aqueous whole-cells containing NaCl electrolyte demonstrated the presence of C due to the carbon-coating, Na and Cl due to the electrolyte and small peaks for S most likely originating from the deposition electrolyte. The electrodes cycled in the nonaqueous LiBr electrolytes both displayed the presence of S and Br, but the DMSO system seemed to exhibit a higher intensity for both. The higher intensity for S is expected due to the solvent composition; however, the higher intensity for Br is not initially obvious. In the previous discussion over the difference between the electrode morphology before and after cycling in the DMSO system (see Figure 4.9e and 9f), one argument proposed the cause to be irreversible intercalation of electrolyte ions. Although the lack of quantitative compositional data for both Li and Br prevents certainty, the higher bromide intensity in the EDS spectra may indicate a higher concentration of intercalated electrolyte ions for the cycled electrode in the DMSO system.

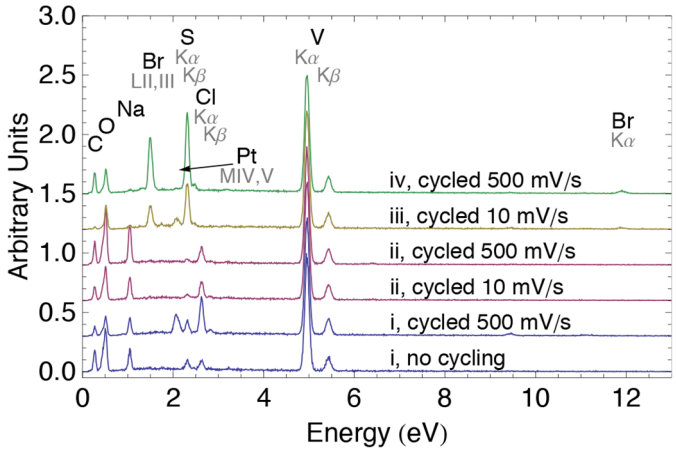

Figure 4.10: EDS of vanadium oxide film electrodes from whole-cells containing i) an aqueous 3.0 M NaCl at pH 3.0 electrolyte, ii) an aqueous 13.34 g/L agar gel electrolyte prepared with 3.0 M NaCl at pH 3.0, iii) a nonaqueous 1.0 M LiBr electrolyte in 100% PC and iv) a nonaqueous 1.0 M LiBr electrolyte in 100% DMSO. The agar gel was removed by brief exposure to 3.0 M NaCl at pH 3.0 and at approximately 100 °C.

4.3.6 Energy and Power Density

The energy and power density for each of the aqueous and nonaqueous vanadium oxide whole-cell systems were calculated before and after cycling using Equations 4.1 and 4.2. The power density was calculated with ESR, or R_s values, chosen from Tables 4.2 and 4.3, and the energy density was calculated from the specific capacitance values before and after cycling calculated from CV at 500 mV s^{-1} and 10 mV s^{-1} as reported in Figure 4.6. The results are listed in Table 4.4. Due to the energy and power ratings, the aqueous NaCl vanadium oxide whole-cells appear

Table 4.4: Power and Energy Density

Electrolyte-Solvent System	Cycling Status	Power Density (kW/kg)	Energy Density (Wh/kg)
3.0 M aqueous NaCl, pH 3.0	Before Cycling (C_s at 500 mV s^{-1})	58	0.8
	Cycled 500 mV s^{-1}	59	3.2
3.0 M aqueous NaCl agar gel, pH 3.0	Before Cycling (C_s at 10 mV s^{-1})	90	8.1
	Cycled 10 mV s^{-1}	82	7.6
	Before Cycling (C_s at 500 mV s^{-1})	90	1.1
	Cycled 500 mV s^{-1}	121	3.4
1.0 M LiBr in PC	Before Cycling (C_s at 10 mV s^{-1})	9	20.9
	Cycled 10 mV s^{-1}	44	20.8
1.0 M LiBr in DMSO	Before Cycling (C_s at 500 mV s^{-1})	45	1.1
	Cycled 500 mV s^{-1}	46	0.4

to be most appropriate for applications requiring a higher power density, and the nonaqueous vanadium oxide whole-cells, particularly the LiBr-PC system, would be most appropriate for higher energy density applications.

4.3.7 Comparison of Present Work to Literature

Although vanadium oxide electrode research has gained momentum in the past few years, most research has been limited to half-cell three-electrode electrochemical characterization [17,18,20,21,23,24], and only a small volume of work is available for comparison to the present work [25,44].

The best performance exhibited by the 3.0 M aqueous NaCl symmetric vanadium oxide whole cell achieved 101 F g^{-1} at approximately 1.3 A g^{-1}, which normalized to the apparent surface area rather than the electrode mass equates to 309 mF cm^{-2} at approximately 4.0 mA cm^{-2}. Wang et al. reported approximately 145 mF cm^{-2} and 170 mF cm^{-2} using 5.0 M LiCl and a LiCl/PVA gel electrolyte, respectively, at approximately the same areal current density. Furthermore, their cells only retained 10% and 85% capacitance retention for the two electrolytes, respectively, after 100 cycles at 100 mV s^{-1} [25]. The present aqueous cells retained 96% capacitance after 3000 cycles at 10 mV s^{-1} and increased in capacitance and stabilized at its maximum capacitance after 50,000 cycles at 500 mV s^{-1}. After cycling at 10 mV s^{-1} and 500 mV s^{-1}, the cells performed with an energy density of 7.6 and 3.4 Wh kg^{-1} and with a power density of 82 and 121 kW kg^{-1}, respectively. Wang et al. did not report energy density or power density values.

Furthermore, the 1.0 M LiBr-PC system exhibited the best nonaqueous electrolyte-solvent performance with a power and energy density of 20.8 Wh kg^{-1} and 44 kW kg^{-1}, respectively, after 2000 cycles at 10 mV s^{-1}. Wei et al. reported a symmetric vanadium oxide electrochemical capacitor utilizing a room-temperature ionic liquid (RTIL) system containing a compatible Li salt, which exhibited 0.5 Wh kg^{-1} at 0.4 kW kg^{-1} with a nontemplated vanadium oxide electrode

and 13.9 Wh kg^{-1} at 16.7 kW kg^{-1} with a templated electrode [44]. Compared to the RTIL system, the LiBr-PC system exhibits higher power capabilities though not as high as the aqueous system.

4.4 Conclusion

Separator materials and designs were studied for symmetric vanadium oxide whole-cell assemblies. The 0.050 mm Nafion® membrane was the optimal separator compared to the alternative separators and spacer designs studied according to capacitive and impedance data.

The aqueous systems utilizing a 3.0 M NaCl electrolyte at pH 3.0 exhibited an excellent 96% capacitance retention over 3000 cycles at 10 mV s^{-1}. The same system tested at 500 mV s^{-1} displayed an increase in capacitance over the first several thousands of cycles, and eventually stabilized over 50,000 cycles. SEM results showed that there was no change in morphology associated with the cycling; however, a decrease in the interfacial charge transfer resistance calculated from EIS modeling suggests the increase in capacitive performance is associated with an increase in the oxide electrical conductivity.

The electrodes cycled in nonaqueous 1.0 M LiBr in PC exhibited mostly non-capacitive charge-storage over the first 1000 cycles at 10 mV s^{-1}. SEM studies indicate that the charge passed during this period resulted in a significant change in morphology perhaps accompanied by a phase change. The whole-cells containing DMSO exhibited a gradual capacitive decay over 10,000 cycles at 500 mV s^{-1} as well as a slightly coarser morphology, which may have been caused by irreversible electrolyte intercalation during cycling.

The aqueous and nonaqueous whole-cells both exhibited excellent power and energy densities. However, the aqueous systems may be more appropriate for high power density applications due to the lower ESR associated with the high electrolyte conductivity, and the nonaqueous systems, particularly those containing PC as the solvent, may be more useful for high energy density applications due to the higher capacitance associated with slower scan rates over wider operating voltages.

Chapter 5 – Electrophoretically Deposited Graphene Oxide and Vanadium Oxide Composite Electrodes

This material has been submitted for publication:

A. M. Engstrom, F. M. Doyle, B. Chen, submitted to J. Power Sources (2013).[1]

Abstract

Reduced graphene oxide and vanadium oxide composites have been successfully synthesized for electrochemical capacitor electrodes, as confirmed by SEM and Raman spectroscopy. The composite material was found to perform with a higher capacitance than vanadium oxide alone by a factor of 4.0 at 10 mV s^{-1} and 7.5 at 500 mV s^{-1}. Four-point probe analysis determined that the sample resistance of the thermally treated vanadium oxide decreased by a factor of 3.5 with the incorporation of the graphene oxide component in the composite followed by thermal treatment. The composite material was incorporated in both symmetric and asymmetric whole cell devices. Although the asymmetric cell exhibits a 245 kW kg^{-1} and 2.0 Wh kg^{-1} power and energy density, respectively, this cell experienced 100 percent capacitive degradation over 40,000 cycles at 200 mV s^{-1}. The symmetric whole cell performed at a lower capacitance, energy and power density, but was able to retain 34% capacitance after 50,000 cycles.

5.1 Introduction

Electrochemical capacitors, also known as supercapacitors or ultracapacitors, are at the forefront of developing energy storage systems due to their high specific capacitance, high specific power and energy density, long cycle life as well as low material cost and toxicity [1,10-13,63]. Graphene has a high electrical conductivity, and its utilization with a pseudocapacitive metal oxide electrode has the potential to improve the electrical conductance of pathways to the active material, increase the cycle life by improving the mechanical stability of the surface and also provide additional overall capacitance due to charging of the double layer [12,13,64]. Although graphene presents a high theoretical double-layer capacitance of 550 F g^{-1}, its utilization in commercial applications depends on overcoming its typically high-cost of fabrication and various performance challenges [65]. Reduced graphene oxide has emerged as an alternate material enabling inexpensive and scalable mass production of graphene-like films. Reduction

[1] This chapter incorporates the outcome of joint research undertaken in collaboration with the author and LC Tech at NASA Ames Research Center under the supervision of Dr. Bin Chen.

methods such as chemical and thermal treatments are common techniques that partially recover graphene oxide to a state that exhibits graphene-like properties such as high electrical conductivity [66,67].

In addition to the benefits of adding graphene oxide to the metal oxide electrode, it may be possible that an asymmetric device design, with a carbonaceous negative electrode and metal oxide composite positive electrode could be cycled over a larger operating potential window. This larger window may lead to a higher specific energy and maximum specific power density, E_s and P_s, (reproduced for convenience, equivalent to Eq. 3.1 and 3.2) respectively [11,68], as calculated [1,10,11,13] by:

$$E_s = \frac{1}{2} C_s V^2 \tag{5.1}$$

$$P_s = \frac{V^2}{4\, ESR\, m} \tag{5.2}$$

where C_s is the specific capacitance, V is the operating voltage, ESR, also written R_s, is the equivalent series resistance and m is the mass of the electrode material.

Previous research has explored the synthesis procedure and viability of reduced graphene oxide and nanocomposite Co_3O_4 and MnO_2 materials for electrochemical capacitor electrodes [64]. In the current work, vanadium oxide has been studied as another metal oxide material that is desirable due to its wide range of stable oxidation states (V, IV, III and II), its higher abundance and lower cost and toxicity than the traditionally utilized RuO_2 [6]. Vanadium oxide exhibits excellent specific capacitance up to 870 F g^{-1} depending upon the structure, composition and accessible surface morphology as determined by the synthesis and processing methods as well as the testing environment [6,20-22]. Previous studies have reported the anodic electrophoretic deposition of both graphene oxide from exfoliated graphite oxide [64] and vanadium oxide [69], separately, but to the best of our knowledge the simultaneous anodic electrophoretic deposition of both materials to produce a homogeneous composite material has not been reported. This is described here, along with the influence of subsequent processing treatments to improve the electrical conductivity.

5.2 Experimental Methods

5.2.1 Electrophoretic Synthesis

Graphene oxide, vanadium oxide and composite structures containing both materials were synthesized by anodic electrophoretic deposition using a two-electrode setup aligned parallel to the electrolyte solution surface as showing in Figure 5.1 to prevent film delamination during removal following deposition. The potential was applied across a 3.0 mm gap between two stainless steel disc electrodes with approximately 0.5 cm^2 surface area exposed to the electrolyte.

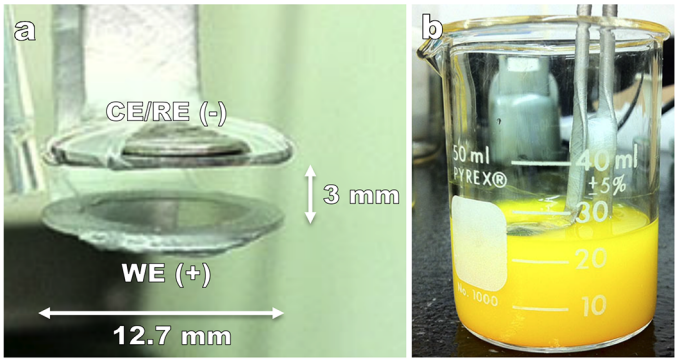

Figure 5.1: Electrophoretic deposition experimental setup showing a) horizontal disc electrodes 12.7 mm in diameter with approximately 8.0 mm diameter exposed to the electrolyte and separated approximately 3 mm apart and attached to stainless steel current collectors as well as b) an image depicting the electrode setup immersed in the solution for vanadium oxide deposition.

Graphene Oxide

Graphene oxide films were produced in a multi-step process. All chemicals and materials were purchased from Sigma Aldrich. First, graphene oxide powder was prepared from synthetic graphite (< 20 μm flakes, reagent grade) via a previously reported modified Hummers' method with additional $KMnO_4$ [70]. Next, the powder was exfoliated by ultrasonication in distilled water for several hours then decanted producing a 0.5 mg mL^{-1} suspension. The solution preparation was completed by ultrasonicating the graphene oxide in a 1:4 volumetric ratio mixture of water and acetone immediately before deposition. Lastly, anodic electrophoretic deposition of the graphene oxide films was performed in the aforementioned solution at 50 V for eight (8) minutes.

Vanadium Oxide

Vanadium oxide was produced using a similar method to the graphene oxide synthesis. Vanadium oxide nanowires were hydrothermally synthesized using a method reported elsewhere [71]. A suspension with approximately 1.5 mg mL^{-1} vanadium oxide nanowires in acetone was then prepared and ultrasonicated for over three (3) hours to disperse the nanowires. Utilizing this suspension, anodic electrophoretic deposition was performed at 50 V for four (4) minutes.

Graphene Oxide and Vanadium Oxide Composites

Graphene oxide and vanadium oxide composite electrodes were synthesized by simultaneous anodic electrophoretic deposition from a mixture of the suspensions used in the previous sections. A 1:4 volume mixture of 0.5 mg mL^{-1} graphene oxide in water and 1.5 mg mL^{-1} vanadium oxide in acetone were ultrasonicated together for several minutes immediately prior to deposition. Anodic electrophoretic deposition was performed at 50 V for seven (7) minutes.

5.2.2 Reduction Methods

The graphene oxide and composite films were reduced to partially restore the structure and properties of graphene using either thermal or chemical reduction [66,67]. Thermal reduction was accomplished using a Lindberg Blue MiniMite tube furnace heated to 300 °C in air for 30 minutes including a manual ramp to temperature followed by a natural cool down in air. The appearance of the electrodes indicated a loss of oxygen due to a color change, gray to black for the graphene oxide and yellow to green for the vanadium oxide, observed after the treatment. Chemical reduction was performed by immersion in aqueous 150 mM $NaBH_4$ for two (2) hours for the graphene oxide sample and for four (4) hours for the graphene oxide and vanadium oxide composite sample.

5.2.3 Electrochemical Characterization

Electrochemical characterization was performed using a three-electrode cell comprising a saturated KCl Ag/AgCl reference electrode (0.199 V vs. SHE) from Koslow Scientific, a 5 x 5 cm Pt gauze from Sigma Aldrich as the counter electrode and the oxide deposited on a stainless steel substrate for the working electrode, tested in aqueous electrolyte solutions prepared with distilled water and reagent grade chemicals. Solutions of 3.0 M NaCl were adjusted to various pH using HCl and NaOH. The electrolyte pH was measured with an Orion, Thermo Scientific 915600 pH electrode connected to an Orion 290A pH meter calibrated with pH 7.0, 4.0 and 1.0 buffer solutions prior to each measurement.

The electrodes were electrochemically characterized using cyclic voltammetry (CV), and galvanostatic charge/discharge (GCD) cycles using a PAR 273 potentiostat. Electrochemical impedance spectroscopy (EIS) was performed using a Gamry Series G™ potentiostat and modeled using Echem Analyst™ Software. The impedance of the oxide and composite films was measured using an AC voltage amplitude of 10 mV with respect to the open circuit potential over a frequency range of 100 kHz to 10 mHz, unless otherwise noted.

5.2.4 Materials Characterization

Morphological analyses were performed with a Hitachi S-4800 field emission scanning electron microscope (SEM). Further characterization was performed with a Renishaw inVia Raman spectrometer using a 633 nm laser and equipped with a Leica microscope. Sample resistance was measured with a four-point probe station (MMR Technologies) equipped with a 6220 Keithly precision current source and 6514 Keithly system electrometer.

5.2.5 Whole Cell Design

Symmetric and asymmetric cells were assembled to test the capacitance as well as power and energy density performance of the composite materials. The symmetric cell consisted of thermally reduced vanadium oxide and graphene oxide composite electrodes for both the positive and negative electrode, whereas the asymmetric cell was composed of the composite for the positive electrode and a thermally reduced graphene oxide deposited on stainless steel mesh for the negative electrode, to allow for a larger electrochemical potential window. The graphene

oxide was deposited on stainless steel mesh using the same procedure described in Section 2.1.1 except for a reduced deposition time of two (2) minutes rather than the standard eight (8) minutes. Both types of cells contained 0.50 mm thick Nafion® membranes and 3.0 M NaCl at pH 5.0 electrolyte solutions, wetted throughout acting as the physical and electrical separation of the positive and negative electrodes.

5.3 Results and Discussion

5.3.1 Electrolyte Compatibility

Previous work determined that the optimal pH for the vanadium oxide system was 3.0 (see Chapter 2) and a later study identified the preferred electrolyte solution as 3.0 M NaCl (see Section 3.3.1). However, in a variable pH experiment the electrolyte compatibility of stainless steel (see Figure 5.2) and graphene oxide (see Figure 5.3) indicates a less than ideal environment at pH 3.0. EIS data of stainless steel in contact with solutions at pH 3.0, 5.0, 7.5 and 13.6 are plotted in Figure 5.2a, and the data was fit to an equivalent circuit model illustrated in Figure 5.2b, which has been described previously (see Chapters 3 and 4). The fitting parameters are reported in Table 5.1 and plotted on top of the data markers. The low equivalent circuit resistance, R_s, and moderately lower charge transfer resistance, R_a, are two benefits to the pH 5.0 environment. In Figure 5.3, graphene oxide films deposited on stainless steel substrates were

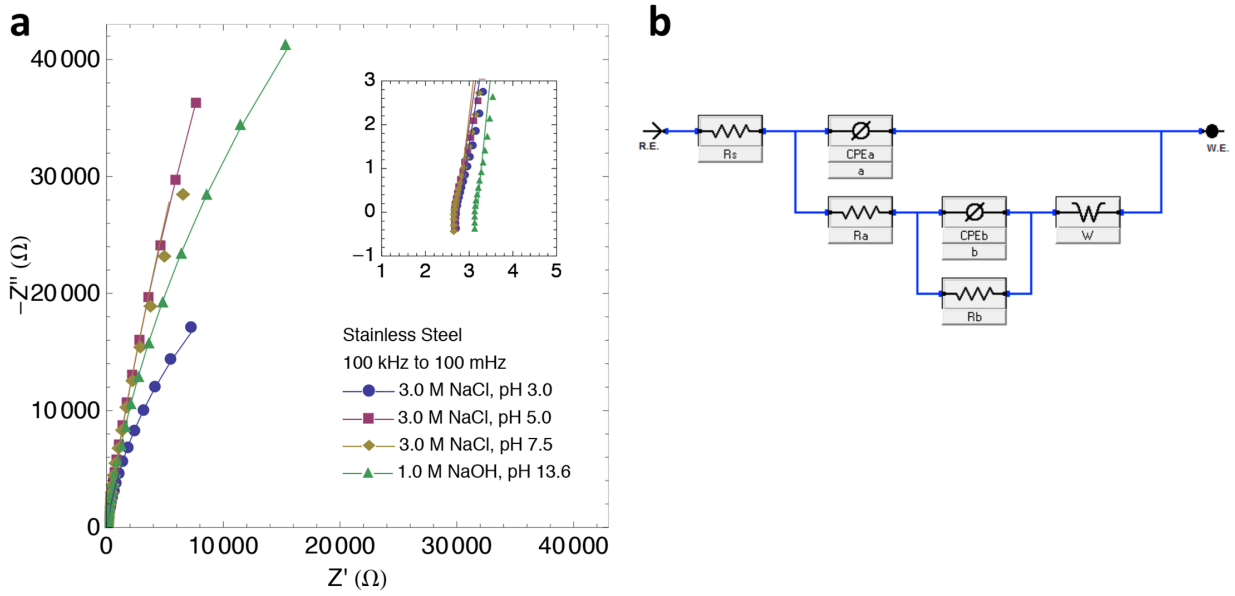

Figure 5.2: EIS data for a) stainless steel substrates in various aqueous electrolyte solutions as well as the b) equivalent circuit model used to fit the data. The markers represent the real data and the corresponding lines represent the fitted model with parameters reported in Table 5.1. The inset graph depicts the high frequency region of the EIS data and fitted model.

Table 5.1: Fitting Parameters for EIS Modeling of Stainless Steel in Various Electrolyte Solutions

Electrolyte Solution	R_s (Ω)	A ($S \cdot s^a$)	a	R_a (Ω)	B ($S \cdot s^b$)	b	R_b (Ω)	W ($S \cdot s^{0.5}$)	Goodness of Fit
3.0 M NaCl, pH 3.0	2.752	7.58×10^{-5}	0.898	7.06×10^{4}	2.88×10^{-2}	0.625	3.76×10^{2}	5.13×10^{-4}	1.18×10^{-3}
3.0 M NaCl, pH 5.0	2.716	4.04×10^{-5}	0.909	7.03×10^{3}	1.21×10^{-7}	1.000	4.47×10^{5}	1.08×10^{-5}	1.35×10^{-3}
3.0 M NaCl, pH 7.5	2.732	5.07×10^{-5}	0.923	2.55×10^{4}	6.26×10^{-8}	0.304	6.18×10^{4}	5.14×10^{-6}	1.88×10^{-3}
1.0 M NaOH, pH 13.6	3.184	2.60×10^{-5}	0.946	7.08×10^{1}	7.29×10^{-6}	0.725	2.14×10^{5}	4.08×10^{-4}	9.65×10^{-4}

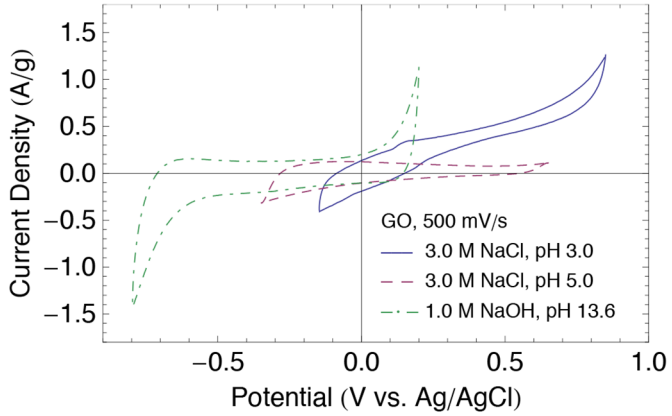

Figure 5.3: Electrolyte compatibility elucidated by cyclic voltammetry of graphene oxide electrophoretically deposited on stainless steel substrates and tested in various aqueous electrolyte solutions.

cycled using cyclic voltammetry in pH 3.0, 5.0 and 13.6. The film is most electrochemically stable in pH 5.0. The high current response in the chloride environment at pH 3.0 is likely due to pitting corrosion of the stainless steel in the transpassive region. Therefore, an electrolyte of 3.0 M NaCl at pH 5.0 was utilized in all following electrochemical studies.

5.3.2 Composite Half-Cell Capacitance and Cycle Behavior

Graphene oxide (GO) and composite films containing vanadium oxide and graphene oxide underwent either thermal or chemical reduction treatments. SEM images of the as-deposited and treated films are reported in Figure 5.4. The as-deposited graphene oxide is relatively planar (see Figure 5.4a) whereas the treated films (Figures 5.4b,c) appear to have more texture due to the reduction. In addition, visual inspection of the films confirmed a color change from brown to black, indicative of a partial recovery of the sp^2-hybridized graphitic framework [72]. The graphene oxide and vanadium oxide composite (GO/V_xO_y) is shown in Figure 5.4d with an inset image of vanadium oxide nanowires deposited without the graphene oxide component for

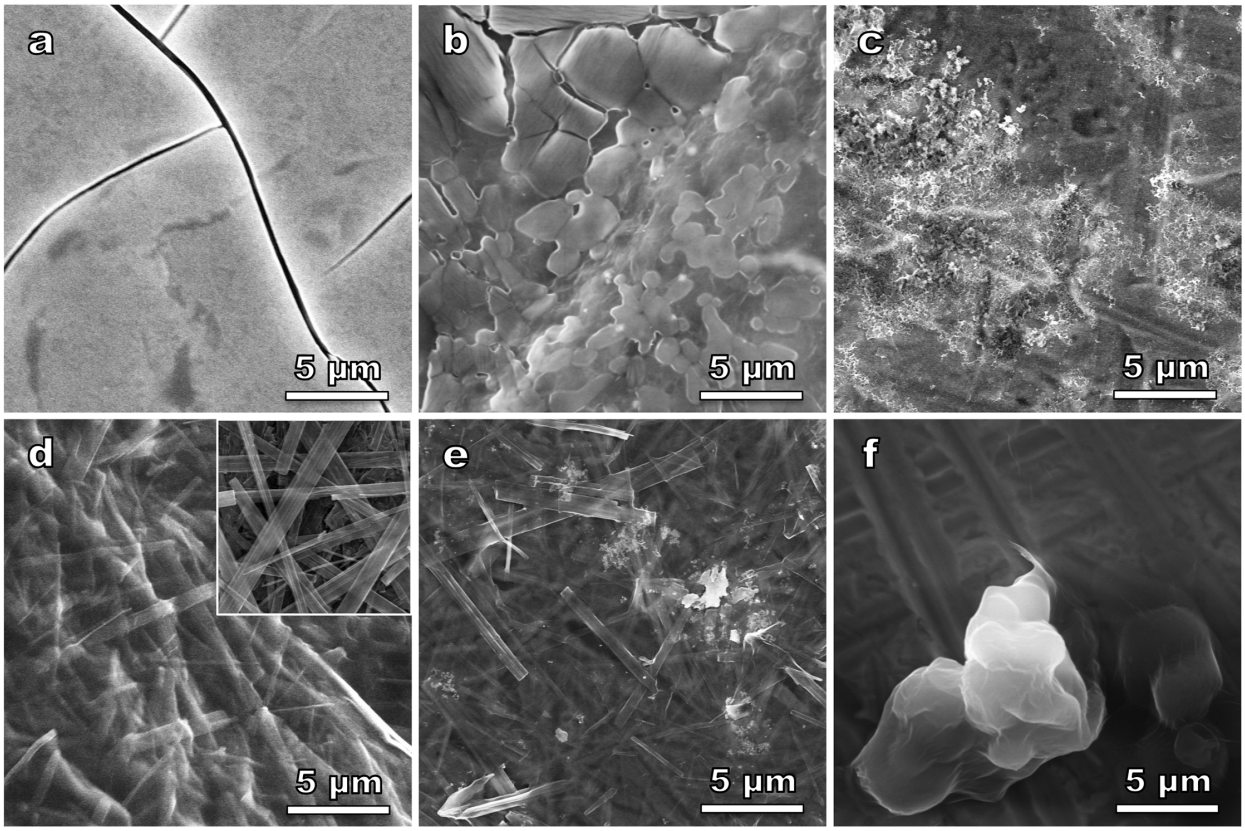

Figure 5.4: SEM images of a) electrophoretically deposited graphene oxide (GO), b) thermally reduced GO, c) chemically reduced GO, d) (inset) deposited vanadium oxide nanowires and (main) simultaneously deposited graphene oxide and vanadium oxide (GO/V_xO_y), e) thermally reduced GO/V_xO_y and f) chemically reduced GO/V_xO_y.

comparison. The GO/V_xO_y sample appears to have a vanadium oxide nanowire network with graphene oxide filling the space and coating the wires. The charge transfer during the deposition process has clearly provided enough electrical conductivity that they lose their charge and approach each other closely. Otherwise, there may not have been sufficient connectivity between the particles to ensure that the whole array could be electrochemically active. The thermally treated composite, $tr(GO/V_xO_y)$, in Figure 5.4e appears to have maintained the vanadium oxide nanowires while the graphene oxide component has gained texture, presumably due to reduction. Despite the success of the thermal treatment, the chemically treated composite, $cr(GO/V_xO_y)$, did not retain the nanowire network. It is possible that the strongly alkaline environment reacted with the vanadium oxide component, possibly removing it entirely.

The reduced GO and GO/V_xO_y films were cycled in electrochemical half-cells containing 3.0 M NaCl at pH 5.0 using cycling voltammetry at 500 mV s^{-1}. The change in the shape of the voltammograms is illustrated in Figure 5.5, the change in the specific capacitance with cycling is reported in Figure 5.6, and the mass-specific capacitance of the half-cells at various scan rates is reported in Figure 5.7. In Figures 5.6a and 5.6b, the current was normalized to the apparent

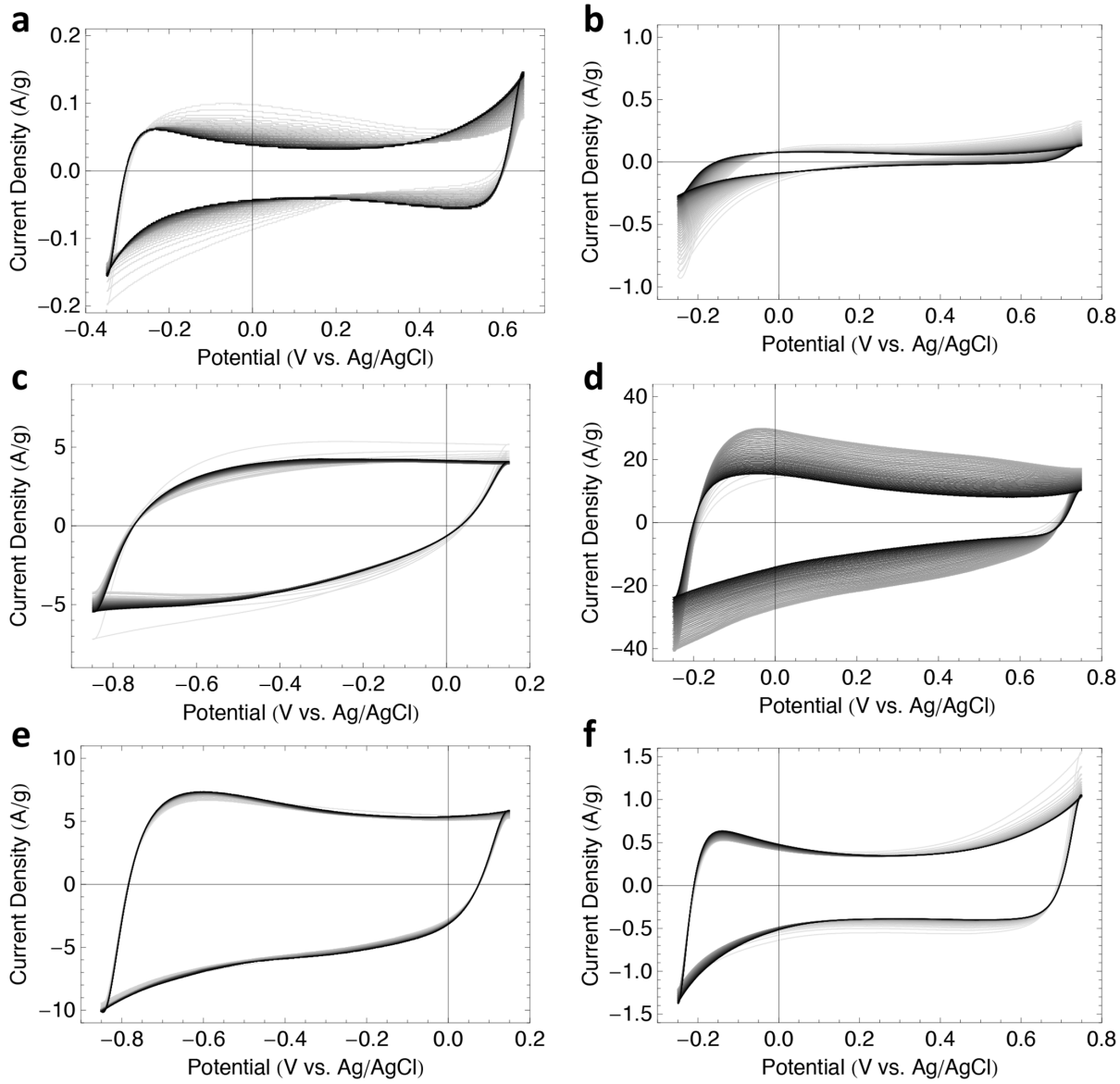

Figure 5.5: Cycle behavior of a) graphene oxide (GO), b) vanadium oxide, c) thermally reduced (tr) GO, d) thermally reduced graphene oxide and vanadium oxide composite, tr(GO/V_xO_y), e) chemically reduced (cr) GO and f) cr(GO/V_xO_y) cycled at 500 mV s^{-1} in 3.0 M NaCl at pH 5.0 aqueous half-cells. One of every 200 cycles is shown, and the color of the cycles is graded from gray to black to denote the progression from the first to the last CV cycle, respectively.

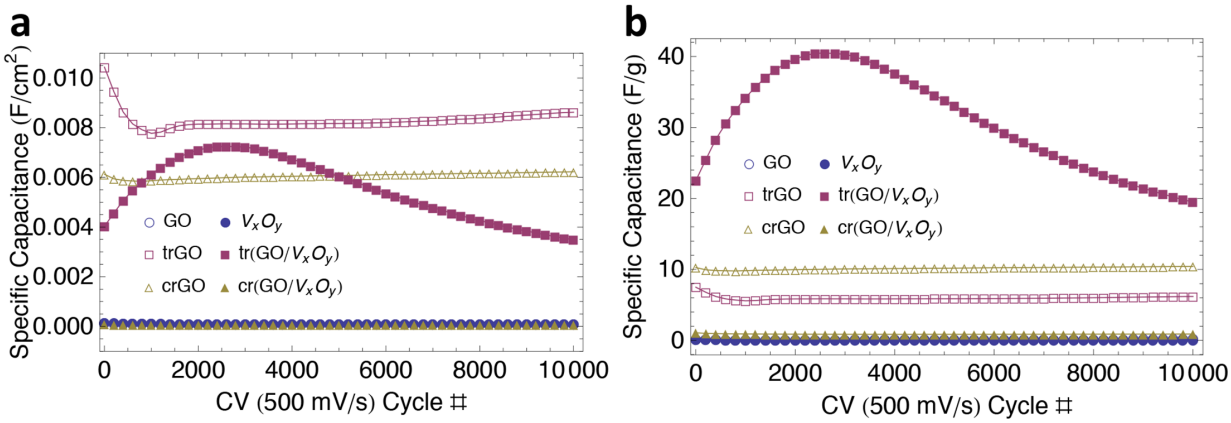

Figure 5.6: Cycle behavior of as-deposited and reduced graphene oxide and vanadium oxide and reduced graphene oxide and vanadium oxide composites in 3.0 M NaCl at pH 5.0 aqueous systems normalized to a) the apparent surface area and b) the mass of the deposited material.

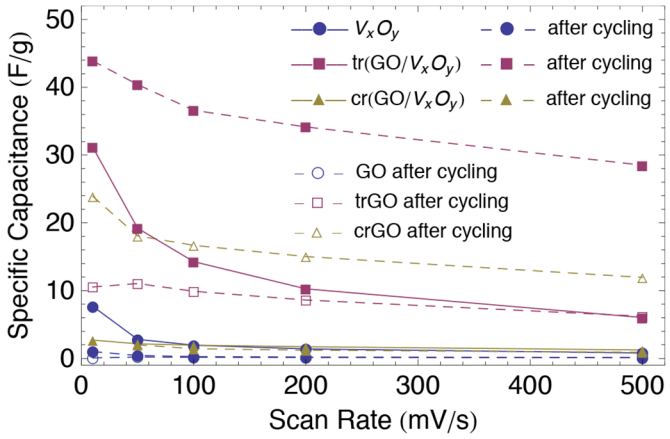

Figure 5.7: Capacitance of graphene oxide and reduced forms after cycling and vanadium oxide and reduced graphene oxide and vanadium oxide composites before and after cycling in 3.0 M NaCl at pH 5.0.

surface area of the electrode, approximately 0.5 cm^2, and the mass of the deposit, respectively. Both the thermal and chemical reduction methods produced films with a higher capacitance than the untreated GO. The thermal method had a higher areal-specific capacitance, but the chemical method exhibited a higher mass-specific capacitance. This discrepancy may be explained by the difference in the mass of the two electrodes. The mass of the chemically reduced graphene oxide was a little less than half that of the thermally treated graphene oxide perhaps due to material loss during the chemical reduction process. Furthermore, the tr(GO/V_xO_y) sample exhibited a marked capacitive improvement over the V_xO_y sample alone, and a larger mass-specific capacitance compared to the trGO and crGO electrodes. According to Figure 5.7, the thermally

reduced composite material exhibited a 4.0 times larger capacitance at 10 mV s^{-1} and 7.5 times larger at 500 mV s^{-1}. The graphene oxide component appeared to improve the rate performance of the vanadium oxide charging mechanism. The cr(GO/V_xO_y) sample was found to perform with little capacitance, which is consistent with the lack of active material as discussed for its SEM image in Figure 5.4f.

5.3.3 Raman Spectroscopy

In order to understand the capacitive and cycling behavior of the films, Raman spectroscopy (see Figure 5.8) was performed. Figure 5.8a illustrates the Raman spectra for the GO and reduced GO films before and after cycling, and Figure 5.8b reports the spectra for the V_xO_y and GO/V_xO_y as-prepared and after thermal treatment. Furthermore, the spectra were fitted using the Wire 2.0 Renishaw software, and the calculated peak centers and widths of the characteristic graphene oxide peaks are reported in Table 5.2. The G peak corresponds to the optical vibrational mode of two neighboring carbon atoms on a graphene layer, the D and D' bands are defect-induced Raman scattering and lastly the G' band is the second-order or overtone of the D band that is sensitive to the stacking order of graphene sheets along the c-axis [73,74]. The final column in Table 5.2 reports the ratio of the integrated area of the D and G peaks, I_D/I_G. This ratio is a sensitive measure of the quantitative degree of disorder and the crystallite size of the graphitic layers [72,73].

When comparing the reduced forms of the graphene oxide to the unreduced film (GO), many of the bands in the crGO sample exhibit a shift to lower energy (red-shift), whereas the trGO sample exhibits a shift to higher energy (blue-shift). The chemical treatment may reduce the stress in the lattice by removing oxygen in functional groups on the graphene oxide sheets. The thermal treatment may introduce more stress in the lattice by removal of oxygen and water at high temperature, followed by possible stress-inducing re-oxidation at the surface upon cooling. Furthermore, the G band for both types of reduced films exhibits a bandwidth reduction indicative of less disorder due to a narrower range of clusters or configurations with different local band gaps and different phonon modes [75]. Both reduction methods produced peaks with narrower D' bands due to less first-order defects in the graphitic framework, but trGO exhibits a much wider G' band suggesting that the thermal treatment causes more stacking order defects than the chemical methods, perhaps due to a more thorough reduction throughout the bulk of the film. Lastly, the I_D/I_G ratio increases after both reduction methods. Each method introduces more defects in the graphene oxide by removing oxygen, but the ratio is larger for crGO. Considering the above analysis, the chemical reduction method may introduce a larger quantity of defects, mostly in the plane of the graphene oxide sheets, but the thermal reduction technique introduces a larger range of defects including stacking order defects. Defects and surface functional groups in graphene oxide are known to lead to a considerable pseudocapacitive effect [76], which may partially explain the superior capacitance of the reduced films due to a larger quantity of defect sites.

Cycling of the as-deposited and reduced graphene oxide films over 10,000 cycles in 3.0 M NaCl at pH 5.0 produced various shifts and changes in peak widths of the characteristic peaks. Although few changes were observed in the D, G and D' bands, the G bandwidth was wider for all cycled GO, crGO and trGO samples than for their uncycled counterparts. Cycling has clearly

increased the degree of disorder in the graphitic framework. Furthermore, the G' band exhibited a blue shift for the cycled GO sample but a red shift for the cycled trGO sample. The cycling has induced stress in the GO lattice, perhaps due to irreversible intercalation of sodium ions during cycling due to a small amount of pseudocapacitive charging. On the other hand, the energy of the G' peak decreases as the trGO sample is cycled and moves closer to that of the as-deposited GO value. Perhaps with cycling, the rehydration of the sample between the graphene oxide sheets helps to alleviate some of the stress induced during the thermal treatment. In addition, the G' band is wider after cycling of the GO and crGO sample but becomes narrower for the cycled trGO sample. This change indicates that a larger range of stacking defects is introduced into the GO and crGO, perhaps due to intercalation effects. However, the range of defects is lowered for the trGO sample after cycling. The thermal treatment itself introduced a large range of stacking defects, but the cycling seems to cause a reduction of this range of defects, perhaps by promoting

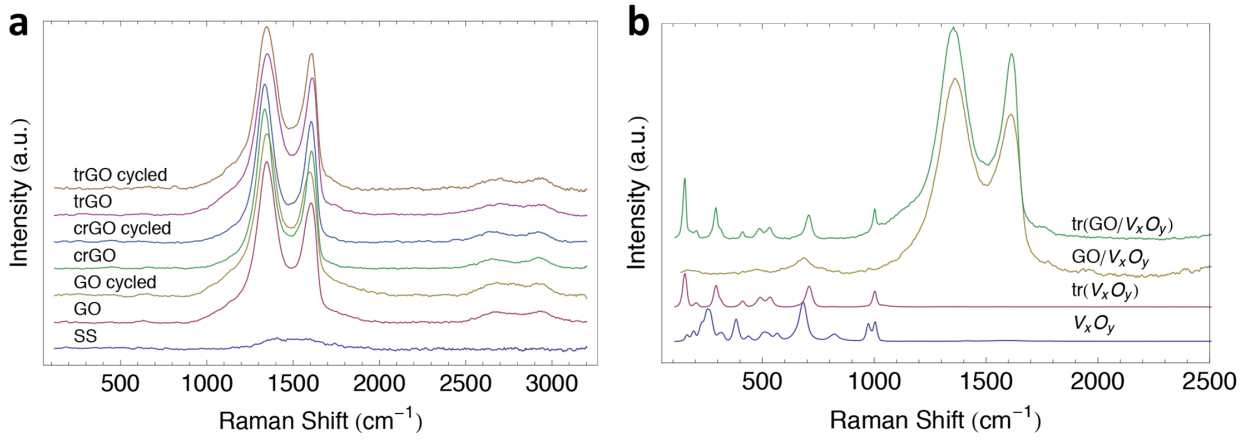

Figure 5.8: Raman spectra of a) as-deposited and reduced graphene oxide before and after cycling and of b) as-deposited and reduced vanadium oxide as well as graphene oxide and vanadium oxide composites. Peak analysis is reported in Table 5.2.

Table 5.2: Raman Peak Fitting Parameters

Sample	Peak Center (cm^{-1})				Peak Width (cm^{-1})				I_D/I_G
	D	G	D'	G'	D	G	D'	G'	
GO	1348	1518	1603	2688	122	159	70	203	3.0
GO after cycling	1347	1517	1598	2714	120	223	73	242	1.4
trGO	1352	1545	1611	2707	147	134	60	309	3.5
trGO after cycling	1348	1545	1607	2694	129	184	59	220	2.0
crGO	1335	1521	1605	2671	109	143	58	212	5.1
crGO after cycling	1337	1521	1603	2668	110	156	61	233	4.5
GO/V_xO_y	1355	1542	1610	2734	149	147	71	316	3.5
tr(GO/V_xO_y)	1355	1551	1615	2705	148	128	59	253	4.0

more order in the stacking. Furthermore, the I_D/I_G ratio decreases with cycling of all samples, demonstrating that cycling has reduced the quantity of defects.

Figure 5.8b compares the Raman spectra of the graphene oxide composites with those of vanadium oxide alone. For further comparison, a thermally treated sample of vanadium oxide, tr(V_xO_y), is also plotted. The as-deposited vanadium oxide film exhibits peaks at 160, 190, 225, 260, 315, 380, 435, 515, 565, 682, 822, 972 and 1002 cm^{-1}. However, after thermal treatment, the sample exhibits peaks at 150, 203, 290, 315, 410, 487, 532, 708 and 1000 cm^{-1}, which closely agrees with V_2O_5 peaks reported in the literature [77]. The GO/V_xO_y sample exhibits the graphene oxide peaks, but the vanadium oxide peaks are not fully defined until after thermal treatment to tr(GO/V_xO_y). Compared with GO, all bands, especially the G and G' bands, for the GO/V_xO_y sample demonstrate a blue shift in their phonon energy. The addition of the vanadium oxide component appears to add additional stress that may impede the phonon movement. However, the G bandwidth is narrower, indicating that the graphitic network is less disordered. Nevertheless, the D and G' bands are wider and the I_D/I_G ratio is larger, indicating there is both an increased range and quantity of defects in the plane and stacking order of the graphene oxide sheets. Compared to the GO/V_xO_y sample, the tr(GO/V_xO_y) sample presents a blue shift for the G and D' bands but a red shift for the G' band. The blue shift is consistent with the trend observed for the thermal treatment of the GO film; however, the red shift in G' indicates that there is less stress associated with the stacking between the graphene sheets. Perhaps with the thermal treatment, the V_xO_y, also loses oxygen, allowed for a reduction in stress between the interspatial regions of the graphene oxide component. In addition, narrower peaks were exhibited for all bands, especially the G' peak, which is inconsistent with the wider peak of the GO sample after thermal treatment. The thermal treatment of the composite material may have increased the degree of order throughout, since the loss of oxygen in the V_xO_y, perhaps accompanied with a loss of volume, allowed for movement and restructuring of sheets around it. Lastly, the I_D/I_G ratio increased with the thermal treatment, which is consistent with the trGO sample, and indicative of an increase in defect quantity.

5.3.4 Film Resistance

In order to study the effect of the graphene oxide component in the composite material, the electrical conductivity was studied using a four-point probe. Thermally reduced V_xO_y exhibited a 26.4 kΩ resistance, and the thermally reduced GO/V_xO_y composite presented a 7.7 kΩ resistance. The presence of the reduced graphene oxide component resulted in a 3.5 times reduction in electrode resistance demonstrating the dominance of the carbonaceous component in determining the overall conductivity.

5.3.5 Electrochemical Impedance Spectroscopy

The EIS data for the as-deposited and reduced forms of GO before and after cycling are reported in Figure 5.9. The data were fitted to the equivalent circuit model from Figure 5.2b and the parameters involved in the fit are listed in Table 5.3. The equivalent series resistance, R_s, is highest for the trGO sample, most likely due to the lack of water following the thermal treatment. After cycling, the series resistance decreases and the charge transfer resistance, R_a, increases perhaps due to rehydration, which may cause an increase in ionic conductivity but also a

simultaneous decrease in electrical conductivity [78]. Furthermore, the series resistance decreased with cycling for all samples. According to the Raman analysis, the defect quantity appears to decrease with cycling, which may also help to explain the decrease in series resistance since electrical conductivity may be affected by defects in the bulk. The resistance associated with the pseudocapacitive mechanism, R_b, decreases with cycling for the crGO but especially the trGO sample, which is accompanied by an increase in the associated capacitive quantity, B. However, the double-layer charging components, A and R_a, do not follow the same trend. This

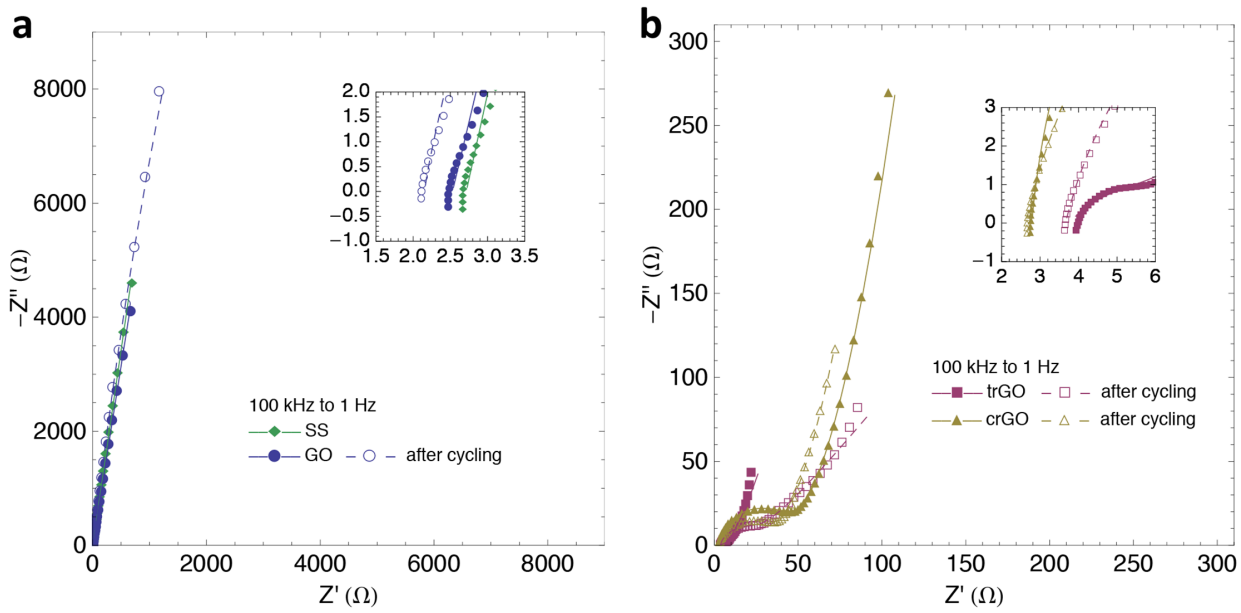

Figure 5.9: EIS before and after cycling of a) graphene oxide compared with bare stainless steel as well as b) reduced graphene oxide. The markers represent the real data and the corresponding lines represent the fitted equivalent circuit model depicted in Figure 5.2b with parameters reported in Table 5.3. The inset graphs depict the high frequency region of the EIS data and fitted model.

Table 5.3: Fitting Parameters for EIS Modeling of Aqueous Half-Cells: Graphene Oxide

Sample	R_s (Ω)	A ($S \cdot s^a$)	a	R_a (Ω)	B ($S \cdot s^b$)	b	R_b (Ω)	W ($S \cdot s^{0.5}$)	Goodness of Fit
GO	2.529	4.67×10^{-5}	0.900	2850	4.54×10^{-4}	0.835	6.74×10^{0}	5.48×10^{-12}	1.72×10^{-3}
GO after cycling	2.158	6.82×10^{-6}	1.000	0.00373	1.57×10^{-5}	0.904	1.88×10^{5}	8.59×10^{-4}	1.02×10^{-3}
trGO	3.770	1.30×10^{-3}	0.581	3.04	5.13×10^{-3}	1.000	3.77×10^{3}	1.29×10^{-2}	1.04×10^{-3}
trGO after cycling	3.663	5.29×10^{-5}	0.853	21.7	1.74×10^{-2}	1.000	7.30×10^{1}	3.95×10^{-3}	6.86×10^{-4}
crGO	2.786	1.61×10^{-5}	0.948	42.9	7.62×10^{-4}	1.000	6.20×10^{4}	4.25×10^{-3}	9.56×10^{-4}
crGO after cycling	2.632	4.97×10^{-5}	0.866	33.0	1.98×10^{-3}	1.000	2.13×10^{4}	7.22×10^{-3}	1.22×10^{-3}

result may help explain the nature of the cycle behavior in Figure 5.6. Although carbon materials are traditionally dominated by double-layer charging, the as-deposited and reduced forms of graphene oxide appear to be dominated by pseudocapacitive mechanisms.

EIS analysis was also utilized for vanadium oxide alone, as well as the reduced GO/V_xO_y composites before and after cycling, as reported in Figure 5.10. The data were fitted to the equivalent circuit model in Figure 5.2b and the fitting parameters are listed in Table 5.4. The

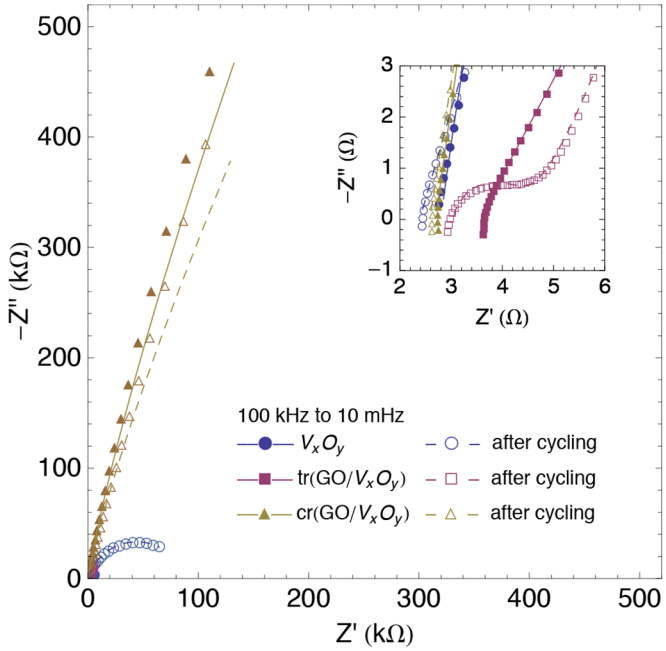

Figure 5.10: EIS of vanadium oxide and the reduced graphene oxide and vanadium oxide composites before and after cycling. The markers represent the real data and the corresponding lines represent the fitted equivalent circuit model depicted in Figure 5.2b with parameters reported in Table 5.4. The inset graph depicts the high frequency region of the EIS data and fitted model.

Table 5.4: Fitting Parameters for EIS Modeling of Aqueous Half-Cells: Vanadium Oxide and Composites

Sample	R_s (Ω)	A ($S \cdot s^a$)	a	R_a (Ω)	B ($S \cdot s^b$)	b	R_b (Ω)	W ($S \cdot s^{0.5}$)	Goodness of Fit
V_xO_y	2.801	6.66×10^{-6}	0.928	2.07×10^{-3}	1.25×10^{-4}	0.403	2.34×10^{3}	7.91×10^{-4}	9.15×10^{-4}
V_xO_y after cycling	2.384	5.74×10^{-5}	0.821	8.46×10^{-8}	5.40×10^{-11}	0.407	8.84×10^{4}	4.39×10^{-2}	1.14×10^{-3}
tr(GO/V_xO_y)	3.536	5.56×10^{-4}	0.687	1.76×10^{2}	2.12×10^{-2}	0.486	1.40×10^{4}	8.36×10^{-11}	1.31×10^{-3}
tr(GO/V_xO_y) after cycling	3.050	2.14×10^{-5}	0.973	1.32×10^{0}	2.43×10^{-3}	0.945	1.09×10^{5}	2.54×10^{-2}	9.97×10^{-4}
cr(GO/V_xO_y)	2.693	2.07×10^{-5}	0.912	6.62×10^{-2}	2.52×10^{-3}	0.854	1.62×10^{1}	1.87×10^{-6}	1.33×10^{-3}
cr(GO/V_xO_y) after cycling	2.582	2.26×10^{-5}	0.902	2.51×10^{0}	1.86×10^{-1}	0.710	2.54×10^{-1}	2.94×10^{-6}	1.80×10^{-3}

thermally reduced composite material has a larger equivalent series resistance than the vanadium oxide alone. This is most likely due to water loss resulting in a decrease in ionic conductivity caused by the thermal treatment despite any improvement in the electrical conductivity caused by the presence of the carbonaceous component. In addition, the cycling of all samples listed in Table 5.4 decreased the series resistance, which is similar to the behavior observed for the graphene oxide samples. Also compared to the vanadium oxide alone, the tr(GO/V_xO_y) sample exhibited a larger value of *B* associated with pseudocapacitance, which is consistent with the capacitance reported in Figure 5.7. With cycling, although the pseudocapacitive element, *B*, decreases and the resistive element, R_b, increases, the constant phase element exponent, *b*, increases, which is indicative of more ideal capacitive behavior.

The electrochemical impedance spectroscopic data analysis appears to be consistent with the cyclic voltammetric data regarding the pseudocapacitive performance of the graphene oxide and graphene oxide and vanadium oxide composite materials.

5.3.6 Whole Cell Performance

The thermally reduced graphene oxide and vanadium oxide composite, tr(GO/V_xO_y), electrode was utilized in two types of whole cell devices to test its capacitance, cycle behavior as well as energy and power density performance. The symmetric type of cell uses identical composite electrodes as both the positive and negative electrodes, whereas the asymmetric cell utilizes an electrode containing only thermally reduced graphene oxide (trGO) deposited on a higher surface area stainless steel mesh as the negative electrode cycled against the composite electrode as the positive electrode. Cyclic voltammetry was utilized to test the operational potential window for the symmetric (see Figure 5.11a) and asymmetric (see Figure 5.11b) cells. The upper potential boundary was progressively increased up to 0.7 V for the symmetric cell and up to 1.1 V for the asymmetric cell. The asymmetric cell is capable of a larger potential window due to the nature of using two different materials for the positive and negative electrodes. The capacitance of the two types of cells is reported in Figure 5.11c using cycling voltammetry at various rates and in Figure 5.11d using galvanostatic charge/discharge at various current densities cycled from 0 to 0.5 V for the symmetric cell and from 0 to 1.0 V for the asymmetric cell. The asymmetric cell performed approximately four times better at 50 mV s^{-1} and eight times better at 500 mV s^{-1}. The addition of the trGO component to the composite material had similarly improved the half-cell specific capacitance at the fast charge/discharge rates. The symmetric cell contains a smaller percentage of trGO material on its negative electrode than the asymmetric cell; therefore, a similar conclusion could be extended to the entire device, that the inclusion of trGO increases the performance at faster charge/discharge rates.

The cells were then repeatedly cycled using cyclic voltammetry at 200 mV s^{-1} up to 50,000 cycles. The progression of the cycle shape is illustrated in Figure 5.12a and 11b for the symmetric and asymmetric cells, respectively. The capacitance calculated over the cycling duration is plotted in Figure 5.12c. Although the asymmetric cell initially has a much larger capacitance, it degrades much faster than the symmetric cell, losing all usable capacitance before 40,000 cycles. The symmetric cell lost 38 percent capacitance over the first 10,000 cycles, but lost only another 28 percent over the remaining 40,000 cycles.

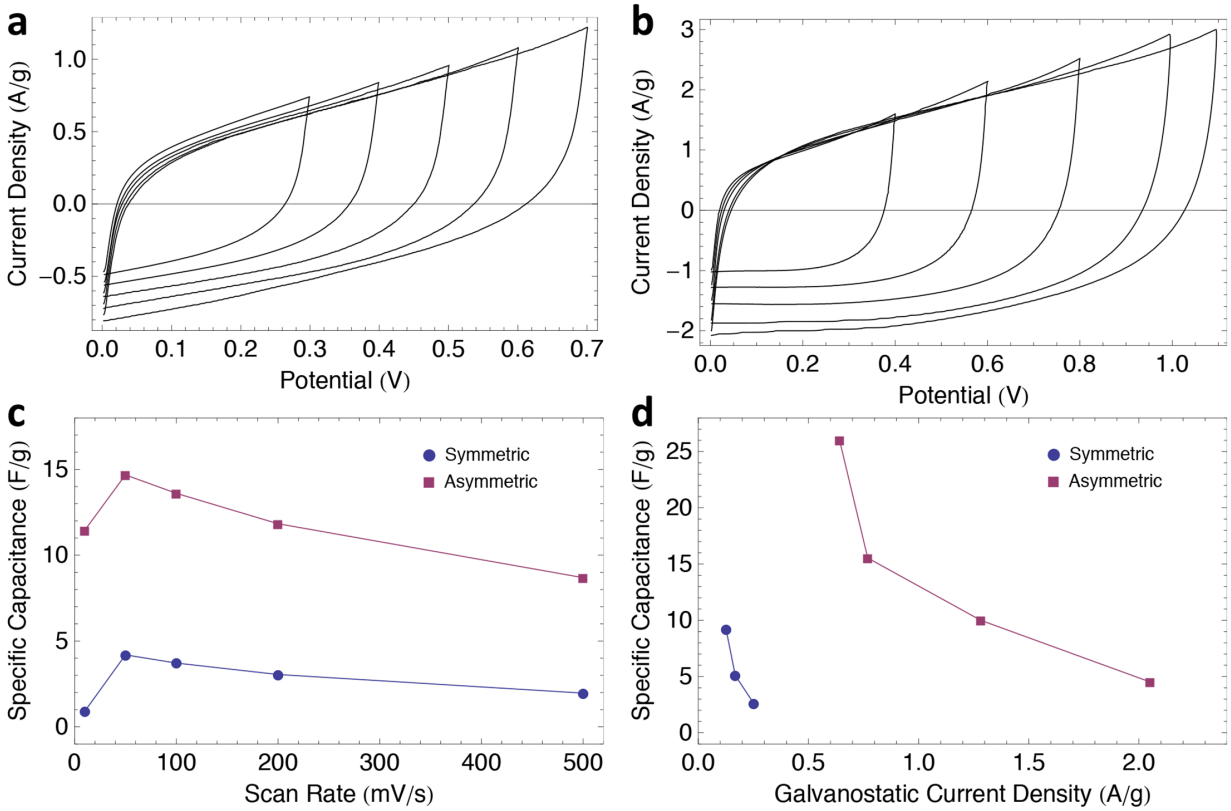

Figure 5.11: Cyclic voltammetry of a) symmetric whole cell up to 0.7 V and b) asymmetric whole cell up to 1.1 V at 200 mV s^{-1} as well as the capacitive performance of both whole cells at various c) cyclic voltammetric scan rates and d) galvanostatic current densities. For the capacitive measurements, the symmetric and asymmetric cells were cycled from 0 to 0.5 and 1.0 V, respectively.

Figure 5.13 presents the EIS data for the whole cells before and after cycling. The data were fitted to the model in Figure 5.2b and plotted on top of the data markers, and the fitting parameters are listed in Table 5.5. The series resistance is significantly lower for the asymmetric cell than the symmetric cell. Although the trGO and tr(GO/V_xO_y) sample series resistances are similar in Tables 5.3 and 5.4, the trGO utilized in the asymmetric cell is a much thinner film due to a shorter deposition time than the trGO film on stainless steel substrates reported in Table 5.3. Therefore, the series resistance of the trGO component may be expected to be less than the thicker trGO and the composite materials, which may explain the lower device series resistance compared to the symmetric device containing two composite electrodes. With cycling, the two types of cells experience similar trends in their impedance behavior, such as a decrease in the double-layer capacitance element, *A,* accompanied by an increase in charge transfer resistance, R_a, both of which would cause capacitive degradation such as that seen in Figure 5.12c. As seen for the cycled half-cell samples, the series resistance, R_s, decreased for the symmetric cell with cycling. However, the resistance increased for the asymmetric cell. This phenomenon may be explained by a lower conductivity of the membrane after cycling. Vanadium oxide is known to degrade by material dissolution at pH 5.0 [41], and although Nafion® is ideally a proton

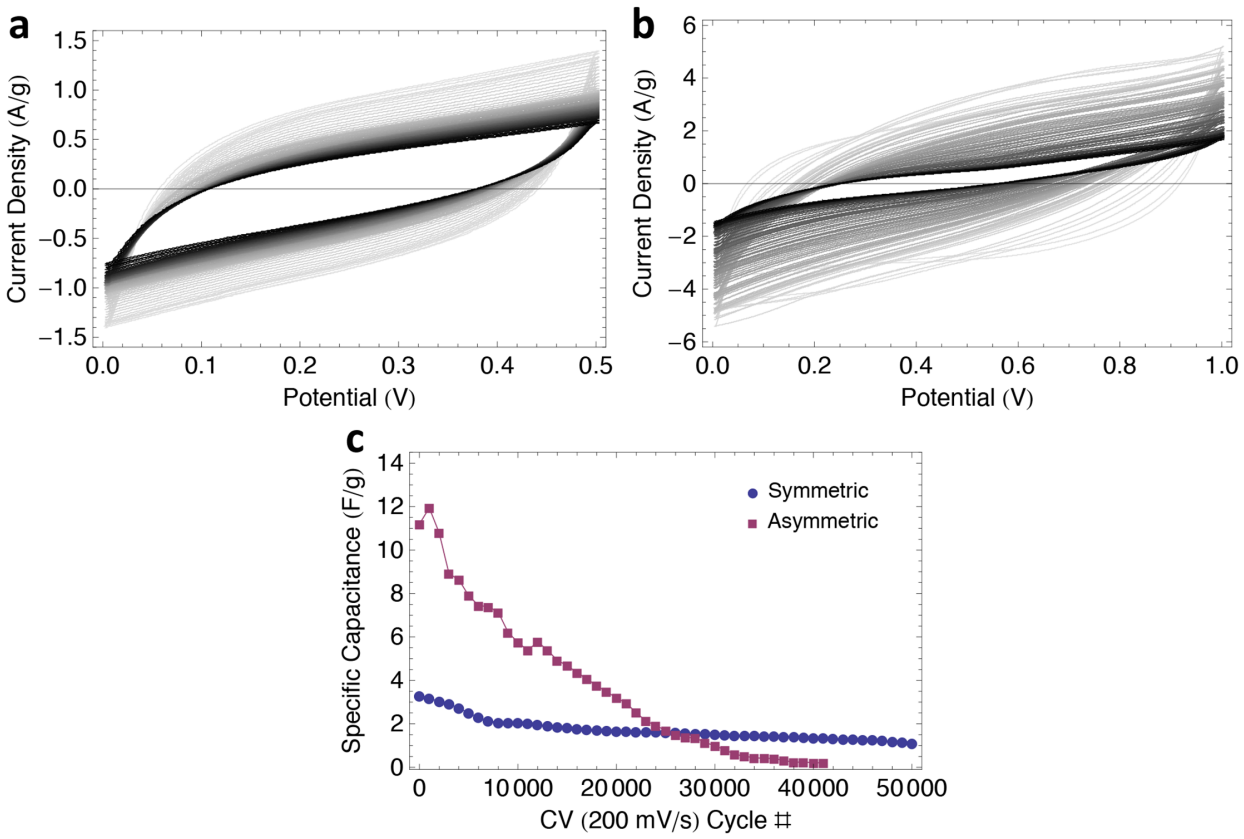

Figure 5.12: Cycle behavior of the a) symmetric and b) asymmetric whole cells cycled at 200 mV s^{-1} and whose capacitance is plotted in c) up to 50,000 cycles. Every 500th cycle is shown, and the color of the cycles is graded from gray to black indicating the progression from the first to the last CV cycle, respectively.

conductor, when exposed to a high concentration of dissolved vanadium ions, crossover does occur [79]. Therefore, during cycling the relatively higher potentials applied across the membrane may initiate ion penetration, potentially blocking proton-conducting pathways and reducing the overall ionic conductivity.

5.3.7 Energy and Power Density

The energy and power density of the whole cells were calculated using Equations 5.1 and 5.2, respectively, from the preliminary CV and EIS analyses (before cycling) reported in Figure 5.11c and Table 5.5. The power density of the symmetric and asymmetric cells is 6.3 kW kg^{-1} and 245 kW kg^{-1}, respectively. The significantly larger power density performance of the asymmetric whole cell is due to the larger potential window and lower equivalent series resistance. At 50 mV s^{-1}, the energy density of the symmetric and asymmetric cells is 0.1 Wh kg^{-1} and 2.0 Wh kg^{-1}, respectively. The larger specific capacitance and larger potential window both yield the larger energy density performance of the asymmetric whole cell. Despite the larger power density, the energy density is one to two orders of magnitude lower than batteries or fuel cells, including

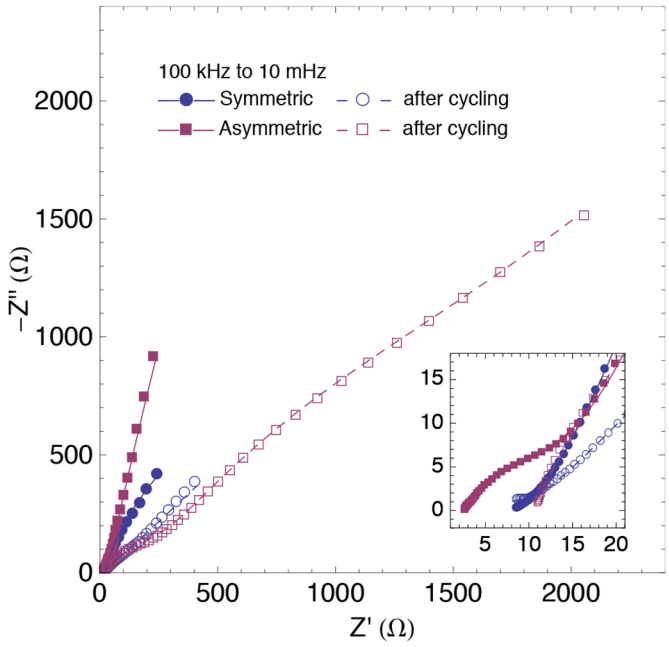

Figure 5.13: EIS of the symmetric and asymmetric whole cells before and after cycling. The markers represent the real data and the corresponding lines represent the fitted equivalent circuit model depicted in Figure 5.2b with parameters reported in Table 5.5. The inset graph depicts the high frequency region of the EIS data and fitted model.

Table 5.5: Fitting Parameters for EIS Modeling of Aqueous Whole Cells

Cell	R_s (Ω)	A ($S \cdot s^a$)	a	R_a (Ω)	B ($S \cdot s^b$)	b	R_b (Ω)	W ($S \cdot s^{0.5}$)	Goodness of Fit
Symmetric	8.294	1.93×10^{-3}	0.557	1.675	3.89×10^{-3}	0.998	2.750×10^{3}	1.28×10^{-2}	6.77×10^{-5}
Symmetric after cycling	6.022	8.23×10^{-4}	0.424	6.261	3.09×10^{-3}	1.000	1.691×10^{1}	2.40×10^{-3}	1.58×10^{-4}
Asymmetric	2.619	7.52×10^{-4}	0.689	13.97	2.68×10^{-3}	0.995	5.040×10^{4}	8.59×10^{-3}	3.27×10^{-4}
Asymmetric after cycling	10.25	7.77×10^{-5}	0.702	287	1.16×10^{-3}	0.758	7.323×10^{2}	9.15×10^{-4}	2.07×10^{-4}

vanadium oxide redox flow batteries, which is consistent with typical performance for electrochemical capacitors [10,11,80]. Further optimization of the composite material would be expected to improve the capacitance and energy density performance.

5.4 Conclusion

Reduced graphene oxide and vanadium oxide composites have been successfully synthesized by simultaneous electrophoretic deposition followed by a thermal reduction procedure. They have

been studied alongside samples containing the as-deposited and reduced single components to compare the composition as well as capacitive and cycling behavior. Both chemical and thermal methods for reduction were implemented. Visual observations and SEM images indicated significant reduction of the graphene oxide, which resulted in a much larger specific capacitance compared to the unreduced GO film. When comparing the reduced films with the GO film, the chemical treatment induced a larger quantity of defects in the GO sheets, whereas the thermal reduction method introduced a larger range of defects, especially in the stacking order, according to Raman spectroscopy. Additionally, EIS analysis indicated that the thermal method increased the series resistance but decreased the charge transfer resistance, which could be explained by a loss of water content that would be expected to decrease the ionic conductivity while simultaneously increasing the electrical conductivity. EIS further indicated that the as-deposited and reduced graphene oxide materials exhibit a significant amount of pseudocapacitance. The high defect quantity observed with Raman is likely involved in the pseudocapacitance [76]. Furthermore, Raman and EIS analysis support the conclusion that the quantity of defects in the graphene oxide decreases with cycling.

A composite material was synthesized with graphene oxide co-deposited with a vanadium oxide nanowire network; Raman and SEM confirmed its composition and morphology, respectively. Although the chemical technique was determined non-ideal for treatment of the composite material due to the high solubility of vanadium oxide in strongly alkaline solutions, the thermally reduced form of the composite material retained the nanowire structure, consistent with the Raman symmetry of primarily V(V) oxidation state of vanadium oxide, beneath the reduced graphene oxide component. Four-point probe analysis determined that the sample resistance of the thermally treated graphene oxide and vanadium oxide composite was lower than that of the thermally treated vanadium oxide by a factor of 3.5, which indicated that the overall electrical conductivity was dominated by the carbonaceous material. The thermally reduced composite performed with a specific capacitance 4.0 and 7.5 times higher than vanadium oxide alone at 10 mV s^{-1} and 500 mV s^{-1}, respectively. The increased electrical conductivity, as well as the significant double-layer capacitance of the thermally reduced graphene oxide, likely contributed to the improved performance at higher charge/discharge rates.

The specific capacitance of the electrophoretically deposited vanadium oxide alone is one to two orders of magnitude lower than typical values reported in the literature, especially compared to those films synthesized by electrochemical deposition [21,41]. This is likely due to the differences in the electrical conductivity throughout the thickness of the films. Due to the nature of the synthesis procedure, electrochemically deposited films must maintain a higher electrical conductivity from the substrate to the surface in order to continue deposition of thicker films. This process results in the deposition of a mixed oxide between V(IV) and V(V) [41], and as the concentration of V(IV) increases, the electronic conductivity increases [18,61]. The Raman analysis indicates the oxidation state of the electrophoretically deposited vanadium oxide is primarily V(V), which would consequently cause a lower electrical conductivity. Consequently, the thermally reduced graphene oxide was incorporated with the vanadium oxide to improve the electrical conductivity, thus allowing for increased electronic transport throughout the film. Although four point probe measurements confirmed the decreased resistance, the composite still performed with a capacitance an order of magnitude lower than other composites of vanadium oxide containing carbon [22]. Although the thermal treatment improved the electrical

conductivity of the thermally reduced graphene oxide, it significantly reduced the ionic transport to the vanadium oxide, resulting in reduced accessibility of the electrolyte for pseudocapacitance. This result is consistent with other studies that found a reduction in capacitance following thermal treatment of vanadium oxide [20,41]. Further optimization of the thermal treatment temperature and duration as well as the relative concentration ratio of the composite components is expected to lead to incremental improvements in the capacitive performance.

The thermally reduced composite material was incorporated in both symmetric and asymmetric whole cell devices. Due to the compositional difference between the asymmetric cell electrodes, it was capable of a potential window approximately twice that of the symmetric cell. Additionally, the asymmetric cell was able to perform with approximately four times larger specific capacitance at 50 mV s^{-1} and eight times larger capacitance at 500 mV s^{-1}. The higher potential window and capacitance of the asymmetric cell resulted in a 20 times larger energy density than the symmetric cell. Furthermore, the lower equivalent series resistance of the asymmetric cell determined by EIS analysis resulted in a 40 times larger power density than the symmetric cell. The asymmetric cell appears to perform better for higher-rate, higher-power density applications due to the significant double-layer capacitance contribution from the thermally reduced graphene oxide. However, the cycle life of the asymmetric cell was drastically inferior to the symmetric cell. The symmetric cell retained 34% capacitance after 50,000 cycles, whereas the asymmetric cell lost all capacitance before 40,000 cycles. EIS analysis suggested that a decrease in double-layer capacitance and an increase in charge transfer resistance accompanied the capacitive degradation. Although more research is needed to improve the stability of the electrodes in asymmetric cells, the thermally reduced graphene oxide and vanadium oxide electrodes have demonstrated the potential for use in high energy and power density applications due to their capability of high cycle-rate pseudocapacitance.

Chapter 6 – Conclusion

6.1 Summary

An investigation into the morphology, composition and electrochemical properties of electrodeposited vanadium oxide and electrophoretically deposited graphene oxide and vanadium oxide composites was performed to illuminate the viability of these materials for electrochemical capacitor electrodes. This research has identified the primary capacitive degradation mechanism of electrodeposited vanadium oxide in aqueous environments to be anodic or cathodic material dissolution depending upon the pH environment of the electrolyte in contact with the electrode. The electrode that exhibited the least amount of degradation was cycled in a pH 3.0 environment, which represented the thermodynamic aqueous stability region of least solubility over the entire potential region per cycle. However, this half-cell test, although critical to understanding the aqueous cycle behavior of vanadium oxide, cannot attest to the behavior of an electrode in a two-electrode whole cell electrochemical capacitor device. In further studies the electrodes were encased in button-type whole cell designs, where the electrolyte volume was limited to the pore volume and area immediately adjacent to the electrode surface, and the aqueous system cycle behavior was drastically improved.

Preferred electrolyte-solvent systems were identified using capacitance and impedance data collected for both aqueous and nonaqueous systems, and both were utilized in the cycle-behavioral studies in whole cell designs. The 3.0 M NaCl aqueous system at pH 3.0 exhibited excellent cyclability and high power density at both relatively fast, 500 mV s^{-1}, and slow, 10 mV s^{-1}, rates; however, the 1.0 M nonaqueous LiBr in PC exhibited a larger energy density at slower scan rates due to the larger operational voltage window not possible in aqueous systems. The nonaqueous LiBr-PC system at slower scan rates represents a complimentary cycle rate region where vanadium oxide may be successfully utilized in not only high power density but also higher energy storage density technology.

Although vanadium oxide alone shows promise in both aqueous and nonaqueous electrochemical capacitor systems, it is still limited by its relatively lower electrical conductivity. This property limits its ability to form thick films using electrochemical deposition synthesis methods, and it limits the power density at faster cycle rates due to the slow electron transport through the bulk material for the solid-state pseudocapacitive mechanism. Therefore, the addition of carbonaceous materials that exhibit higher electrical conductivity could improve the accessibility of the vanadium oxide in bulk electrodes. Carbonaceous materials also exhibit significant double-layer capacitance and usually a small degree of pseudocapacitance, which both contribute to the overall electrode capacitance. Graphene oxide was simultaneously deposited with vanadium oxide nanowires using electrophoretic deposition followed by a chemical or thermal treatment. The thermal reduction method significantly decreased the electrode resistance and improved the electrode capacitance. A symmetric whole cell was constructed utilizing the thermally reduced composites for both electrodes, and an asymmetric whole cell was assembled with the thermally reduced composite as the positive electrode and the thermally reduced graphene oxide alone on a stainless steel mesh as the negative electrode. Although the

asymmetric cell performed with a higher capacitance and thus a higher energy density, the symmetric cell exhibited a significantly higher capacitive retention with cycling. Nevertheless, the composite material containing both the vanadium oxide pseudocapacitive component and the reduced graphene oxide component providing the electrically conductive pathways resulted in electrodes with substantial potential for higher cycle-rate applications requiring both high energy density and high power density applications.

6.2 Future Work

Overall, vanadium oxide appears to be a promising material for electrochemical capacitor electrodes, but its properties are extremely sensitive to the synthesis methods used and environment in which it is cycled. The electrochemical deposition method used in this work produced a highly connected but porous network of vanadium oxide nodular structures, which allowed for electrical transport through the solid-state pathways leading to pores providing ionic transport for the electrolyte. However, depositing thick uniform films or the simultaneous deposition with carbonaceous materials for bulk electrodes is a challenge with this method. The electrophoretic deposition method utilized for the graphene oxide and vanadium oxide composites was used to synthesize much thicker films in a fraction of the time, but the as-deposited network of loosely packed vanadium oxide nanowires and graphene oxide sheets may result in large contact resistances between the particles. The thermal reduction treatment utilized on the composites increased the overall conductivity, but further optimization is necessary to balance the increased electrical conductivity while minimizing water loss causing capacitive losses due to a decreased ionic conductivity. In addition, studies altering the ratio of vanadium oxide and graphene oxide are expected to improve the specific capacitance by minimizing the vanadium oxide component based on the desired rate-capability, power density and energy density for the desired application. The graphene oxide component favors a larger power density, while the vanadium oxide component, requiring slower cycle-rate charging, favors a larger overall energy density.

References

[1] B.E. Conway, Electrochemical Supercapacitors: Scientific Fundamentals and Technological Applications, Kluwer Academic/Plenum Publishers, New York, 1999.

[2] D.A. Scherson, A. Palenscár, Electrochem Soc Interface (2006) 17.

[3] H.I. Becker, Low Voltage Electrolytic Capacitor, 2800616, 1957.

[4] J.R. Miller, in:, Short Course 1, PRIME ECS Meeting, Honolulu, HI, 2012, pp. 1–316.

[5] S. Trasatti, G. Buzzanca, J Electroanal Chem 29 (1971) 1.

[6] H.Y. Lee, J.B. Goodenough, J Sol State Chem 148 (1999) 81.

[7] J.B. Goodenough, Basic Research Needs for Electrical Energy Storage: Report of the Basic Energy Sciences Workshop on Electrical Energy Storage, Office of Basic Energy Sciences, Department of Energy, 2007.

[8] Energy Storage Activities in the United States Electricity Grid, Electricity Advisory Committee, U. S. Department of Energy, 2011.

[9] Global Energy Storage Capacity to Multiply 100-Fold by 2021, Navigant Research, 2011.

[10] R. Kotz, M. Carlen, Electrochim Acta 45 (2000) 2483.

[11] J.H. Chae, K.C. Ng, G.Z. Chen, P I Mech Eng a-J Pow 224 (2010) 479.

[12] W. Deng, X. Ji, Q. Chen, C.E. Banks, Rsc Adv 1 (2011) 1171.

[13] X. Zhao, B.M. Sánchez, P.J. Dobson, P.S. Grant, Nanoscale 3 (2011) 839.

[14] V.S. Bagotsky, Fundamentals of Electrochemistry, John Wiley & Sons, Inc, New Jersey, 2006.

[15] J.W. Long, K.E. Swider, C.I. Merzbacher, D.R. Rolison, Langmuir 15 (1999) 780.

[16] P. Jampani, A. Manivannan, P.N. Kumta, Electrochem Soc Interface (2010) 57.

[17] B. Saravanakumar, K.K. Purushothaman, G. Muralidharan, ACS Appl. Mater. Interfaces 4 (2012) 4484.

[18] L.-M. Chen, Q.-Y. Lai, H.M. Zeng, Y.-J. Hao, Huang Jian-Hua, J Appl Electrochem 41 (2011) 299.

[19] R.N. Reddy, R.G. Reddy, J Power Sources 156 (2006) 700.

[20] C.-M. Huang, C.-C. Hu, K.-H. Chang, J.-M. Li, Y.-F. Li, J Electrochem Soc 156 (2009) A667.

[21] H. Jeon, B. Jeong, J.K. Lee, H.S. Kim, S.-H. Lee, J. Lee, Electrochem Solid St 13 (2010) A25.

[22] B. Wang, K. Konstantinov, D. Wexler, H. Liu, G. Wang, Electrochim Acta 54 (2009) 1420.

[23] C.-H. Lai, C.-K. Lin, S.-W. Lee, H.-Y. Li, J.-K. Chang, M.-J. Deng, J Alloy Compd 536 (2012) S428.

[24] S.-L. Chou, J.-Z. Wang, H.-K. Liu, S.-X. Dou, Adv Sci Lett 3 (2010) 295.

[25] G. Wang, X. Lu, Y. Ling, T. Zhai, H. Wang, Y. Tong, Y. Li, ACS Nano 6 (2012) 10296.

[26] Y. Sato, T. Nomura, A. Tanaka, K. Kobayakawa, J Electrochem Soc 138 (1991) L37.

[27] E. Shembel, R. Apostolova, V. Nagirny, D. Aurbach, B. Markovsky, J Power Sources 81 (1999) 480.

[28] E. Potiron, A. La Salle, A. Verbaere, Y. Piffard, D. Guyomard, Electrochim Acta 45 (1999) 197.

[29] P. Liu, J.-G. Zhang, C.E. Tracy, J.A. Turner, Electrochem Solid St 3 (2000) 163.

[30] M. Nakayama, A. Tanaka, S. Konishi, K. Ogura, J Mater Res 19 (2004) 1509.

[31] K. Takahashi, S. Limmer, Y. Wang, G. Cao, J Phys Chem B 108 (2004) 9795.

[32] V.M. Nagirnyi, R.D. Apostolova, E.M. Shembel, Russ J Appl Chem+ 79 (2006) 1443.

[33] I. Kim, J. Kim, B. Cho, K. Kim, J Electrochem Soc 153 (2006) A1451.

[34] D.L. da Silva, R.G. Delatorre, G. Pattanaik, G. Zangari, W. Figueiredo, R.-P. Blum, H. Niehus, A.A. Pasa, J Electrochem Soc 155 (2008) E14.

[35] P. Pande, P.G. Rasmussen, L.T. Thompson, in:, ECS Fall Meeting, Las Vegas, 2010.

[36] M. Pourbaix, Atlas of Electrochemical Equilibria in Aqueous Solutions, 2nd ed., National Association of Corrosion Engineers, Houston, 1974.

[37] E. Muthuswamy, S.S. Ramadevi, H.N. Vasan, C. Garcia, L. Noe, M. Verelst, J Nanopart Res 9 (2007) 561.

[38] M. Lahaye, J Appl Phycol 13 (2001) 173.

[39] C.M.A. Brett, A.M.O. Brett, Electrochemistry: Principles, Methods, and Applications, Oxford UP, Oxford, 1993.

[40] J.-H. Chang, J. Park, Y.K. Pak, J.J. Pak, IEEE EMBS Conference on Neural Engineering (2007) SaD1.9.

[41] A.M. Engstrom, F.M. Doyle, J Power Sources 228 (2013) 120.

[42] G. Wee, H.Z. Soh, Y.L. Cheah, S.G. Mhaisalkar, M. Srinivasan, J Mater Chem 20 (2010) 6720.

[43] E. Khoo, J. Wang, J. Ma, P.S. Lee, J Mater Chem 20 (2010) 8368.

[44] D. Wei, M.R.J. Scherer, C. Bower, P. Andrew, T. Ryhänen, U. Steiner, Nano Lett. 12 (2012) 1857.

[45] M. Ue, K. Ida, S. Mori, J Electrochem Soc 141 (1994) 2989.

[46] P.K. Muhuri, S.K. Ghosh, D.K. Hazra, J Chem Eng Data 38 (1993) 242.

[47] B. Long, Ind Eng Chem Res 50 (2011) 7019.

[48] Bulletin 102B: Dimethyl Sulfoxide (DMSO) Solubility Data, Gaylord Chemical Company, LLC, 2007.

[49] W.L. Reynolds, Prog Inorg Chem 12 (1970).

[50] Huang J.-H, Lai Q.-Y, Song J.-M., Chen L.-M, X.Y. Ji, Chinese J Inorg Chem 23 (2007) 237.

[51] Z. Chen, Y. Qin, D. Weng, Q. Xiao, Y. Peng, X. Wang, H. Li, F. Wei, Y. Lu, Adv Funct Mater 19 (2009) 3420.

[52] L.-M. Chen, Q.-Y. Lai, Y.-J. Hao, Y. Zhao, X.-Y. Ji, J Alloy Compd 467 (2009) 465.

[53] Y.U. Jeong, A. Manthiram, J Electrochem Soc 149 (2002) A1419.

[54] J.C. Fanning, Coord Chem Rev 140 (1995) 27.

[55] S.H. Lee, J.C. Rasaiah, J Chem Phys 101 (1994) 6964.

[56] S. Koneshan, J.C. Rasaiah, R.M. Lynden-Bell, S.H. Lee, J Phys Chem B 102 (1998) 4193.

[57] J. Mähler, I. Persson, Inorg Chem 51 (2012) 425.

[58] S.I. Dutch, J Chem Educ 76 (1999) 1.

[59] J. Światowska-Mrowiecka, V. Maurice, S. Zanna, L. Klein, E. Briand, I. Vickridge, P. Marcus, J Power Sources 170 (2007) 160.

[60] D.W. Murphy, P.A. Christian, F.J. DiSalvo, J.V. Waszczak, Prog Inorg Chem 18 (1979) 2800.

[61] J. Muster, G.T. Kim, V. Krstic, J.H. Park, Y.W. Park, S. Roth, Adv Mater 12 (2000) 420.

[62] M.S. Whittingham, J Electrochem Soc 123 (1976) 315.

[63] Y. Wang, Z. Shi, Y. Huang, Y. Ma, C. Wang, M. Chen, Y. Chen, J Phys Chem C 113 (2009) 13103.

[64] J.R. Lake, A. Cheng, S. Selverston, Z. Tanaka, J. Koehne, M. Meyyappan, B. Chen, J. Vac. Sci. Technol. B 30 (2012) 03D118.

[65] M.F. El-Kady, V. Strong, S. Dubin, R.B. Kaner, Science 335 (2012) 1326.

[66] D.R. Dreyer, S. Park, C.W. Bielawski, R.S. Ruoff, Chem Soc Rev 39 (2009) 228.

[67] S. Pei, H.-M. Cheng, Carbon 50 (2012) 3210.

[68] J.W. Long, D. Belanger, T. Brousse, W. Sugimoto, M.B. Sassin, O. Crosnier, Mrs Bull 36 (2011) 513.

[69] W.G. Menezes, D.M. Reis, T.M. Benedetti, M.M. Oliveira, J.F. Soares, R.M. Torresi, A.J.G. Zarbin, J Colloid Interf Sci 337 (2009) 586.

[70] D.C. Marcano, D.V. Kosynkin, J.M. Berlin, A. Sinitskii, Z. Sun, A. Slesarev, L.B. Alemany, W. Lu, J.M. Tour, ACS Nano 4 (2010) 4806.

[71] D. Pan, Z. Shuyuan, Y. Chen, J.G. Hou, J Mater Res 17 (2002) 1.

[72] V. Lee, L. Whittaker, C. Jaye, K.M. Baroudi, D.A. Fischer, S. Banerjee, Chem Mater 21 (2009) 3905.

[73] M.A. Pimenta, G. Dresselhaus, M.S. Dresselhaus, L.G. Can ado, A. Jorio, R. Saito, Phys Chem Chem Phys 9 (2007) 1276.

[74] M.S. Dresselhaus, G. Dresselhaus, M. Hofmann, Philos Trans R Soc London Ser A 366 (2008) 231.

[75] A. Ferrari, J. Robertson, Phys Rev B 64 (2001) 075414.

[76] B. Xu, S. Yue, Z. Sui, X. Zhang, S. Hou, G. Cao, Y. Yang, Energ Environ Sci 4 (2011) 2826.

[77] X. Wang, H. Li, Y. Fei, X. Wang, Y. Xiong, Y. Nie, K. Feng, Appl Surf Sci 177 (2001) 8.

[78] D.A. McKeown, P.L. Hagans, L.P.L. Carette, A.E. Russell, K.E. Swider, D.R. Rolison, J Phys Chem B 103 (1999) 4825.

[79] J.S. Lawton, A. Jones, T. Zawodzinski, J Electrochem Soc 160 (2013) A697.

[80] T. Nguyen, R.F. Savinell, Electrochem Soc Interface (2010) 54.